

**2005 ANNUAL REPORT  
FUSION RESEARCH CENTER  
GEORGIA INSTITUTE OF TECHNOLOGY  
ATLANTA, GA 30332**

**W. M. STACEY  
OCTOBER, 2005**

The Georgia Tech Fusion Research Center (FRC) provides a focus on-campus for research in fusion plasma physics and technology, maintains a research library of international fusion reports, and supports the educational mission of Georgia Tech in the areas of plasmas and fusion technology. This report summarizes the research carried out in the FRC during 2005 and serves as an annual report for Dept. of Energy Grants ER54538 and ER54350.

**Collaborators:**

*Georgia Tech Faculty* R. W. Johnson (FRC), W. J. Lackey (ME), J. Mandrekas (FRC—on leave to DOE/OFES), C. de Oliveira (NRE), W. M. Stacey (NRE), D. W. Tedder (ChBE)

*Georgia Tech NRE Students* Z. Abbasi, C. Boyd, A. Bridges, E. Burgett, M. Cymbor, S. Fowler, Z. W. Friis, A. Jones, R. Kelm, R. Kern, D. Lassiter, J. W. Maddox, W. Murphy, H. Park, J. Pounders, J. Preston, D-K. Zhang

*Argonne National Laboratory, Nuclear Engineering Div.* E. A. Hoffman

*General Atomics, Fusion Division* R. J. Groebner, A. W. Leonard, T. W. Petrie

**Research Reports**

- p2     Improvements in the 2D TEP Neutral Particle Transport Calculation in Edge Plasmas (DoE Grant ER54538)
- p7     Rotation velocities and radial electric field in the plasma edge
- p14    Investigation of the cause of the High-to-Low mode confinement transition following MARFE formation in DIII-D (DoE Grant ER54538)
- p22    Calculation of toroidal rotation profiles in DIII-D using neoclassical viscosity (DoE Grant ER54538)
- p43    Investigation of edge pedestal structure in DIII-D (DoE Grant ER54538)
- p68    A sub-critical, He-cooled, fast reactor for the transmutation of spent nuclear fuel (DOE Grant ER54350)

# I. Improvements in the 2D TEP Neutral Particle Transport Calculation in Edge Plasmas (DoE Grant ER54538)

D. Zhang, J. Mandrekas, and W. M. Stacey  
(to be published in *Contributions to Plasma Physics*, 2006)

## Abstract

Extensions of the 2D Transmission and Escape Probability neutral particle transport method in treating the spatial non-uniformity of collision sources and neutral energy effects are presented. These extensions have been tested by benchmarks against Monte Carlo calculations for specially designed models and for realistic DIII-D discharges. The comparisons indicate these extensions improve accuracy of the TEP method.

## 1. Introduction

The Transmission and Escape Probability (TEP) method [1] and the 2D code GTNEUT [2] based thereon have been used to analyze 2D neutral particle transport for realistic edge models of plasma experiments. While comparisons of GTNEUT with Monte Carlo calculations of neutral measurements in DIII-D showed good agreement [3,4], extensive model problem testing identified certain limiting conditions for which some of the original TEP approximations could lead to inaccuracy [3,5]. We have previously described [6] an extension of the original DP0 approximation of the angular distribution of the incident neutral flux across interfaces to DP1 and DP2 to improve the accuracy of the calculation of transmission probabilities for models in which transmission across a series of optically thin regions would produce increasingly forward peaked anisotropic fluxes incident across successive interfaces. In this paper we report improved approximations which allow a more accurate treatment of 1) the preferential escape of scattered or charge-exchanged neutrals back across the incident surface in optically thick regions 2) the energy distribution of neutrals in optically thin regions in locations with strong background plasma ion temperature gradients.

## 2. Two Major Improvements

### 2.1 Correction to escape probabilities

The TEP method is based on the particle current balance [1] across each interface between any two contiguous computational regions. An exiting current from a region is coupled to all incoming currents from all the adjacent regions via transmission and escape probabilities.

$$\Gamma_{i,j}^n = \sum_{k,n'} T_{i,k \rightarrow j}^{n' \rightarrow n} \Gamma_{k,i}^{n'} + \sum_{k,n'} \left( \delta_{n'0} - \sum_l T_{i,k \rightarrow l}^{n' \rightarrow 0} \right) \Gamma_{k,i}^{n'} c_i P_i \Lambda_{ij}^0 \delta_{n0} + S_{ext}^i P_i \Lambda_{ij}^0 \delta_{n0} \quad (1)$$

where  $\Gamma_{i,j}^n$  is the  $n$ -th moment of the total partial current from region  $i$  to region  $j$ ,  $T_{i,k \rightarrow j}^{n' \rightarrow n}$  represent the transmission probability that neutral particles flowing from region  $k$  in moment  $n'$  to region  $i$  will be directly transmitted to region  $j$  in moment  $n$  without a collision within region  $i$ ,  $P_i$  is the total escape probability that charge-exchanged and recombination neutrals or their progenies within region  $i$  escape into region  $j$ ,  $\Lambda_{i,j}^0$  is the directional escape probabilities that neutrals escaping from region  $i$  escape into region  $j$ ,  $c_i$  is the charge exchange fraction and  $S_{ext}^i$  represents recombination neutral source rate.

The accuracy of the TEP method depends completely on transmission and escape probabilities. The DP<sub>1</sub> or DP<sub>2</sub> approximation of the angular distribution allows a more accurate evaluation of transmission probabilities for optically thin regions, but the calculation of collision probabilities was previously based on the flat collision source approximation. In this approximation, the collision source is assumed to be uniformly distributed over each computational region, implying that the collision source has no preferable escaping direction. Since the actual collision source is strongly peaked near the incident surface for an optically thick region, and consequently charge-exchanged neutrals are more likely to escape back across the incident surface than in any other directions. As a result, the flat collision source approximation leads to an over-predication of collided fluxes in the forward direction in optically thick regions.

The variational diffusion approximation used in this research to correct directional escape probabilities consists of three steps. First, the original problem with non-uniform first-collision sources resulting from

neutrals entering from all adjacent regions is separated into several simpler problems, within each of which we only deal with the first-collision source associated with neutrals entering from one of the contiguous regions. The linear separation in this step converts the original problem into collision response calculations, and therefore directionalities could be calculated if even the exact collision source distribution of the original problem is unknown. In the second step, the diffusion approximation (2) is used to describe neutral transport in an optically thick region.

$$-\nabla \cdot D \nabla \phi(r) + \Sigma_a \phi(r) = S_{j,i}^0(\mathbf{r}) \quad (2)$$

where  $\phi(\mathbf{r})$  is the neutral scalar flux,  $D$  is the diffusion coefficient,  $\Sigma_{ion}$  is the total macroscopic ionizing cross section,  $S_{j,i}^0(\mathbf{r})$  represents the first-collision source distribution associated with a flux entering from region  $j$  to region  $i$ . In the last step, each optically thick region is divided into a number of sub-regions (elements), finite element methods are applied to the diffusion equation (2) to obtain a piecewise linear flux representation, and finally the total and directional escape probabilities can be calculated.

In addition to the non-uniformity of the first collision rate within optically regions, angular fluxes along interfaces between regions are also characterized by a strong gradient, which couples the spatial non-uniformity of both uncollided and collided fluxes with contiguous regions. To take this effect into account, a spatially linear function is added to the set of original DP<sub>1</sub> representation functions [6].

$$\psi_{i,j}^3(x_{ij}, \mathbf{\Omega}) = \frac{2\sqrt{3}}{\pi L_{ij}^2} (x_{ij} - 0.5L_{ij}) \quad (3)$$

where  $L_{ij}$  is the length of the interface between regions  $i$  and  $j$ ,  $\psi_{i,j}^3(x_{ij}, \mathbf{\Omega})$  represents a spatially linear and angularly isotropic representation function. Here spatially linear DP<sub>1</sub> (and also linearly anisotropic) representation functions are not taken into consideration because they can always be regarded as higher order approximations either for optically thick or thin regions. Apparently, for optically thin regions, all the spatially linear terms can be neglected, while for optically thick region, it has been shown that all DP1 terms can be safely ignored because of the randomization of charge-exchanged scattering events.

The non-uniformity of uncollided fluxes is embodied in calculations of transmission probabilities, while the non-uniformity of collided fluxes is taken into account in diffusion calculations of escape probabilities. To the lowest order the following two linear contributions for the collided flux crossing an interface of a given region must be considered: (1) the spatially linear outgoing collided flux associated with a spatially uniform flux entering into that region, where the non-uniformity is driven by material attenuation; (2) the spatially linear collided angular flux associated with a spatially linear flux entering into that region, where the non-uniformity is driven by the non-uniform incoming flux and material attenuation.

## 2.2 Neutral energy treatment

The treatment of the neutral energy distribution has an important impact on accuracy of the TEP method. Transmission and escape probabilities are functions of the neutral mean free path (mfp), which depends on neutral energies. As a result, errors in the neutral energy treatment can propagate to the neutral partial current crossing each interface. The original TEP method used the local ion temperature (LIT) approximation, which basically assumed all neutrals from a region are in thermal equilibrium with ions in that region, resulting an average energy equal to the local ion temperature, i.e.  $\bar{E} = T_i$ , where  $T_i$  is the local ion temperature in region  $i$ . Extensive comparisons with Monte Carlo show that this is a good approximation when the mfp is small compared to the characteristic dimension of computational regions, or the local ion temperature changes slowly from region to region. However, for a long mfp region, neutrals from this region predominantly consist of uncollided neutrals directly transmitted from the adjacent regions, and if, at the same time, the local ion temperature changes dramatically across from region to region, the energy of collided neutrons are significantly different from the local ion temperature, and therefore the original approximation that the local neutral distribution could be represented as a Maxwellian with the local ion temperature becomes inadequate.

To remedy this defect, the average neutral energy (ANE) approximation used in this research calculates the average energy of neutrals flowing out across an interface as a weighted average of energies

of uncollided neutrals directly transmitted from all the contiguous regions and energies of charge-exchanged neutrals in the thermal equilibrium with the local ions within that region, i.e.

$$\bar{E}_{ij} = \frac{\sum_{k,n} T_{i,k \rightarrow j}^{n \rightarrow 0} \Gamma_{k,i}^n \bar{E}_{ki} + \Gamma_{i,j}^{c,0} T_i}{\sum_{k,n} T_{i,k \rightarrow j}^{n \rightarrow 0} \Gamma_{k,i}^n + \Gamma_{i,j}^{c,0}} \quad (4)$$

where  $\bar{E}_{ij}$  is the average energy of neutrals from region  $i$  to region  $j$ ,  $\sum_n T_{i,k \rightarrow j}^{n \rightarrow 0} \Gamma_{k,i}^n$  represents the uncollided current from region  $k$  to region  $j$ ,  $\Gamma_{i,j}^{c,0}$  is the collided current from region  $i$  to region  $j$ .

Before using Equation (4) to evaluate the average neutral energy, uncollided and collided currents across each interface must be known; to calculate these currents, we have first to compute transmission and escape probabilities, which implicitly depends on the neutral energy distribution. The neutral current balance equation must be solved iteratively. The iterative process is started with the local ion temperature approximation ( $\bar{E}_{ij} = T_i$ ), and then the mfp, transmission and escape probabilities can be evaluated. After that, we can solve the linear equations (1) to obtain collided and uncollided fluxes, which can then be used to update the average neutral energy in Equation (4). Once the average neutral energies are well converged, neutral densities and reaction rates can be computed.

### 3. Results and discussion

In order to investigate the impact of the variation diffusion approximation on the accuracy of the TEP method, a test problem with a uniform background plasma is chosen to avoid errors introduced by neutral energy approximations. Similarly, vacuum boundaries are assumed on the four external interfaces, so that errors produced by the reflection models can be precluded. The problem shown in Fig. 1 consists of nine identical squares. A uniform neutral source with unit strength is imposed on the left boundary of region 2.

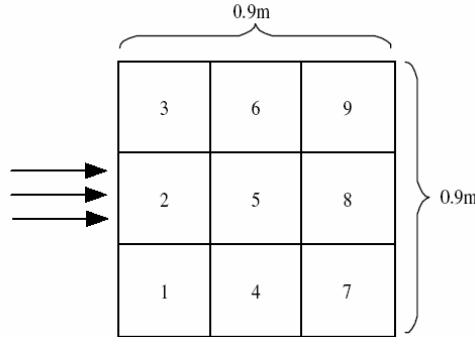


Fig.1 Geometry for the 2D nine-region configuration

Both the electron and ion temperatures are 10 eV. The charge exchange fraction and  $\Delta/\lambda$  ratio are adjusted to be 0.9 and 5, respectively, resulting in a very strongly non-uniform collision source distribution of incident neutrals in region 2. Neutral densities calculated by DEGAS and GTNEUT with various approximations are shown in Fig. 2. It can be seen that GTNEUT with the  $DP_0$  approximation significantly over-estimates neutral densities for regions away from the source, and there is no obvious improvement using the  $DP_1$  approximation, since both calculations ignore the strong gradient of collision sources and angular fluxes in region 2. With the non-uniformity of collision sources taken into account, the diffusion approximation significantly improves agreement with the Monte Carlo calculations, but it still over-predicts the results for regions 4-9, since the effects of non-uniform flux along interfaces between regions are neglected. If both the diffusion and spatially linear angular flux approximation are used, the GTNEUT calculations are in excellent agreement with the DEGAS simulations.

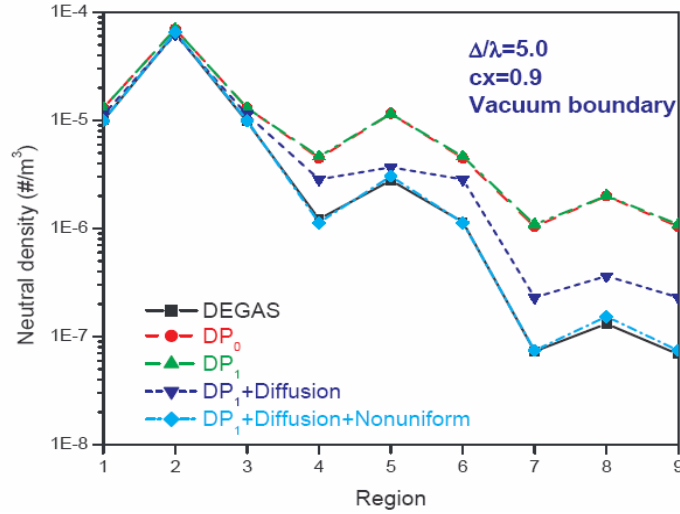


Fig.2 Neutral densities calculated by DEGAS and GTNEUT for the 2D model problem

In addition to specially designed model problems, realistic DIII-D discharges are also used to test the performance of the new extensions. The geometric configuration of the DIII-D discharge 96747 at 3940 ms is shown in Fig. 3, where the shaded regions represent the locations where neutral densities were measured. The problem is characterized by a strong gradient in the background plasma properties. For instance, the ion temperature varies from 57 eV in the private flux region to more than 600 eV inside the separatrix near the X-point. As a result, the neutral mean free path could be lower than 6 cm in the main plasma region, while it could be as high as 26 m outside the separatrix. Recycling neutral sources are imposed on bottom boundaries of regions 2-13, and for all regions, the grid size is much smaller compared to the mfp, resulting in three important effects on neutral transport in this specific problem: 1) strong anisotropy of angular fluxes, 2) almost uniform collision sources within each computational region, and 3) a big difference between energies of collided and uncollided fluxes.

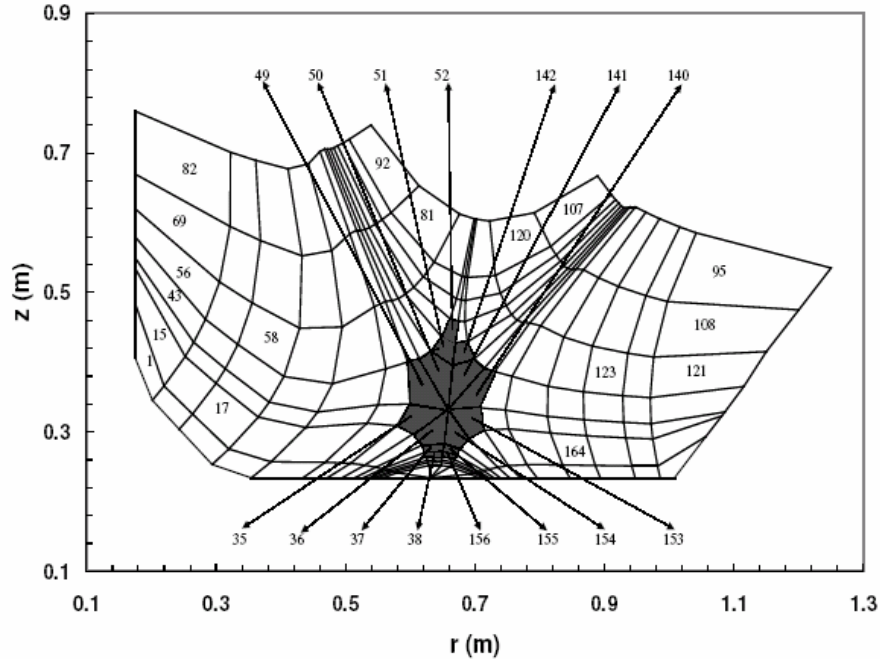


Fig.3 Geometry for the DIII-D H discharge 96747 at 3940 ms

The comparison of density calculations by DEGAS and GTNEUT with different level approximations is illustrated in Fig. 4. It can be seen that the ANE approximation is superior to the LIT approximation, since the energy of uncollided neutrals originating from carbon walls is much lower than that of collided neutrals, and consequently the LIT approximation cannot sufficiently represent the neutral energy distribution. The  $DP_1$  approximation also improves agreement with DEGAS simulations, since in

optically thin regions neutral fluxes become strongly anisotropic. The diffusion approximation has no obvious improvement as we expected for large mean free path regions.

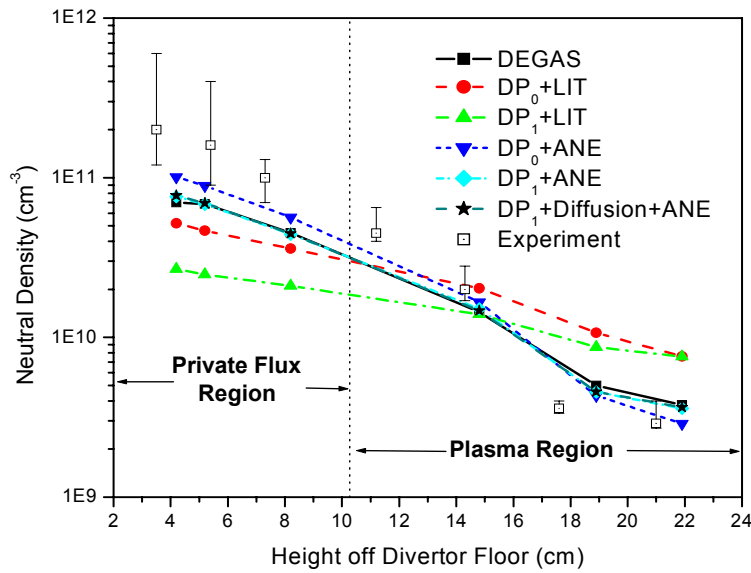


Fig.4 Neutral densities calculated by DEGAS and GTNEUT for the DIII-D H discharge

#### 4. Conclusions

The variational diffusion and ANE approximations have been developed to extend the TEP method. Benchmark comparisons with Monte Carlo for model problems in which the mean free path was small relative to the dimension of the computational region indicate that the intra-nodal diffusion treatment of the escape probability directionality significantly improves accuracy in optically thick regions. Iterative calculation of average neutral energy in a region as the weighted average of the energies of neutrals incident from the contiguous regions and the energy of neutrals resulting from charge-exchanged ions within the region, has been found to yield improved and quite good agreement with continuous energy Monte Carlo calculations for both model problems and realistic DIII-D discharges.

#### References

- [1] W.M. Stacey and J. Mandrekas, *Nuclear Fusion* 34 (1994)1385.
- [2] J. Mandrekas, *Computer Physics Communications* 36 (2004)161.
- [3] W. M. Stacey, J. Mandrekas and R. Rubilar, *Fusion Sci. Techn.*, 40 (2001) 66.
- [4] J. Mandrekas, R. J. Colchin, W. M. Stacey, et al., *Nucl. Fusion*, 43 (2003) 314.
- [5] R. Rubilar, W. M. Stacey and J. Mandrekas, *Nucl. Fusion*, 41 (2001) 1003.
- [6] D. Zhang, J. Mandrekas and W.M. Stacey, *Contributions to Plasma Physics*, 44 (2004) 45.

## II. Rotation velocities and radial electric field in the plasma edge

W. M. Stacey

(to be published in *Contributions to Plasma Physics*, 2006)

### 1. Introduction

The toroidal and poloidal rotation and related radial electric field observed in the edge (and core) of tokamak plasmas are of interest for several reasons, not least of which is what they reveal about radial momentum transport, but also because of their apparent role in the L-H transition and the edge pedestal. It was recently shown<sup>1</sup> that if the heat transport coefficients and rotation velocities are taken from experiment, then the particle, momentum and energy balance equations and the conductive heat conduction relation are sufficient to determine the observed edge pedestal profile structure in the density and temperature profiles in several DIII-D discharges. Thus, it would seem that understanding the edge pedestal structure is a matter of understanding the edge rotation profiles. We present a practical computational model for the rotation and the radial electric field profiles in the plasma edge that is based on momentum and particle balance, includes both convective (including anomalous) and neoclassical gyroviscous momentum transport, and incorporates atomic physics effects associated with recycling neutrals.

### 2. Radial Electric Field

An expression for the radial electric field can be derived from the radial component of the momentum balance equation for ion species ‘j’

$$n_j m_j \left[ (\mathbf{V}_j \cdot \nabla) \mathbf{V}_j \right]_r + [\nabla \cdot \Pi_j]_r + \frac{\partial p_j}{\partial r} = n_j e_j (E_r + V_{\theta j} B_\phi - V_{\phi j} B_\theta) + F_{rj} + M_{\xi j} - m_j (n_j v_{at,j} + \tilde{S}_j) V_{rj} \quad (1)$$

where  $M_{\xi j}$  is the  $\xi$  – component of the momentum input,  $\tilde{S}_j \equiv S_j - \langle S_j \rangle$  is the poloidally varying part of the ionization source (due to recycling and fueling neutral influx and neutral beam injection),  $F_j$  is the friction force and  $v_{at,j} = v_{ion,j} + v_{cx,j} + v_{el,j}$  represents atomic physics processes—ionization, charge exchange, elastic scattering.

The radial component of Eq. (1) yields

$$E_r = \frac{1}{n_j e_j} \frac{\partial p_j}{\partial r} + V_{\phi j} B_\theta - V_{\theta j} B_\phi - \frac{m_j}{e_j} \left( \cos \theta \frac{V_{\phi j}^2}{R} + \frac{V_{\theta j}^2}{r} \right) \quad (2)$$

where the unfamiliar last term results from retention of inertial effects to leading order.

### 3. Poloidal rotation and density asymmetries

Equations for the poloidal rotation velocities and for the poloidal density asymmetries can be derived from the poloidal components of the momentum balance equations and the particle balance equations for ion species ‘j’

$$n_j m_j \left[ (\mathbf{V}_j \cdot \nabla) \mathbf{V}_j \right]_\theta + [\nabla \cdot \Pi_j]_\theta + \frac{1}{r} \frac{\partial p_j}{\partial \theta} - M_{\theta j} - F_{\theta j} + n_j e_j (V_{rj} B_\phi - E_\theta) + m_j (n_j v_{elcx} + \tilde{S}_j) = 0 \quad (3)$$

where the poloidal components of the inertial and viscous terms are

$$n_j m_j \left[ (\mathbf{V}_j \cdot \nabla) \mathbf{V}_j \right]_\theta = n_j m_j \left[ V_{rj} \frac{\partial V_{\theta j}}{\partial r} + \frac{V_{rj} V_\theta}{r} + \frac{1}{2} \frac{1}{r} \frac{\partial V_{\theta j}^2}{\partial \theta} + \frac{V_{\phi j}^2}{R} \sin \theta \right] \quad (4)$$

and

$$\left[ \nabla \cdot \Pi_j \right]_\theta = \eta_{0j} \left( \frac{1}{2} A_{0j} \right) \left\{ \frac{1}{r} \frac{\partial \ln(\eta_{0j} A_{0j})}{\partial \theta} - 3 \frac{\sin \theta}{R} \right\} \quad (5)$$

with

$$A_0 = 2 \left\{ -\frac{1}{3} \left( \frac{\partial V_p}{\partial l_p} \right) + \left[ \left( \frac{1}{R} \right) \frac{\partial R}{\partial l_p} + \frac{1}{3} \left( \frac{1}{B_p} \right) \frac{\partial B_p}{\partial l_p} \right] V_p + f_p R \frac{\partial \left( \frac{V_\phi}{R} \right)}{\partial l_p} \right\} \quad (6)$$

and the neoclassical parallel viscosity coefficient can be represented by<sup>2</sup>

$$\eta_{0j} = \frac{n_j m_j \nu_{thj} q R \varepsilon^{-3/2} \nu_{jj}^*}{(1 + \varepsilon^{-3/2} \nu_{jj}^*)(1 + \nu_{jj}^*)} \equiv n_j m_j \nu_{thj} q R f_j (\nu_{jj}^*) \quad (7)$$

where  $\nu_{jj}^* = \nu_{jj} q R / \nu_{thj}$ ,  $f_p = B_p / B_\phi$  and  $\varepsilon = r/R$ .

Making low-order Fourier expansions of the form  $n_j(r, \theta) = n_j^0(r) + n_j^s \sin \theta + n_j^c \cos \theta$  and taking the flux surface average with weighting functions 1,  $\sin \theta$  and  $\cos \theta$  results in a coupled set of equations (three times the number of ion species) that can be solved for the  $V_{\theta j}^0$  and  $\tilde{n}_j^{s,c} \equiv n_j^{s,c} / \varepsilon n_j^0$  for all the plasma ion species. Assuming  $V_{rj} \ll V_{\theta j} < V_{\phi j}$ , the resulting equations are

$$\begin{aligned} & \hat{V}_{\theta j} \left[ -q \hat{V}_{\phi j} \varepsilon \left( \tilde{n}_j^s + \tilde{\Phi}^s \right) - q^2 f_j f_p \left( 1 + \tilde{\Phi}^c + \frac{2}{3} \tilde{n}_j^c \right) + f_p \sum_{k \neq j} \nu_{jk}^* + \right. \\ & \frac{q}{\varepsilon} \nu_{elcx,j}^* f_p + \frac{1}{2} f_p \varepsilon \nu_{ionj}^* \left\{ \left( 1 + \tilde{n}_j^c \right) \left( \frac{n_e^0}{n_j^0} \left( \tilde{n}_e^c + \tilde{n}_{oj}^c \right) - \left( \tilde{n}_j^c + \tilde{n}_{oj}^c \right) \right) + \right. \\ & \left. \left. \tilde{n}_j^s \left( \frac{\tilde{n}_e}{n_j} \left( \tilde{n}_e^s + \tilde{n}_{oj}^s \right) - \left( \tilde{n}_j^s + \tilde{n}_{oj}^s \right) \right) \right\} \right] - \sum_{k \neq j} \hat{V}_{k\theta} \left[ f_p \nu_{jk} \sqrt{\frac{m_j}{m_k}} \right] = \\ & -\hat{V}_{rj} - q \varepsilon \frac{1}{4} \tilde{n}_j^s - q \varepsilon \hat{\Phi}_j \left[ \frac{1}{4} \left( \tilde{\Phi}^s + \tilde{n}_j^c \tilde{\Phi}^s - \tilde{n}_j^s \tilde{\Phi}^c \right) \right] - q^2 f_j f_p \left( \hat{V}_{\phi j} + \hat{P}_j \right) \tilde{\Phi}^c \\ & - q \varepsilon \hat{V}_{\phi j} \left[ \left( \hat{V}_{\phi j} + \hat{P}_j \right) \tilde{\Phi}^s + \frac{1}{2} \hat{V}_{\phi j} \tilde{n}_j^s \right] - \frac{n_e^0}{n_j^0} \nu_{ionj}^* q \left[ \hat{V}_{\phi j} \varepsilon \left( \tilde{n}_e^c + \tilde{n}_{oj}^c \right) \right. \\ & \left. \left. - \frac{2}{3} q f_j \left( \tilde{n}_e^s + \tilde{n}_{oj}^s \right) \right] \right] \quad (8) \end{aligned}$$



$$\begin{aligned}
& \tilde{n}_j^s \left[ \frac{1}{3} \frac{q^2}{\varepsilon} f_j f_p \hat{V}_{\theta j} + \frac{1}{2} \varepsilon \hat{V}_{rj} - \frac{1}{2} \varepsilon f_p \sum_{k \neq j} v_{jk}^* \hat{V}_{\theta k} \sqrt{\frac{m_j}{m_k}} + \frac{1}{2} q v_{ion}^* f_p \hat{V}_{\theta j} \right] \\
& + \tilde{n}_j^c \left[ \frac{1}{2} q f_p^2 \hat{V}_{\theta j}^2 - \frac{1}{4} q + \frac{1}{2} q v_{elcx,j}^* v_{ionj}^* \right] = -\frac{1}{2} \varepsilon f_p \sum_{k \neq j} v_{jk}^* \hat{V}_{\theta j} \tilde{n}_k^s \\
& - \frac{1}{4} q \hat{\Phi}_j \left[ -\tilde{\Phi}^c \right] - \frac{q^2}{\varepsilon} f_j f_p \left[ \frac{1}{2} \left( \hat{V}_{\theta j} - \hat{V}_{\phi j} - \hat{P}_j' \right) \tilde{\Phi}^s - \frac{1}{2} q f_p^2 \hat{V}_{\theta j}^2 - \frac{1}{2} q \hat{V}_{\phi j}^2 \right. \\
& \left. - \frac{1}{2} q v_{elcx,j}^* \left[ f_p \hat{V}_{\theta j} \tilde{n}_{oj}^s + v_{ionj}^* \tilde{n}_{oj}^c \right] - q v_{ionj}^* f_p \left[ \frac{1}{2} \hat{V}_{\theta j} \left\{ \tilde{n}_{oj}^s \left( 1 + \frac{n_e^0}{n_j^0} \right) + \frac{n_e^0}{n_j^0} \tilde{n}_e^s \right\} \right. \right. \\
& \left. \left. + \frac{1}{3} \frac{q}{\varepsilon} f_j \frac{n_e^0}{n_j^0} \left( \tilde{n}_e^c + \tilde{n}_{oj}^c \right) \right] \right]
\end{aligned} \tag{9}$$

and

$$\begin{aligned}
& \tilde{n}_j^c \left[ \frac{1}{3} \frac{q^2}{\varepsilon} f_j f_p \hat{V}_{\theta j} + \frac{1}{2} \varepsilon \hat{V}_{rj} - \frac{1}{2} \varepsilon f_p \sum_{k \neq j} v_{jk}^* \hat{V}_{\theta k} \sqrt{\frac{m_j}{m_k}} + \frac{1}{2} q v_{ionj}^* f_p \hat{V}_{\theta j} \right] \\
& + \tilde{n}_j^s \left[ -\frac{1}{2} q f_p \hat{V}_{\theta j}^2 + \frac{1}{4} q - \frac{1}{2} q v_{elcx,j}^* v_{ionj}^* \right] = -\sum_{k \neq j} \tilde{n}_k^c \left[ \frac{1}{2} \varepsilon f_p v_{jk}^* \hat{V}_{\theta j} \right] \\
& - \frac{1}{4} q \hat{\Phi}_j \left[ \tilde{\Phi}^s \right] - \frac{q^2}{\varepsilon} f_j f_p \left[ \frac{1}{2} \left\{ \left( 1 + \tilde{\Phi}^c \right) \hat{V}_{\theta j} - \left( \hat{V}_{\phi j} - \hat{P}_j' \right) \tilde{\Phi}^c \right\} \right] \\
& - q \hat{V}_{\phi j}^2 \left[ \frac{1}{4} \varepsilon \left\{ \tilde{V}_{\phi j}^s \tilde{V}_{\phi j}^c + \tilde{n}_j^c \tilde{V}_{\phi j}^s + \tilde{n}_j^s \tilde{V}_{\phi j}^c \right\} \right] - \frac{1}{2} q v_{elcx,j}^* \left[ f_p \hat{V}_{\theta j} \tilde{n}_{oj}^c - v_{ionj}^* \tilde{n}_{oj}^s \right] \\
& - q f_p v_{ionj}^* \left[ \frac{1}{2} \hat{V}_{\theta j} \left\{ \tilde{n}_{oj}^c \left( 1 + \frac{n_e^0}{n_j^0} \right) + \frac{n_e^0}{n_j^0} \tilde{n}_e^c \right\} + \frac{1}{3} \frac{q}{\varepsilon} f_j \frac{n_e^0}{n_j^0} \left( \tilde{n}_e^s + \tilde{n}_{oj}^s \right) \right]
\end{aligned} \tag{10}$$

where the “e” and “o” subscripts refer to electrons and neutrals, respectively, and

$$\begin{aligned}
\hat{V}_{\theta j} &\equiv \frac{V_{\theta j}^0}{|f_p| v_{thj}}, \quad \hat{V}_{\phi j} \equiv \frac{V_{\phi j}^0}{v_{thj}}, \quad \hat{V}_{rj} \equiv \frac{V_{rj}^0}{\left( \frac{m_j v_{thj}}{e_j B_\theta^0} \right) |f_p| \left( \frac{v_{thj}}{qR} \right)}, \quad \hat{\Phi}_j \equiv \frac{e_j \Phi^0}{T_j}, \\
\hat{P}_j &\equiv \frac{1}{B_\theta^0 n_j^0 e_j v_{thj}} \frac{\partial p_j^0}{\partial r}, \quad \tilde{n}_{oj}^{c/s} \equiv \frac{n_{oj}^{c/s}}{\varepsilon n_{oj}^0}, \quad \tilde{\Phi}^{c/s} \equiv \frac{\Phi^{c/s}}{\varepsilon} = \frac{n_e^{c/s}}{\varepsilon (e \Phi^0 / T_e)}, \\
\tilde{V}_{\phi j}^s &\equiv V_{\phi j}^s / \varepsilon V_{\phi j}^0 = - \left( V_{\theta j}^0 / V_{\phi j}^0 \right) f_p^{-1} \left( \tilde{n}_j^s + \tilde{\Phi}^s \right) + \tilde{\Phi}^s \left( 1 + \bar{P}_j' / V_{\phi j}^0 \right) \\
\tilde{V}_{\phi j}^c &\equiv V_{\phi j}^c / \varepsilon V_{\phi j}^0 = 1 - \left( V_{\theta j}^0 / V_{\phi j}^0 \right) f_p^{-1} \left( 2 + \tilde{n}_j^c + \tilde{\Phi}^c \right) + \tilde{\Phi}^c \left( 1 + \bar{P}_j' / V_{\phi j}^0 \right) \\
v_{jk}^* &\equiv \frac{v_{jk}^0}{v_{thj} / qR}, \quad v_{ionj}^* \equiv \frac{\left( v_{ionj}^0 + v_{ionj,nb}^0 \right) r}{v_{thj}}, \quad v_{elcx,j}^* \equiv \frac{\left( v_{cx,j}^0 + v_{el,j}^0 \right) r}{v_{thj}}
\end{aligned} \tag{11}$$

The corresponding Fourier components of the poloidal velocity are given by

$$\tilde{V}_{\theta j}^s \equiv V_j^s / \varepsilon V_j^0 = (rv_{ion} / V_{\theta j}^0) (\tilde{n}_j^c + \tilde{n}_{oj}^c) - \tilde{n}_j^s,$$

$$\tilde{V}_{\theta j}^c \equiv V_j^c / \varepsilon V_j^0 = - (rv_{ion} / V_{\theta j}^0) (\tilde{n}_j^s + \tilde{n}_{oj}^s) - (1 + \tilde{n}_j^s) \quad (12)$$

#### 4. Toroidal viscous force

The toroidal viscous force (actually torque) can be written in toroidal flux surface coordinates<sup>3</sup>

$$R^2 \nabla \phi \cdot \nabla \cdot \Pi = \frac{1}{Rh_p} \frac{\partial}{\partial l_\psi} (R^2 h_p \Pi_{\psi\phi}) + B_p \frac{\partial}{\partial l_p} \left( -\frac{R \Pi_{p\phi}}{B_p} \right) \quad (13)$$

where the  $\Pi_{\xi\phi}$  are the stress tensor elements. In this Braginskii decomposition<sup>4</sup> of the rate-of-strain tensor in a flux-surface coordinate system, the neoclassical viscous stress tensors have ‘perpendicular’ components with coefficients  $\eta_2$  that are well known to be too small to account for the observed radial momentum transport rate, gyroviscous components

$$\Pi_{\psi\phi}^{gv} = -\eta_4 R \frac{\partial}{\partial l_p} \left( \frac{V_\phi}{R} \right), \Pi_{p\phi}^{gv} = -\eta_4 R \frac{\partial}{\partial l_\psi} \left( \frac{V_\phi}{R} \right) \quad (14)$$

and ‘parallel’ viscous components

$$\Pi_{\psi\phi}^{\parallel} = 0, \Pi_{p\phi}^{\parallel} = -\frac{3}{2} \eta_0 f_p A_0 \quad (15)$$

The Braginskii values<sup>4</sup> of the viscosity coefficients for a collisional plasma are

$$\eta_0 \simeq n T \tau f_{neo} \gg \eta_4 \simeq n T m / ZeB = \eta_0 f_{neo}^{-1} / \Omega \tau \gg \eta_2 \simeq \eta_4 / \Omega \tau \simeq \eta_0 f_{neo}^{-1} / (\Omega \tau)^2 \quad (16)$$

where  $\tau$  is the self-collision frequency and  $\Omega = m / ZeB$  is the gyrofrequency. Since typically  $\Omega \tau \approx 10^3 - 10^4$ ,  $\eta_0 f_{neo} \gg \eta_4 \gg \eta_2$ . Taking into account lower collisionality should not effect  $\eta_4$ , which has no  $\tau$ -dependence, and has been shown<sup>5,6</sup> to have very little effect on  $\eta_2$ . However, collisionality has a major effect on  $\eta_0$ , which we represent as indicated in Eq. (7) and as  $f_{neo}$  above. It has also been shown<sup>7-9</sup> that it may be necessary to extend the viscous torque to include heat flux terms in steep gradient regions with small rotation velocities, such as are found in the plasma edge.

#### 5. Toroidal Rotation

Equations for the toroidal rotation can be derived from the toroidal component of the angular momentum balance equation and the particle balance equation for species “j”

$$R^2 \nabla \phi \cdot n_j m_j (\mathbf{V}_j \cdot \nabla) \mathbf{V}_j + R^2 \nabla \phi \cdot \nabla \cdot \Pi_j = n_j e_j R (E_\phi^A + V_{rj} B_\theta) - R n_j m_j v_{jk} (V_{\phi j} - V_{\phi k}) + R M_{\phi j} - R m_j (n_j v_{at,j} + \tilde{S}_j) V_{\phi j} \quad (17)$$

where the toroidal component of the inertial term is

$$R^2 \nabla \phi \cdot n_j m_j (\mathbf{V}_j \cdot \nabla) \mathbf{V}_j = R n_j m_j \left( V_{rj} \frac{\partial V_{\phi j}}{\partial r} + \frac{V_{rj} V_{\phi j}}{R} \cos \theta + \frac{V_{\theta j}}{r} \frac{\partial V_{\phi j}}{\partial \theta} - \frac{V_{\phi j} V_{\theta j}}{R} \sin \theta \right) \quad (18)$$

##### A. Gradient Scale Length Formulation

If we can obtain gradient scale lengths (e.g. from experiment), then the flux surface averages of Eq. (17) for all can be written as a coupled set of algebraic equations at each radial point

$$n_j^0 m_j v_{jk}^0 \left( (1 + \beta_j) V_{\phi j}^0 - V_{\phi k}^0 \right) = n_j^0 e_j E_\phi^A + e_j B_\theta^0 \Gamma_j + M_{\phi j}^0 \equiv n_j^0 m_j v_{jk}^0 y_j, \quad (19)$$

where  $M_{\phi j}$  is the momentum input from the neutral beams,  $M_{\phi j}^{nb}$ , and possibly from other “anomalous” mechanisms,  $M_{\phi j}^{anom}$ , and the radial transfer of toroidal momentum by viscous, inertial, and atomic physics and perhaps “anomalous” processes is represented by the parameter

$$\beta_j \equiv \frac{\nu_{dj}^0 + \nu_{nj}^0 + \nu_{ionj,nb}^0 + \nu_{ionj}^0 + \nu_{elcx,j}^0 + \nu_{anom,j}^0}{\nu_{jk}^0} \equiv \frac{\nu_{dj}^0 + \nu_{nj}^0 + \nu_{atom,j}^0 + \nu_{anom,j}^0}{\nu_{jk}^0} \equiv \frac{\nu_{dj}^*}{\nu_{jk}^0} \quad (20)$$

where  $\nu_{nj}$  is the frequency for the radial transport of toroidal angular momentum due to inertial effects,  $\nu_{atom,j}^0$  is the frequency for loss of toroidal momentum due to atomic physics processes  $\nu_{anom,j}$  is the frequency for loss of toroidal momentum by “anomalous” processes (e.g. turbulent transport, ripple viscosity).

The gyroviscous momentum transport frequency is defined by

$$\left\langle R^2 \nabla \phi \cdot \nabla \cdot \boldsymbol{\pi}_j \right\rangle_{gv} \approx \frac{1}{2} \tilde{\theta}_j G_j \frac{n_j m_j T_j}{e_j B_\phi} \frac{V_{\phi j}^0}{R} \equiv R n_j m_j \nu_{dj} V_{\phi j}^0 \quad (21)$$

where

$$\tilde{\theta}_j \equiv (4 + \tilde{n}_j^c) \tilde{V}_{\phi j}^s + \tilde{n}_j^s (1 - \tilde{V}_{\phi j}^c) \quad (22)$$

represents poloidal asymmetries and

$$G_j \equiv -\frac{r}{\eta_{4j} V_{\phi j}} \frac{\partial (\eta_{4j} V_{\phi j})}{\partial r} = r (L_n^{-1} + L_T^{-1} + L_{V_\phi}^{-1}) \quad (23)$$

represent radial gradients. We have used the gyroviscosity coefficient  $\eta_{4j} \approx n_j m_j T_j / e_j B$ .

The inertial momentum transport frequency is defined by

$$\begin{aligned} \left\langle R^2 \nabla \phi \cdot n_j m_j (\mathbf{V}_j \cdot \nabla) \mathbf{V}_j \right\rangle &\approx \frac{1}{2} \left( \frac{V_{rj}}{R_o} \left\{ \varepsilon (1 + \tilde{n}_j^c + \tilde{V}_{\phi j}^c) - 2 R_o L_{v\phi,j}^{-1} \right\} - \right. \\ &\left. \varepsilon \frac{V_{\theta j}^0}{R_o} \left\{ \tilde{V}_{\phi j}^s (1 + \tilde{n}_j^c + \tilde{V}_{\theta j}^c) - \tilde{V}_{\theta j}^s (1 + \tilde{V}_{\phi j}^c) - \tilde{V}_{\phi j}^c \tilde{n}_j^s \right\} \right) n_j m_j R V_{\phi j}^0 \equiv R n_j m_j \nu_{nj} V_{\phi j}^0 \end{aligned} \quad (24)$$

## B. Differential Equation Formulation

If the radial gradient scale lengths in the  $\nu_{dj}$  and  $\nu_{nj}$  (in  $\beta_j$ ) in Eqs. (19) are replaced by their definitions  $L_x^{-1} \equiv -(1/x)(dx/dr)$ , then these equations become coupled first order ODEs that must be solved for the  $V_{\phi j}^0$ , together with similar equations for the density and temperature<sup>1</sup>.

Alternatively, it is possible to solve explicitly for the poloidal dependence of the toroidal rotation velocity by expanding the poloidal dependence of the toroidal rotation frequency

$$\Omega_{\phi j}(r, \theta) \equiv \frac{V_{\phi j}}{R} = \Omega_{\phi j}^0(r) + \Omega_{\phi j}^s(r) \sin \theta + \Omega_{\phi j}^c(r) \cos \theta \quad (26)$$

using similar density and poloidal velocity expansions, and flux surface averaging with weighting functions of 1,  $\sin \theta$  and  $\cos \theta$  then leads to three equations for each ion species “j”

$$\begin{aligned}
& \frac{d\Omega_{\phi j}^0}{dr} [R_o V_{rj}] + \frac{d\Omega_{\phi j}^c}{dr} \left[ \frac{\eta_{4j}^0 \tilde{n}_j^s}{2n_j^0 m_j} \right] - \frac{d\Omega_{\phi j}^s}{dr} \left[ \frac{\eta_{4j}^0 (\tilde{n}_j^c + 3)}{2n_j^0 m_j} \right] + \\
& \Omega_{\phi j}^0 \left[ \frac{V_{rj} \varepsilon (2 + \tilde{n}_j^c) + R_o (\bar{v}_{jk} + \bar{v}_{at,j})}{n_j^0} - V_{\theta j}^0 \varepsilon (\tilde{V}_{\theta j}^s + \tilde{n}_j^s) \right] - \Omega_{\phi j}^c \left[ \frac{\eta_{4j}^0}{2n_j^0 m_j} \left( \tilde{n}_j^s (L_{nj}^{-1} + L_{Tj}^{-1}) - \frac{1}{\varepsilon n_j^0} \frac{dn_j^s}{dr} \right) - \right. \\
& \left. \frac{1}{2} \frac{R_o \tilde{S}_j^c}{n_j^0} + V_{\theta j}^0 (\tilde{V}_{\theta j}^s + \tilde{n}_j^s) - V_{rj} \right] + \quad (27) \\
& \Omega_{\phi j}^s \left[ \frac{\eta_{4j}^0}{2n_j^0 m_j} \left( (L_{nj}^{-1} + L_{Tj}^{-1}) (\tilde{n}_j^c + 3) - \frac{4}{r} - \frac{1}{\varepsilon n_j^0} \frac{dn_j^c}{dr} \right) + V_{\theta j}^0 (2 + \tilde{V}_{\theta j}^c + \tilde{n}_j^c) \right] - \Omega_{\phi k}^0 [R_o \bar{v}_{jk}] \\
& = \frac{e_j}{m_j} [E_\phi^A + V_{rj} B_\theta^0] + \frac{M_{\phi j}}{n_j^0 m_j}
\end{aligned}$$

$$\begin{aligned}
& \frac{d\Omega_{\phi j}^0}{dr} \left[ \frac{\eta_{4j}^0 \tilde{n}_j^s}{n_j^0 m_j} + r V_{rj} (\tilde{n}_j^c + 3) \right] + \frac{d\Omega_{\phi j}^c}{dr} [R_o V_{rj}] + \\
& \Omega_{\phi j}^0 \left[ 2V_{rj} + r \bar{v}_{jk} (2 + \tilde{n}_j^c + \tilde{n}_k^c) + r \bar{v}_{at,j} (2 + \tilde{n}_j^c + \tilde{n}_{oj}^c) + \frac{R_o \tilde{S}_j^c}{n_j^0} \right] + \\
& \Omega_{\phi j}^c \left[ R_o (\bar{v}_{jk} + \bar{v}_{at,j}) + \frac{3\eta_{0j}}{n_j^0 m_j q^2 R_o} \right] + \quad (28) \\
& \Omega_{\phi j}^s \left[ \frac{\eta_{4j}^0}{n_j^0 m_j} \left( \frac{L_{Tj}^{-1}}{\varepsilon} + \frac{L_{nj}^{-1}}{\varepsilon} \right) + \frac{V_{\theta j}^0}{\varepsilon} \right] - \Omega_{\phi k}^c [R_o \bar{v}_{jk}] - \Omega_{\phi k}^0 [r \bar{v}_{jk} (2 + \tilde{n}_j^c + \tilde{n}_k^c)] \\
& = \varepsilon \left[ \frac{e_j}{m_j} (E_\phi^A (\tilde{n}_j^c + 1) + V_{rj} B_\theta^0 \tilde{n}_j^c) + \frac{M_{\phi j}}{n_j^0 m_j} \right] + \frac{\eta_{0j}}{n_j^0 m_j R_o} \left( \frac{f_p}{r} \right) V_{\theta j}^0 [\tilde{V}_{\theta j}^c - 2]
\end{aligned}$$

and

$$\begin{aligned}
& \frac{d\Omega_{\phi j}^0}{dr} \left[ r V_{rj} \tilde{n}_j^s - \frac{\eta_{4j}^0 (\tilde{n}_j^c + 3)}{n_j^0 m_j} \right] + \frac{d\Omega_{\phi j}^s}{dr} [R_o V_{rj}] - \Omega_{\phi j}^c \left[ \frac{\eta_{4j}^0}{n_j^0 m_j} \frac{(L_{Tj}^{-1} + L_{nj}^{-1})}{\varepsilon} + \frac{V_{\theta j}^0}{\varepsilon} \right] + \\
& \Omega_{\phi j}^0 \left[ -V_{\theta j}^0 + r (\bar{v}_{jk} (\tilde{n}_j^s + \tilde{n}_k^s) + \bar{v}_{at,j} (\tilde{n}_j^s + \tilde{n}_{oj}^s)) + \frac{R_o \tilde{S}_j^s}{n_j^0} \right] + \quad (29) \\
& \Omega_{\phi j}^s \left[ V_{rj} + R_o (\bar{v}_{jk} + \bar{v}_{at,j}) + \frac{3\eta_{0j}}{n_j^0 m_j q^2 R_o} \right] - \Omega_{\phi k}^0 [r \bar{v}_{jk} (\tilde{n}_j^s + \tilde{n}_k^s)] - \Omega_{\phi k}^s [R_o \bar{v}_{jk}] \\
& = \varepsilon \tilde{n}_j^s \frac{e_j}{m_j} (E_\phi^A + V_{rj} B_\theta^0) + \frac{\eta_{0j}}{n_j^0 m_j R_o} \frac{f_p}{r} V_{\theta j}^0 \tilde{V}_{\theta j}^s
\end{aligned}$$

where  $\tilde{S}_j^{s,c} \equiv (+,-)v_{ion}(n_j^{c,s} + n_{oj}^{c,s})$ . The radial velocity  $V_{rj} = V_{rj}^{class} + V_{rj}^{anom}$ , where the classical term can be calculated from particle, momentum and energy balance<sup>1</sup> and any anomalous momentum transport is assumed to be convective.

## 6. Application to DIII-D

The above formalism, with the gradient scale-length formulation of section 5A, was applied to calculate rotation  $V_\theta$  and  $E_r$  in a few DIII-D shots. Density and temperature profiles and gradient scale lengths were taken from experiment, and the total momentum transfer frequency  $\nu_{dj}^*$  was inferred from experiment by matching the  $V_{\phi j}$  calculated from Eq. (18) to experiment, and then compared with the calculated gyroviscous and atomic transfer frequencies, as shown in Fig. 1. The poloidal velocities are compared with measured values in Fig. 2.

## REFERENCES

1. W. M. Stacey and R. J. Groebner, Phys. Plasmas, 12, 042504 (2005).
2. W. M. Stacey, A. W. Bailey, D. J. Sigmar and K. C. Shaing, Nucl. Fusion, 25, 463 (1985).
3. W. M. Stacey and D. J. Sigmar, Phys. Fluids, 28, 2800 (1985).
4. S. I. Braginskii, Rev. Plasma Phys., 1, 205 (1965).
5. F. L. Hinton and S. K. Wong, Phys. Fluids, 28, 3082 (1985).
6. J. W. Connor, et al., Plasma Phys. Control. Fusion, 29, 919 (1987).
7. A. B. Mikhailovskii and V. S. Tsypin, Sov. J. Plasma Phys., 10, 51 (1984).
8. H. A. Claassen, et al., Phys. Plasmas, 7, 3699 (2000).
9. P. J. Catto and A. N. Simakov, Phys. Phys. Plasmas, 12, 012501 (2005); Plasmas, 10, 4744 (2003); Contrib. Plasma Phys., 44, 83 (2004).

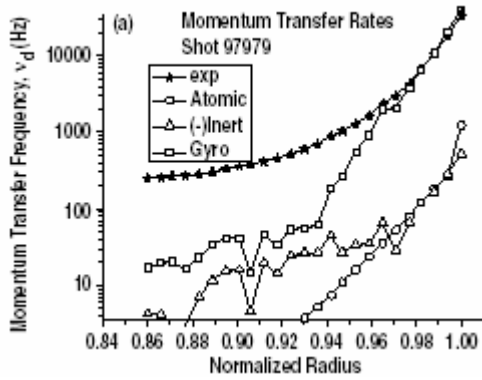


Fig. 1 Experimentally inferred and calculated angular momentum transfer frequencies in DIII-D.

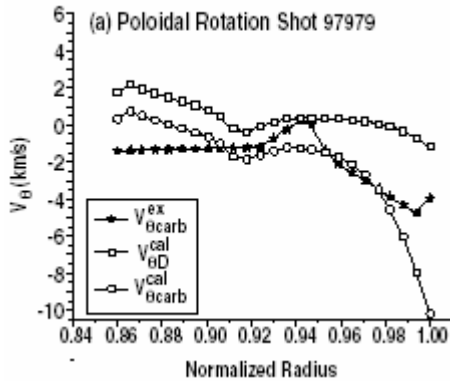


Fig. 2 Measured and calculated poloidal rotation velocities in DIII-D.

### **III. Investigation of the cause of the High-to-Low mode confinement transition following MARFE formation in DIII-D**

(DoE Grant ER54538) W. M. Stacey, Z. W. Friis, T. W. Petrie and A. W. Leonard  
(published in *Physics of Plasmas*, 12, 072518, 2005)

#### **Abstract**

The common observation that the onset of a core MARFE (Multifaceted Asymmetric Radiation From Edge) is followed immediately by a H-L (High-to-Low) confinement mode transition in DIII-D [J. Luxon, Nucl. Fusion, 42, 614 (2002)] was investigated by comparing a theoretical prediction of the threshold non-radiative power across the separatrix needed to maintain H-mode with an experimental determination of the non-radiative power flowing across the separatrix. It was found that in three shots with continuous gas fueling the increased neutral influx associated with the MARFE formation caused a sharp increase in the predicted threshold non-radiative power crossing the separatrix that was required for the plasma to remain in H-mode to a value comparable to the experimental power crossing the separatrix.

#### **Introduction**

A variety of thermal instability phenomena are observed when tokamak discharges are continuously gas-fueled to build up the density, ultimately leading to one or more density limiting phenomena. A typical sequence of events that is observed when the density is increased by continuous gas fueling in a diverted, H-mode plasma has been well documented for DIII-D [e.g. Refs 1-5]: 1) the plasma ‘partially detaches’ (complete detachment near the separatrix strike point on the divertor target and significantly reduced power and particle fluxes to the remainder of the divertor target) and a dense, radiating region forms just in front of the target; 2) with continued fueling the density in front of the divertor target is suddenly reduced, and a dense, cool radiating region (a “divertor MARFE”) is formed upstream in the vicinity of the x-point but outside the separatrix, or LCFS (last closed flux surface), on open field lines; 3) with continued fueling the divertor MARFE appears to gradually move inward across the separatrix to trigger the formation of a radiating region of high density and low temperature on closed field lines in the vicinity of the x-point (an “x-point MARFE”); and immediately thereafter 4) the plasma makes a back transition from H-mode to L-mode confinement. A similar sequence of events has been documented for other experiments<sup>6-10</sup>. The H-L transition constitutes an effective density limit for an H-mode plasma. The proximity of the H-L transition following immediately after the formation of the core MARFE is suggestive of a causative relationship, an investigation of which is the purpose of this paper.

The lines of this investigation are suggested by the well-known existence of a power threshold for the transition from L-mode into H-mode and for another, usually lower, power threshold for remaining in H-mode. The ‘power’ in question is the non-radiative power that flows across the separatrix or last closed flux surface. It seems likely that the formation of a core MARFE may increase the radiative power from inside the separatrix and thus reduce the non-radiative power flowing outward across the separatrix below the threshold value for remaining in H-mode. It is also plausible that events associated with the MARFE may affect the power threshold for remaining in H-mode.

An international database of measured L-H and H-L power thresholds in tokamaks has been compiled and various correlations have been suggested (e.g. Ref. 11). In general, these correlations tend to be based on machine parameters (major and minor radii, magnetic field, etc.) and the line average density. The parameters used in such power threshold predictions do not vary significantly with the formation of a MARFE and thus are not useful for attempting to explain the effect of MARFE formation in producing a H-L transition.

Instead, we will use a recently developed theoretical model for the H-L power threshold<sup>12</sup> which has the advantage for our purposes of being based on edge physics parameters which do vary significantly over the course of MARFE formation. The model is based on the predicted existence of electron and ion temperature radial gradient scale length thresholds for the destabilization of the respective power balances with respect to thermal instabilities with short radial wavelengths which increase the transport in the edge transport barrier. This model, which is described in Ref. 12, has been found to predict both the H-L<sup>13</sup> and L-H<sup>14</sup> power thresholds in several DIII-D discharges.

### **II. Effect of Core MARFE Formation on Proximity to H-L Power Threshold**

The H-L (and L-H) power threshold model<sup>12</sup> used in this paper has the following elements: 1) a model<sup>15</sup> for the growth rate of thermal instabilities with short radial wavelengths in the edge pedestal region, or ‘transport barrier’; 2) an enhancement of transport in the pedestal when thermal instabilities are growing; and 3) the conventional transport heat conduction closure relation among heat fluxes, temperature gradients and transport coefficients. A linear analysis of the stability of the plasma particle, momentum and energy

balance equations in the edge pedestal against two-dimensional (r- $\perp$ ) coupled density, velocity and temperature perturbations with radial wavelength  $k_r^{-1}$  leads to a dispersion relation from which the growth rates (real parts of  $\omega$ ) of such modes can be calculated. This dispersion relation can be solved for a threshold value of the temperature gradient scale length for stabilizing instabilities by setting  $\omega = 0$ , and from this threshold temperature gradient scale length and the heat conduction relation an expression for a separatrix power threshold,  $P_{thresh}$ , can be determined<sup>12</sup>.

We have evaluated the theoretical expression for the power threshold for remaining in H-mode,  $P_{thresh}$ , at several times during three continuously gas fueled DIII-D discharges (Table 1), including well before, just before and just after core MARFE formation. We have also evaluated the non-radiative power,  $P_{sep}^{exp}$ , flowing across the separatrix at the same times.

#### A. Evaluation of $P_{thresh}$

The theoretical prediction of the threshold power for remaining in H-mode is evaluated as the sum of the threshold powers for stabilizing thermal instabilities with radial wavelength  $k_r^{-1}$  in both the ion and electron temperature balances,  $P_{thresh} = P_{thresh,i} + P_{thresh,e}$ , where<sup>12</sup>

$$P_{thresh} = \frac{5}{4} \Gamma_{\perp} T A_{sep} \left[ \sqrt{1 + \frac{(\chi^0 (\alpha - \chi^0 k_r^2) / \nu)}{\left(\frac{5}{4} \frac{\Gamma_{\perp}}{n}\right)^2}} + 1 \right] \quad (1)$$

is the generic form for  $P_{thresh,i}$  or  $P_{thresh,e}$ . The quantity  $\alpha$  refers to terms arising from the atomic physics cooling terms in the ion and electron power balance equations and are given in Ref. 12. The respective ion or electron particle flux across the separatrix ( $\Gamma_{\perp}$ ), density and temperature in the edge transport barrier, H-mode thermal conductivity ( $\chi^0$ ) in the edge transport barrier, and radiation and atomic physics cooling terms must be used to evaluate  $P_{thresh,i}$  and  $P_{thresh,e}$ .  $A_{sep}$  is the separatrix area, and  $\nu$  represents the temperature dependence of  $\chi^0 \sim T^{\nu}$ . We use an average magnitude  $\chi^0 = 0.1 (T/T_0)^{\nu}$  m<sup>2</sup>/s,  $k_r^{-1} = 1$  cm and  $\nu = 2.5$  (an average value for anomalous transport theories<sup>16</sup>), but the results are relatively insensitive to variations in these parameters. The average density and temperature in the edge transport barrier were taken from experiment, as was the average carbon impurity concentration needed to evaluate the radiation term in the electron  $\alpha$ . The neutral densities needed to evaluate the atomic physics cooling terms in the  $\alpha$ 's were calculated as described next.

The ion particle flux across the separatrix,  $\Gamma_{\perp}$ , was determined from particle balance on the plasma core inside the separatrix

$$\Gamma_{\perp} = (S + \Gamma_o^{in} A_{sep} - Vol \times \frac{\partial n^{exp}}{\partial t}) / A_{sep} \quad (2)$$

where  $S$  represents the neutral beam heating particle source and  $\Gamma_o^{in}$  represents the net influx of fueling and recycling neutrals across the separatrix. The outward ion flux was input to a ‘‘2-point’’ divertor model<sup>17</sup> (with radiation and recycling neutrals), which predicted an ion flux to the divertor plate that was used to calculate the recycling source of neutrals at the divertor plate from recycling plasma ions. This recycling neutral source and the neutral fueling sources were then used in a 2D neutral transport calculation<sup>17</sup> to determine  $\Gamma_o^{in}$  and the neutral concentrations in the edge transport barrier needed to evaluate the atomic physics contributions to the  $\alpha$ 's. Experimental values of density and temperature in the edge plasma and values calculated from the ‘‘2-point’’ model for the divertor plasma were used in the

neutral attenuation calculation. The total neutral fueling source was adjusted empirically to take into account wall outgassing sources by requiring the calculation to match the experimental value of the line averaged density, using a pulsed measurement<sup>5</sup> of the particle confinement time (i.e. to calculate the neutral fueling correctly). This procedure has been found to predict local neutral densities in the edge plasma in reasonable agreement with measured values<sup>18</sup>.

### B. Evaluation of $P_{sep}^{exp}$

The non-radiative power crossing the separatrix was determined experimentally from

$$P_{sep}^{exp} = P_{nb} + P_{OH} - P_{rad}^{core} - \partial W_{exp} / \partial t \quad (3)$$

where the subscripts “nb” and “OH” refer to “neutral beam” and “ohmic”, respectively, and  $W_{exp}$  is the measured thermal energy.  $P_{rad}^{core}$  is the radiated power from within the separatrix determined from the bolometer system<sup>19</sup>.

### C. Analysis of DIII-D Discharges

The pedestal values of electron densities, ion and electron temperatures and their gradients needed to evaluate Eqs. (1) and (2) were taken directly from experiment, and the neutral beam particle source was calculated directly from the known beam power. The neutral influx term needed to calculate the outward ion flux across the separatrix,  $\Gamma_{\perp}$ , was calculated as described above. The value of the power flux crossing the separatrix was determined experimentally, as discussed above. Three times in each shot were examined: 1) early in the shot (2500 ms) near the time that the divertor MARFE took place; 2) later in the shot somewhat before the core MARFE formed; and 3) after the core MARFE had formed and immediately before the H-L transition took place. The values of  $P_{sep}^{exp}$ , of the various contributing terms given in Eq. (3), and of  $P_{thresh} = P_{thresh,i} + P_{thresh,e}$  calculated from Eq. (1) are given for the 3 times in each shot in Table 2.

It is clear that  $P_{sep}^{exp} \gg P_{thresh}$  early in the shot and up to just before the onset of the core MARFE (the first 2 times) and that  $P_{sep}^{exp} \approx P_{thresh}$  following core MARFE formation and immediately prior to the H-L transition (third time) for all 3 shots. The interesting result is that this pattern is caused more by a sharp increase in  $P_{thresh}$  after core MARFE formation more than by any sharp decrease in  $P_{sep}^{exp}$  accompanying core MARFE formation (the anticipated cause). In fact,  $P_{sep}^{exp}$  did decrease strongly with core MARFE formation due to the anticipated increase in  $P_{rad}$  for shot 92976, but the increase in  $P_{rad}$  was partially compensated by an increase in  $P_{OH}$  in shot 92972 and more than offset by the combination of a large increase in  $P_{OH}$  and a decrease in  $-dW_{exp}/dt$  in shot 96887. It should be noted that because of the spatial resolution and finite grid size of the bolometer system there is an uncertainty in the determination of the amount of radiation from the vicinity of the X-point that is actually inside the separatrix, so that an error bar in  $P_{rad}$  of about 0.1 MW is associated with the later times in the first two shots and of about 0.5 MW is associated with the later times in shot 96887.

The quantities in Eq. (1) for  $P_{thresh}$  which change with time during the shots are tabulated in Table 3. It is clear from the table that the neutral influx ( $S_{recycle} = \Gamma_o^{in} A_{sep}$ ), hence the neutral concentration in the edge ( $f_o$ ), increases with time in general and increases sharply at the time of core MARFE formation. The increase in neutral influx produces an increase in the ion outflux across the separatrix, as given by Eq. (2), and causes an increase in both the neutral and electron densities in the pedestal. The increased neutral density in the pedestal increases the ionization, charge-exchange and scattering rates in the pedestal,  $\nu_{ion} \equiv n_o \langle \sigma v \rangle_{ion}$  and  $\nu_{at} \equiv n_o^{cold} (\langle \sigma v \rangle_{cx} + \langle \sigma v \rangle_{elast})$ , which generally causes an increase in the atomic physics terms  $\alpha_e$  and  $\alpha_i$ . An increase in neutral concentration in the edge also causes an increase in the carbon radiation emissivity, which causes an increase in  $\alpha_e$ .



We conclude from these results that the increased neutral influx associated with the MARFE formation causing a sharp increase in the threshold non-radiative power crossing the separatrix that is required for the plasma to remain in H-mode is a principal mechanism triggering the back H-L transitions that are observed to follow MARFE formation in DIII-D. The onset of MARFE formation is also predicted to be strongly influenced by the penetration of recycling and fueling neutrals into the plasma edge in DIII-D<sup>20</sup> and other tokamaks (e.g. TEXTOR<sup>21</sup>). The extent to which this increase in neutral influx is caused by core MARFE formation, as distinguished from merely associated with it, remains an open question.

## Appendix: Thermal Instability Modeling

As discussed previously, an important aspect of this analysis is the modeling of the divertor plasma properties and of the related transport of fueling and recycling neutrals in the divertor and into the plasma edge, because the prediction of the threshold power for staying in the H-mode depends on the neutral influx across the separatrix and on the neutral density in the edge transport barrier. In addition to the edge thermal instability on which the power threshold analysis used in this paper was based, there are (at least) two other thermal instabilities that also depend on the modeling of the divertor (divertor MARFE) and of the neutral transport inward across the separatrix into the edge transport barrier (core MARFE).

We have previously carried out thermal instability analyses leading to predictive algorithms for the onset of divertor and core MARFEs, the comparison of which with observed experimental manifestation of the instabilities in DIII-D are summarized in Ref. 20. For the divertor MARFE, a prediction of the growth rate of parallel density and temperature perturbations along the field lines in the divertor channel,  $\omega_{DIV}$ , was developed which is sensitive to the divertor densities, temperatures and geometry. For the core MARFE, a prediction of the maximum density for which the plasma in the edge transport barrier is stable against poloidal perturbations in density and temperature was developed in terms of the temperature, atomic and impurity cooling rates, and cross-field heat fluxes into the scrape-off layer. This core MARFE prediction is sensitive to the neutral influx into the edge transport barrier. Both of these predictions have previously been found to be in agreement with observation of the respective thermal instability onset<sup>20</sup>.

Thus, an indirect check of the modeling procedure used in evaluating the power threshold for the H-L transition is a comparison of the prediction of thermal instability onset,  $\omega_{DIV} > 0$  and  $MI \equiv n_{edge}^{exp} / n_{edge}^{MARFE} > 1$ , with experimental observation of divertor and core, respectively, MARFE onset. These quantities are predicted as part of the overall calculation for each time in each shot, as shown in Table 4. Clearly the onset conditions (times) for divertor and core MARFEs are predicted for these shots. The onset conditions for the core MARFEs in these discharges were strongly influenced by the penetration of recycling and fueling neutrals into the edge plasma.

## References

1. T. W. Petrie, D. Buchenauer, D. N. Hill, *et al.*, J. Nucl. Mater. 196-198, 848 (1992)
2. T. W. Petrie, A. G. Kellman and M. A. Mahdavi, Nucl. Fusion, 33, 929 (1993).
3. T. W. Petrie, D. N. Hill, S. L. Allen, *et al.*, Nucl. Fusion, 37, 321 (1997).
4. T. W. Petrie, S. L. Allen, T. N. Carlstrom, *et al.*, J. Nucl. Mater. 241-243, 639 (1997).
5. R. Maingi, M. A. Mahdavi, T. C. Jernigan, *et al.*, Phys. Plasmas, 4, 1752 (1997).
6. G. F. Matthews, J. Nucl. Mater., 220-222, 104 (1995)
7. W. Suttrop, V. Mertens, H. Murmann, *et al.*, J. Nucl. Mater., 266-269, 118 (1999).
8. A. Loarte, R. D. Monk, J. R. Martin-Soles, *et al.*, Nucl. Fusion, 38, 331 (1998).
9. N. Hosogane, K. Itami, N. Asakura, *et al.*, J. Nucl. Mater., 220-222, 420 (1995).
10. B. Lipschultz, J. Goetz, B. LaBombard, *et al.*, J. Nucl. Mater., 220-222, 50 (1995).
11. J. A. Snipes and the International H-mode Threshold Database Working Group, Plasma Phys. Control. Fusion, 42, A299 (2000).
12. W. M. Stacey, Phys. Plasmas, 9, 3082 (2002).

13. W. M. Stacey and T. W. Petrie, Phys. Plasmas, 10, 3949 (2003).
14. W. M. Stacey, Phys. Plasmas, 11, 686 (2004).
15. W. M. Stacey, Phys. Plasmas, 6, 2452 (1999).
16. J. J. Martinell, J. A. Almaguer and J. J. E. Herrera, Plasma Phys. Control. Fusion, 34, 977 (1992).
17. W. M. Stacey, Phys. Plasmas, 5, 1015 (1998) and 8, 3673 (2001).
18. W. M. Stacey, Nucl. Fusion, 40, 965 (2000).
19. A. W. Leonard, W. H. Meyer, B. Geer, *et al.*, Rev. Sci. Instr., 66, 1201 (1995).
20. W. M. Stacey, Phys. Plasmas, 9, 2692 (2002).
21. M. Z. Tokar and F. A. Kelly, Phys. Plasmas, 10, 4378 (2003).

**Table 1.** Parameters of gas fueled D-IIIID shots that underwent a H-L transition immediately following core MARFE formation. (The ion  $B \times \nabla B$  drift is towards the X-point in all shots.)

Shot #	Times (ms)	$I_p$ (MA)	$B(T)$	q95	$P_{NBI}$ (MW)	$n_{eped}$ ( $e19/m^3$ )	$T_{eped}$ (eV)	$nebar$ ( $e19/m^3$ )
92976	2500 to 3212	1.0	2.1	6.2	5.2	4.1 to 4.4	218 to 187	5.0 to 6.1
92972	2500 to 3325	1.0	1.1	3.2	5.0	5.5 to 6.2	414 to 168	6.3 to 8.4
96887	2500 to 3650	1.7	2.1	3.2	8.5	9.6 to 11.3	440 to 231	10.1 to 12.7

**Table 2.**  $P_{thresh}^{theory}$  and  $P_{sep}^{exp}$  evolution during three DIII-D shots that underwent H-L transitions following core MARFEs (units MW).

T I M E ↓ ↓ ↓ ↓ ↓ ↓ ↓ ↓ ↓ ↓	<b>92976</b>	$P_{rad}$	$P_{NBI}$	$\frac{dW}{dt}$	$P_{OH}$	$P_{sep}^{exp}$	$P_{thresh}$
	<i>TIME(ms)</i>						
	2500	.54	5	0	.30	<b>4.8</b>	<b>2.5</b>
	2962-3000	DIVERTOR MARFE					
	3000	.39	5	0	.58	<b>5.2</b>	<b>3.0</b>
	3050-3100	CORE MARFE					
	3212	1.4	5	0	.63	<b>4.2</b>	<b>4.1</b>
	3230	H-to-L TRANSITION					
	<b>92972</b>	$P_{rad}$	$P_{nbi}$	$\frac{dW}{dt}$	$P_{OH}$	$P_{sep}^{exp}$	$P_{thresh}$
	<i>TIME(ms)</i>						
T I M E ↓ ↓ ↓ ↓ ↓ ↓ ↓ ↓ ↓ ↓	2500	.62	5.2	0	.35	<b>4.9</b>	<b>3.5</b>
	2750-2790	DIVERTOR MARFE					
	3000	.87	5.2	0	.45	<b>4.8</b>	<b>3.7</b>
	3190	CORE MARFE					
	3325	1.29	5.2	0	.55	<b>4.5</b>	<b>4.6</b>
	3323	H-to-L TRANSITION					
	<b>96887</b>	$P_{rad}$	$P_{nbi}$	$\frac{dW}{dt}$	$P_{OH}$	$P_{sep}^{exp}$	$P_{thresh}$
	<i>TIME(ms)</i>						
	2390	DIVERTOR MARFE					
	2500	.8	8.5	0	.21	<b>7.9</b>	<b>6.1</b>
T I M E ↓ ↓ ↓ ↓ ↓ ↓	3200	1.09	8.5	-.46	.37	<b>8.2</b>	<b>6.8</b>
	3240	CORE MARFE					
	3650	1.2	8.5	-.23	.95	<b>8.5</b>	<b>8.8</b>
	3653	H-to-L TRANSITION					

**Table 3.** Evolution of edge pedestal parameters during three DIII-D shots that underwent H-L transitions following a core MARFE.

T I M E ↓ ↓ ↓ ↓	<b>92976</b>	$S_{\text{recyc}}(10^{20}/\text{s})$	$n_{\text{ped}}(10^{20}\text{m}^{-3})$	$T_{\text{eped}}(\text{eV})$	$F_0(\%)$	$\alpha_i(10^3\text{s}^{-1})$	$\alpha_e(10^3\text{s}^{-1})$	$\Gamma_{\perp}(10^{20}/\text{m}^2\text{s})$
	<i>TIME(ms)</i>							
	2500	.64	.41	218	.84	.37	.40	1.6
	2962-3000	DIVERTOR MARFE						
	3000	1.4	.43	212	1.7	.88	1.3	3.0
	3050-3100	CORE MARFE						
	3212	3.9	.44	187	3.7	2.3	2.4	6.9
	3230	H-to-L TRANSITION						
T I M E ↓ ↓ ↓ ↓	<b>92972</b>	$S_{\text{recyc}}(10^{20}/\text{s})$	$n_{\text{ped}}(10^{20}\text{m}^{-3})$	$T_{\text{eped}}(\text{eV})$	$F_0(\%)$	$\alpha_i(10^3\text{s}^{-1})$	$\alpha_e(10^3\text{s}^{-1})$	$\Gamma_{\perp}(10^{20}/\text{m}^2\text{s})$
	<i>TIME(ms)</i>							
	2500	.40	.59	414	.48	.26	.29	1.1
	2750-2790	DIVERTOR MARFE						
	3000	1.1	.62	212	.91	.48	1.0	2.7
	3190	CORE MARFE						
	3325	7.2	.55	168	2.3	1.6	1.6	12
	3323	H-to-L TRANSITION						
T I M E ↓ ↓ ↓ ↓	<b>96887</b>	$S_{\text{recyc}}(10^{20}/\text{s})$	$n_{\text{ped}}(10^{20}\text{m}^{-3})$	$T_{\text{eped}}(\text{eV})$	$F_0(\%)$	$\alpha_i(10^3\text{s}^{-1})$	$\alpha_e(10^3\text{s}^{-1})$	$\Gamma_{\perp}(10^{20}/\text{m}^2\text{s})$
	<i>TIME(ms)</i>							
	2390	DIVERTOR MARFE						
	2500	2.1	.99	440	.46	.45	.46	5.3
	3200	2.5	.96	450	.56	.54	.55	6.1
	3240	CORE MARFE						
	3650	6.7	1.13	231	.70	.90	1.1	13
	3653	H-to-L TRANSITION						

**Table 4.** Divertor and core MARFE prediction and observation in three DIII-D shots that underwent H-L transitions following core MARFE formation.

T I M E ↓ ↓ ↓	92976	$\omega_{DIV}(10^5/s)$	$MI=n_{exp}/n_{marfe}$
	TIME(ms)		
	2500	-93	.23
	2962-3000	DIVERTOR MARFE	
	3000	25	.65
	3050-3100	CORE MARFE	
	3212	46	1.8
	3230	H-to-L TRANSITION	
	92972	$\omega_{DIV}(10^5/s)$	$MI=n_{exp}/n_{marfe}$
	TIME(ms)		
T I M E ↓ ↓ ↓	2500	-36	.39
	2750-2790	DIVERTOR MARFE	
	3000	-4.8	.80
	3190	CORE MARFE	
	3325	27	1.5
	3323	H-to-L TRANSITION	
	96887	$\omega_{DIV}(10^5/s)$	$MI=n_{exp}/n_{marfe}$
	TIME(ms)		
T I M E ↓ ↓ ↓	2390	DIVERTOR MARFE	
	2500	14	.43
	3200	22	.53
	3240	CORE MARFE	
	3650	65	2.2
	3653	H-to-L TRANSITION	

## IV. Calculation of toroidal rotation profiles in DIII-D using neoclassical viscosity (DoE Grant ER54538)

W. M. Stacey, R. W. Johnson and J. Mandrekas

(to be published in *Physics of Plasmas*, 2006)

### Abstract

Momentum and particle balance and neoclassical viscosity were applied to calculate the radial profile of toroidal rotation in several DIII-D [J. Luxon, Nucl. Fusion, 42, 614 (2002)] discharges in a variety of energy confinement regimes (Low-mode, Low-mode with Internal Transport Barrier, High-mode, and High-mode with Quiescent Double Barrier). Calculated toroidal rotation velocities were found to over-predict measured values most in the center—by factors of 1.5 to 3—with the over-prediction generally decreasing with increasing radius, for the L, H and ITB mode shots, but the single impurity species approximation could not properly model the multiple Ni and Cu charge states in the QDB shots.

### I. Introduction

There have been longstanding experimental<sup>1-10</sup> and theoretical<sup>11-27</sup> efforts to characterize and understand toroidal rotation and the related radial transport of angular momentum in neutral beam driven tokamaks. Since the theoretical expression for the toroidal rotation velocity follows directly from toroidal momentum balance once the viscous stress is specified, understanding toroidal rotation is primarily a matter of understanding toroidal viscosity.

It was early noted that the familiar “perpendicular” viscosity of classical theory was much too small to account for observed momentum damping<sup>1,13-15</sup>, even when extended to take neoclassical effects into account<sup>13-15,18,19</sup>, giving rise to the now widespread belief that momentum transport in tokamaks was “anomalous”. The observation in several recent experimental investigations<sup>4,5,7,8,10,28</sup> that the ratio of the inferred momentum diffusivity and ion thermal diffusivity ( $\chi_\phi/\chi_i$ ), or the ratio of parameters that are determined by these diffusivities, was relatively uniform over the radial dimension of the plasma was interpreted as further evidence that the momentum transport was anomalous, since the ion thermal transport was believed to be anomalous in these discharges.

It was also early pointed out<sup>11,12</sup> (but little noted) that there was a second, gyroviscous contribution to the radial transport of angular momentum in classical theory with a gyroviscosity coefficient that was several orders of magnitude larger than the perpendicular viscosity coefficient. The relative obscurity of the gyroviscous contribution in momentum transport analyses (it has long been included in extended MHD codes such as NIMROD and M3D) is perhaps due in part to the fact that it vanishes in cylindrical geometry (hence would not have survived in much of the early theoretical work) and in part by its puzzling failure to survive in some contemporary developments of neoclassical viscosity based on a formal gyroradius ordering of the flow fields<sup>18,19,26</sup>, which essentially recovered the much smaller classical perpendicular viscosity with small corrections. In any case, there would now appear to be a firm theoretical basis for gyroviscosity<sup>11,12,16,17,20-25,27</sup>. It is our purpose in this paper to test neoclassical viscosity by using neoclassical gyroviscosity to calculate the radial profile of toroidal rotation velocity and neoclassical parallel viscosity to poloidal density and velocity asymmetries that are needed to evaluate the gyroviscous torque for comparison with measured values in a set of DIII-D discharges.

We would anticipate that there are other, non-classical momentum transport mechanisms present in DIII-D (and other) discharges (e.g. Ref. 29). However, since the particle motions and forces that give rise to classical and neoclassical transport are always present (trapped particle effects only in the appropriate collisionality regimes), it is important to make a comparison of the predictions of neoclassical momentum transport theory with rotation measurements in order to establish the magnitude of the additional transport that must be accounted for by these other transport mechanisms.

For this purpose, we make use of the practical computation formalism that has been developed by extending the Braginskii gyroviscosity formalism to tokamak toroidal flux surface geometry<sup>17</sup> (i.e. the “Pfirsch-Schluter” extension of classical gyroviscosity) and by developing a methodology for evaluating the poloidal asymmetry factors needed to determine the rate of radial transport of toroidal angular momentum<sup>20</sup>. A number of previous, less extensive, comparisons of this formalism with experimental data<sup>30-32</sup> have established that gyroviscosity predicts the magnitude of the global momentum loss rate (the

momentum confinement time) in many neutral beam driven tokamaks and under a variety of operating conditions. The intent of this paper is to extend these investigations to test the ability of this gyroviscosity formalism to predict the radial profile, as well as the overall magnitude, of the radial transport rate of toroidal angular momentum for neutral beam driven DIII-D plasmas in a variety of energy confinement regimes.

Radial momentum transport in tokamak plasmas is of intrinsic interest, of course, for what it reveals about basic transport processes. Moreover, toroidal rotation has also been shown to affect neoclassical particle transport<sup>33,34</sup>, to suppress MHD resistive wall mode instabilities<sup>35-37</sup>, and to alter MHD equilibria<sup>38</sup>, and is postulated to be involved in the shear suppression of transport enhancing microinstabilities<sup>39</sup>.

## II. Neoclassical Radial Transport of Toroidal Angular Momentum

### A. Viscous torques

Following the previous generalization<sup>17</sup> of the Braginskii<sup>12</sup> derivation to toroidal flux-surface geometry, the toroidal component of the viscous torque can be written

$$R^2 \nabla \phi \cdot \nabla \cdot \Pi = \frac{1}{R h_p} \frac{\partial}{\partial l_\psi} (R^2 h_p \Pi_{\psi\phi}) + B_p \frac{\partial}{\partial l_p} \left( \frac{R \Pi_{p\phi}}{B_p} \right) \quad (1)$$

where the  $\Pi_{pq}$  are the stress tensor elements that result from the Braginskii decomposition of the rate-of-strain tensor extended to a right-hand ‘radial’, ‘poloidal’, toroidal  $(\psi, p, \phi)$  flux-surface coordinate system with length elements  $(dl_\psi = h_\psi d\psi, dl_p = h_p dp, dl_\phi = h_\phi d\phi)$ . The viscous stress tensors have ‘perpendicular’ components

$$\Pi_{\psi\phi}^\perp = -\eta_2 R \frac{\partial}{\partial l_\psi} \left( \frac{V_\phi}{R} \right), \Pi_{p\phi}^\perp = -\eta_2 R \frac{\partial}{\partial l_p} \left( \frac{V_\phi}{R} \right) \quad (2)$$

gyroviscous components

$$\Pi_{\psi\phi}^{\text{gv}} = -\eta_4 R \frac{\partial}{\partial l_p} \left( \frac{V_\phi}{R} \right), \Pi_{p\phi}^{\text{gv}} = -\eta_4 R \frac{\partial}{\partial l_\psi} \left( \frac{V_\phi}{R} \right) \quad (3)$$

and ‘parallel’ viscous components

$$\Pi_{\psi\phi}^\parallel = 0, \Pi_{p\phi}^\parallel = -\frac{3}{2} \eta_0 f_p A_0 \quad (4)$$

where

$$A_0 = 2 \left\{ -\frac{1}{3} \left( \frac{\partial V_p}{\partial l_p} \right) + \left[ \left( \frac{1}{R} \right) \frac{\partial R}{\partial l_p} + \frac{1}{3} \left( \frac{1}{B_p} \right) \frac{\partial B_p}{\partial l_p} \right] V_p + f_p R \frac{\partial \left( \frac{V_\phi}{R} \right)}{\partial l_p} \right\} \quad (5)$$

and  $f_p = B_p / B_\phi$ .

The Braginskii values of the viscosity coefficients in a collisional plasma are

$$\eta_0 \simeq nT\tau, \eta_4 \simeq nTm / ZeB = \eta_0 / \Omega\tau, \eta_2 \simeq \eta_4 / \Omega\tau \simeq \eta_0 / (\Omega\tau)^2 \quad (6)$$

where  $\tau$  is the self-collision time and  $\Omega = m/ZeB$  is the gyrofrequency. Since typically  $\Omega\tau \approx 10^3 - 10^4$ ,  $\eta_0 \gg \eta_4 \gg \eta_2$ . Taking into account trapped particle effects that would occur at lower collisionality should not directly effect  $\eta_4$ , which has no  $\tau$ -dependence, and has been shown<sup>18,19</sup> to have very little effect on  $\eta_2$ . However, trapped particle effects at lower collisionality have a major effect on  $\eta_0$ , which we represent as<sup>31</sup>

$$\eta_{0j} = \frac{n_j m_j v_{thj} q R \varepsilon^{-3/2} v_{jj}^*}{(1 + \varepsilon^{-3/2} v_{jj}^*)(1 + v_{jj}^*)} \equiv n_j m_j v_{thj} q R f_j(v_{jj}^*) \quad (7)$$

where  $v_{jj}^* = v_{jj} q R / v_{thj}$ ,  $v_{thj}$  is the thermal speed,  $q$  is the safety factor, and  $\varepsilon = r/R$ .

Since the flux surface average of the second term in Eq.(1) vanishes identically, and the ‘parallel’ component of the first term in Eq. (1) vanishes identically, the flux surface averaged toroidal viscous torque may be written as the sum of the gyroviscous and perpendicular viscous components

$$\langle R^2 \nabla \phi \cdot \nabla \cdot \Pi \rangle = \langle R^2 \nabla \phi \cdot \nabla \cdot \Pi \rangle_{gv} + \langle R^2 \nabla \phi \cdot \nabla \cdot \Pi \rangle_{\perp} \quad (8)$$

where

$$\langle R^2 \nabla \phi \cdot \nabla \cdot \Pi \rangle_{gv} = - \left\langle \frac{1}{R h_p} \frac{\partial}{\partial l_{\psi}} \left( R^3 h_p \eta_4 \frac{\partial}{\partial l_p} (V_{\phi}/R) \right) \right\rangle \quad (9)$$

and

$$\langle R^2 \nabla \phi \cdot \nabla \cdot \Pi \rangle_{\perp} = - \left\langle \frac{1}{R h_p} \frac{\partial}{\partial l_{\psi}} \left( R^3 h_p \eta_2 \frac{\partial}{\partial l_{\psi}} (V_{\phi}/R) \right) \right\rangle \quad (10)$$

If the plasma rotated as a rigid body,  $\Omega \equiv V_{\phi}/R \neq \Omega(\psi, p)$ , then both of these components of the viscous torque would vanish identically. It is departure from rigid body rotation in the flux surface,  $\Omega = \Omega(p)$ , that drives the gyroviscous torque, and departure from rigid body rotation radially,  $\Omega = \Omega(\psi)$ , that drives the perpendicular viscous torque. Although the radial departure of the toroidal rotation velocity from rigid body rotation is generally larger by an order of magnitude or more than the poloidal departure of the toroidal rotation velocity from rigid body rotation in the flux surface, the gyroviscosity coefficient is larger than the perpendicular viscosity coefficient by 3-4 orders of magnitude,  $\eta_4 \approx (\Omega\tau)\eta_2 \approx (10^3 - 10^4)\eta_2$ , so that the gyroviscous toroidal torque is generally a couple of orders of magnitude larger than the perpendicular toroidal viscous torque. We note again that it is the smaller, perpendicular toroidal viscous torque to which several authors were referring when they stated that the neoclassical viscosity is too small to account for experimentally observed rotation damping.

Finally, we further note that it has been suggested<sup>23</sup> that the above expression for the gyroviscous toroidal torque, which is based on the Braginskii development of the viscous stress tensor, may overestimate the momentum transport rate in regions of steep pressure gradients and low toroidal rotation (e.g. the plasma edge pedestal) because of the  $V_{\phi} \sim v_{th}$  ordering of the Braginskii derivation<sup>12</sup>. Mikhailovskii and Tsypin<sup>16</sup> were the first, and Catto and Simakov<sup>27</sup> the most recent, to repeat the Braginskii derivation in the  $V_{\phi} \ll v_{th}$  ordering. Braginskii’s derivation, which is used in this paper, is valid if the fluid velocities in the directions perpendicular and parallel to  $\mathbf{B}$  are larger than the diamagnetic velocity and the diamagnetic velocity multiplied by  $B_{\phi}/B_p$ , respectively<sup>25</sup>. If this condition is not satisfied, then a heat flux term may be required also in the parallel, perpendicular and gyroviscous torque expressions<sup>25,27</sup>. This ‘large rotation’ condition for the validity of the Braginskii ordering appears to be valid over most of the radius for the discharges considered in this paper, as will be discussed later.

## B. Toroidal viscous torque approximate representation



In order to obtain an approximate model for numerically evaluating the gyroviscous torque on each flux surface separately, we specialize to toroidal geometry, use the representations  $B = B^0/(1 + \varepsilon \cos \theta)$ ,  $R = R_0(1 + \varepsilon \cos \theta)$ , replace the radial gradients in Eq. (9) by radial gradient scale lengths (e.g.  $L_n^{-1} = -1/n \partial n / \partial r$ ) which will be evaluated from experiment in this paper, and expand the poloidal dependence of densities and velocities in a low-order Fourier series of the form

$$n_j(r, \theta) = n_j^0 \left[ 1 + n_j^c(r) \cos \theta + n_j^s(r) \sin \theta \right] \quad (11)$$

to obtain a representation of the toroidal viscous torque in terms of an angular momentum transfer, or “drag”, frequency,  $\nu_{dj}$

$$\left\langle R^2 \nabla \phi \cdot \nabla \cdot \pi_j \right\rangle_{gv} = \frac{1}{2} \tilde{\theta}_j G_j \frac{n_j m_j T_j}{e_j B_\phi} \frac{V_{\phi j}^0}{R} \equiv R n_j m_j \nu_{dj} V_{\phi j}^0 \quad (12)$$

where

$$\begin{aligned} \tilde{\theta}_j &\equiv (4 + \tilde{n}_j^c) \tilde{V}_{\phi j}^s + \tilde{n}_j^s (1 - \tilde{V}_{\phi j}^c) \\ &= (4 + \tilde{n}_j^c) \left( -(\hat{V}_{\theta j} / \hat{V}_{\phi j}) (\tilde{\Phi}^s + \tilde{n}_j^s) + \tilde{\Phi}^s \left( 1 + \left( \hat{P}_j' / \hat{V}_{\phi j} \right) \right) \right) + \\ &\tilde{n}_j^s \left( (\hat{V}_{\theta j} / \hat{V}_{\phi j}) (\tilde{\Phi}^c + \tilde{n}_j^c + 2) - \tilde{\Phi}^c \left( 1 + \left( \hat{P}_j' / \hat{V}_{\phi j} \right) \right) \right) \end{aligned} \quad (13)$$

represents poloidal asymmetries and

$$G_j \equiv -\frac{r}{\eta_{4j} V_{\phi j}} \frac{\partial (\eta_{4j} V_{\phi j})}{\partial r} = r (L_n^{-1} + L_T^{-1} + L_{V_\phi}^{-1}) \quad (14)$$

represent radial gradients. We have used the gyroviscosity coefficient  $\eta_{4j} \approx n_j m_j T_j / e_j B$  and introduced the notation

$$\hat{V}_{\theta j} \equiv \frac{V_{\theta j}^0}{f_p \nu_{thj}}, \hat{V}_{\phi j} \equiv \frac{V_{\phi j}^0}{\nu_{thj}}, \hat{P}_j' \equiv \frac{1}{n_j^0 e_j B_\theta^0 \nu_{thj}} \frac{\partial \overline{p_j}}{\partial r}, f_p \equiv \frac{B_\theta}{B_\phi}, \tilde{n}_j^{c/s} \equiv \frac{n_j^{c/s}}{\varepsilon}, \tilde{\Phi}^{c/s} \equiv \frac{\Phi^{c/s}}{\varepsilon} = \frac{n_e^{c/s}}{\varepsilon (e\Phi / T_e)} \quad (15)$$

with the last relation following from electron momentum balance, and neglected radial gradients in the density asymmetry coefficients  $n_j^{c,s}$ . The radial gradient scale lengths needed to evaluate the  $G_j$  from Eq. (14) are taken from experiment in this paper.

### C. “Neoclassical” terminology and collisionality dependence

The terminology “neoclassical” is used differently by various authors, and the collisionality dependence of the neoclassical viscosity is subtle, so a brief discussion of both is in order. Transport due to collisions in straight field-line geometry (e.g. cylinders) is referred to as “classical” transport. Kaufman<sup>11</sup> and Braginskii<sup>12</sup> worked out a “classical” theory of viscosity. In the more familiar case of Braginskii, the viscosity was derived from kinetic theory under the assumption of large collisionality and large rotation  $V_\phi \sim \nu_{th}$ .

Extension of “classical” Braginskii collisional transport to include the effects of toroidal geometry is referred to in this paper, but not by all authors, as “neoclassical” transport (i.e. Pfirsch-Schluter transport). In general, collisional transport in toroidal geometry includes the “classical” transport plus the new “neoclassical” transport effects due to the toroidal geometry. Since the latter effects are larger, the “classical” transport is usually neglected in toroidal geometry relative to the new Pfirsch-Schluter “neoclassical” transport, but it is still there (i.e. the forces producing it are still operable).

Mikhailovskii and Tyspin<sup>16</sup>, Stacey and Sigmar<sup>17</sup> and recently Catto and Simakov<sup>27</sup> extended “classical” viscosity theory to toroidal geometry to obtain what we refer to in this paper as a “neoclassical viscosity” theory that takes into account Pfirsch-Schluter-like toroidal geometry effects.

We note that this “Pfirsch-Schluter gyroviscosity” vanishes to leading order in the absence of an up-down asymmetry in either the density or the toroidal rotation velocity<sup>17</sup>, as shown explicitly in Eq. (13), but survives at higher order<sup>27</sup>. This does not mean that gyroviscosity vanishes in a tokamak with an up-down symmetric magnetic field structure, because inertial and other effects can produce up-down density and rotation velocity asymmetries even in tokamaks with an up-down symmetric magnetic field structure<sup>20,30-32</sup>. Catto and Simakov<sup>27</sup> recently concluded purely on theoretical grounds that sufficiently strong up-down asymmetries such as found in diverted plasmas could drive gyroviscous momentum transport rates comparable to those observed experimentally, but did not note that similarly strong up-down asymmetries could be produced by inertial and other effects (see Fig. 3).

At sufficiently small collisionality, trapped particle effects introduce additional transport effects in toroidal geometry that are usually larger than the Pfirsch-Schluter transport effects (at least for the more familiar heat conductivities), although the latter (and also the “classical” transport effects) are still present because most of the particles are untrapped. We refer to the transport associated with these trapped particle effects also as “neoclassical” transport, while noting that some authors refer to it as “banana-plateau” transport, and that yet other authors refer to only these trapped particle transport effects as “neoclassical”. Numerous authors have investigated trapped particle effects on the parallel component of the viscosity tensor and found them to cause a significant enhancement of the viscosity coefficient [Eq. (7) is one such example], but of course to exist only when the collisionality was small enough to allow a small number of trapped particles to execute trapped particle orbits. Hinton and Wong<sup>18</sup> (and others) worked out the trapped particle effects on the perpendicular component of the viscosity and found only a small enhancement over the “classical” Braginskii value.

The Pfirsch-Schluter-like “neoclassical gyroviscosity” of this paper does not have any explicit collisionality dependence, and no one has suggested that there is any direct trapped particle effect on gyroviscosity, to our knowledge. This does not mean that the Pfirsch-Schluter-like gyroviscosity does not exist in low collisionality plasmas, only that trapped particle effects do not directly enhance gyroviscosity relative to the “neoclassical Pfirsch-Schluter” values produced by toroidal geometry effects. However, since trapped particle effects enhance the parallel component of viscosity [Eq. (7)] that is used in solving the poloidal momentum moments equations [Eqs. (19)-(22)] for the poloidal velocities and density asymmetries needed to evaluate the gyroviscous torque from Eqs. (12)-(14), there is an indirect trapped particle collisionality dependence of gyroviscosity that is taken into account in the calculation of this paper.

#### D. Poloidal rotation velocities and density asymmetries

Evaluation of the poloidal asymmetry factors  $\tilde{\theta}_j$  of Eq. (13) requires the solution of the poloidal momentum balance equations for the poloidal rotation velocities and the poloidal density asymmetries.

The poloidal component of the momentum balance equation is

$$n_j m_j \left[ (\mathbf{V}_j \cdot \nabla) \mathbf{V}_j \right]_\theta + \left[ \nabla \cdot \Pi_j \right]_\theta + \frac{1}{r} \frac{\partial p_j}{\partial \theta} - M_{\theta j} - F_{\theta j} + n_j e_j (V_{rj} B_\phi - E_\theta) = 0 \quad (16)$$

where the poloidal components of the inertial and viscous terms are

$$n_j m_j \left[ (\mathbf{V}_j \cdot \nabla) \mathbf{V}_j \right]_\theta = n_j m_j \left[ V_{rj} \frac{\partial V_{\theta j}}{\partial r} + \frac{V_{rj} V_\theta}{r} + \frac{1}{2} \frac{1}{r} \frac{\partial V_{\theta j}^2}{\partial \theta} + \frac{V_{\phi j}^2}{R} \sin \theta \right] \quad (17)$$

and

$$\left[ \nabla \cdot \Pi_j \right]_\theta = n_{0j} \left( \frac{1}{2} A_{\theta j} \right) \left\{ \frac{1}{r} \frac{\partial \ln(\eta_{0j} A_{\theta j})}{\partial \theta} - 3 \frac{\sin \theta}{R} \right\} \quad (18)$$

where  $M$  and  $F$  represent external momentum input from the neutral beam injection and interspecies collisional friction, respectively. We note that the “parallel” component of the viscosity enters the rotation calculation at this point and ultimately affects the calculation of the poloidal asymmetry factors

$\tilde{\theta}_j$  which enter into the calculation of the frequencies  $\nu_{dj}$  for the radial transport of toroidal angular momentum.

Making expansions of the type indicated by Eq.(11) for the density and velocities for each species in Eq. (16) and taking the flux surface average with weighting functions 1,  $\sin\theta$  and  $\cos\theta$  results in a coupled set of moments equations (three times the number of ion species) that must be solved for the  $V_{\theta j}^0$  and  $\tilde{n}_j^{s,c}$  for all the plasma ion species. If the first term on the right in Eq. (17) is neglected, these equations can be solved locally on each radial flux surface. The justification for this neglect is the plausible assumption  $V_{rj} \ll V_{\theta j} < V_{\phi j}$ , which would also justify neglect of the second term on the right in Eq. (17). The resulting equations are

$$\begin{aligned} & \hat{V}_{\theta j} \left[ -q \hat{V}_{\phi j} \varepsilon \left( \tilde{n}_j^s + \tilde{\Phi}^s \right) - q^2 f_j f_p \left( 1 + \tilde{\Phi}^c + \frac{2}{3} \tilde{n}_j^c \right) + f_p \sum_{k \neq j} v_{jk}^* (1 + \Delta_{fric,j}) \right] \\ & - \sum_{k \neq j} \hat{V}_{\theta k} \left[ f_p v_{jk}^* \sqrt{\frac{m_j}{m_k}} \right] (1 + \Delta_{fric,k}) = \\ & - \hat{V}_{rj} - q \varepsilon \frac{1}{4} \tilde{n}_j^s - q \varepsilon \hat{\Phi}_j \left[ \frac{1}{4} (\tilde{\Phi}^s + \Delta_{\Phi j}) \right] - q^2 f_j f_p (\hat{V}_{\phi j} + \hat{P}_j) \tilde{\Phi}^c \\ & - q \varepsilon \hat{V}_{\phi j} \left[ (\hat{V}_{\phi j} + \hat{P}_j) \tilde{\Phi}^s + \frac{1}{2} \hat{V}_{\phi j} \tilde{n}_j^s \right] \end{aligned} \quad (19)$$

where  $\Delta_{fric,j} \equiv -\frac{1}{2} \varepsilon^2 \left( 1 + n_j^c + (n_j^c)^2 + (n_j^s)^2 \right)$ ,  $\Delta_{\Phi j} \equiv \tilde{n}_j^c \tilde{\Phi}^s - \tilde{n}_j^s \tilde{\Phi}^c$ , and

$$\begin{aligned} & \tilde{n}_j^s \left[ \frac{1}{3} \frac{q^2}{\varepsilon} f_j f_p \hat{V}_{\theta j} + \frac{1}{2} \varepsilon \hat{V}_{rj} - \frac{1}{2} \varepsilon f_p \sum_{k \neq j} v_{jk}^* \hat{V}_{\theta k} \sqrt{\frac{m_j}{m_k}} \right] \\ & + \tilde{n}_j^c \left[ \frac{1}{2} q f_p^2 \hat{V}_{\theta j}^2 - \frac{1}{4} q \right] = -\frac{1}{2} \varepsilon f_p \sum_{k \neq j} v_{jk}^* \hat{V}_{\theta j} \tilde{n}_k^s - \frac{1}{2} q \hat{V}_{\phi j}^2 (1 + \Delta_{inert1,j}) \\ & + \frac{1}{4} q \hat{\Phi}_j \tilde{\Phi}^c - \frac{q^2}{\varepsilon} f_j f_p \frac{1}{2} (\hat{V}_{\theta j} - \hat{V}_{\phi j} - \hat{P}_j) \tilde{\Phi}^s - \frac{1}{2} q f_p^2 \hat{V}_{\theta j}^2 \end{aligned} \quad (20)$$

where  $\Delta_{inert1,j} = \frac{1}{2} \varepsilon^2 \left( \frac{1}{2} (\tilde{V}_{\phi j}^c)^2 + \tilde{n}_j^c \tilde{V}_{\phi j}^c + 3 \tilde{n}_j^s \tilde{V}_{\phi j}^s + \frac{3}{2} (\tilde{V}_{\phi j}^s)^2 \right)$ , and

$$\begin{aligned} & \tilde{n}_j^c \left[ \frac{1}{3} \frac{q^2}{\varepsilon} f_j f_p \hat{V}_{\theta j} + \frac{1}{2} \varepsilon \hat{V}_{rj} - \frac{1}{2} \varepsilon f_p \sum_{k \neq j} v_{jk}^* \hat{V}_{\theta k} \sqrt{\frac{m_j}{m_k}} \right] \\ & + \tilde{n}_j^s \left[ -\frac{1}{2} q f_p \hat{V}_{\theta j}^2 + \frac{1}{4} q \right] = -\frac{1}{2} \varepsilon f_p \sum_{k \neq j} \tilde{n}_k^c \left[ v_{jk}^* \hat{V}_{\theta j} \right] \\ & - \frac{1}{4} q \hat{\Phi}_j \tilde{\Phi}^s - \frac{q^2}{\varepsilon} f_j f_p \left[ \frac{1}{2} \left\{ (1 + \tilde{\Phi}^c) \hat{V}_{\theta j} - (\hat{V}_{\phi j} + \hat{P}_j) \tilde{\Phi}^c \right\} \right] \\ & - q \hat{V}_{\phi j}^2 \Delta_{inert2,j} \end{aligned} \quad (21)$$

where  $\Delta_{\text{inert}2,j} = \frac{1}{4} \varepsilon \left\{ \tilde{V}_{\phi j}^s \tilde{V}_{\phi j}^c + \tilde{n}_j^c \tilde{V}_{\phi j}^s + \tilde{n}_j^s \tilde{V}_{\phi j}^c \right\}$ . The  $\tilde{V}_{\phi j}^{s,c}$  are derived from the radial component of the momentum balance equation and defined in Eq. (13). We note that  $V_{\theta j}^c / V_{\theta j}^0 = -\varepsilon \left( 1 + \tilde{n}_j^c \right)$  and  $V_{\theta j}^s / V_{\theta j}^0 = -\varepsilon \left( \tilde{n}_j^s \right)$  have been derived from the particle continuity equations and used in the above development. We have introduced the additional notation

$$\hat{V}_{rj} \equiv \frac{\bar{V}_{rj}}{\left( \frac{m_j \nu_{thj}}{e_j B_\theta^0} \right) \left| f_p \right| \left( \frac{\nu_{thj}}{qR} \right)}, \quad v_{jk}^* \equiv \frac{\bar{v}_{jk}}{\frac{\nu_{thj}}{qR}}, \quad \hat{\Phi}_j \equiv \frac{e_j \bar{\Phi}}{T_j}, \quad (22)$$

The  $\Delta_{xx}$  are higher order terms that were not consistently retained in earlier versions (e.g. Ref. 24) of these equations.

#### E. Radial electric field and toroidal rotation velocities

For each ion species, the momentum balance equation minus  $m_j \mathbf{V}_j$  times the particle balance equation is

$$n_j m_j (\mathbf{V}_j \cdot \nabla) \mathbf{V}_j + \nabla p_j + \nabla \cdot \Pi_j = -n_j e_j \nabla \Phi + n_j e_j \mathbf{V}_j \times \mathbf{B} + \mathbf{F}_j + \mathbf{M}_j \quad (23)$$

where  $\mathbf{F}_j = -n_j m_j \nu_{jk} (\mathbf{V}_j - \mathbf{V}_k)$  is the interspecies collisional friction and  $\mathbf{M}_j$  is the net external momentum input (e.g. neutral beam input less any charge-exchange and asymmetric ionization source losses). The lowest-order radial component of the flux surface average of Eq. (23) for each species ‘j’ is

$$\left( \bar{E}_r / B_\theta^0 \right) = V_{\phi j}^0 - \left( \bar{B}_\phi^0 / B_\theta^0 \right) V_{\theta j}^0 + \bar{P}_j \quad (24)$$

where the overbar or zero superscript indicates the average value over the flux surface.

The flux surface average of the toroidal component of Eq. (23) for each species ‘j’ can be written

$$n_j^0 m_j \bar{\nu}_{jk} \left( (1 + \beta_j) V_{\phi j}^0 - V_{\phi k}^0 \right) = n_j^0 e_j E_\phi^A + e_j B_\theta^0 \Gamma_j + \bar{M}_{\phi j} \equiv n_j^0 m_j \bar{\nu}_{jk} y_j, \quad (25)$$

where radial transport of toroidal momentum is represented by the parameter

$$\beta_j \equiv \frac{\bar{\nu}_{dj}^*}{\nu_{jk}} \quad (26)$$

The ion-electron friction term has been neglected. A sum over other species ‘k’ is implied and the collisional momentum conservation requirement  $n_j^0 m_j \bar{\nu}_{jk} = n_k^0 m_k \bar{\nu}_{kj}$  has been used in deriving Eq. (25).

We note that most neoclassical derivations (e.g. Refs. 14 and 27) obtain the result that the radial electric field is proportional to the radial ion temperature gradient (which is proportional to  $V_\theta$  in those derivations). The above equations can be rearranged to compare with these earlier derivations. Using the radial momentum balance Eqs. (24) in the toroidal momentum balance Eqs.(25) to eliminate the  $V_{\phi j}^0$  and summing over species yields another expression for the radial electrostatic field

$$\frac{\bar{E}_r}{B_\theta^0} = \left[ \frac{\{ \hat{M}_{\phi I} + \hat{M}_{\phi i} \} + \beta_i \{ \bar{P}_i - \left( \bar{B}_\phi^0 / B_\theta^0 \right) (V_{\theta i}^0) \} + \beta_i \{ \bar{P}_i - \left( \bar{B}_\phi^0 / B_\theta^0 \right) (V_{\theta i}^0) \}}{\beta_i \{ \bar{P}_i - \left( \bar{B}_\phi^0 / B_\theta^0 \right) (V_{\theta i}^0) \}} \right] \div [\beta_i + \beta_i] \quad (27)$$

that displays the dependence on momentum input, pressure and poloidal rotation velocity. Since earlier derivations usually do not take into account the presence of external angular momentum input they naturally do not obtain the terms in the first  $\{ \}$  brackets.

### III. Comparison with DIII-D rotation measurements

The main purposes of this paper are to compare theoretical and experimental toroidal rotation velocity radial profiles and to draw some conclusions therefrom about how much of the radial transport of toroidal angular momentum in DIII-D tokamak plasmas is accounted for by neoclassical viscosity (as represented in the previous section) and how much must be attributed to other processes. A diverse set of discharges including L- and H-modes, with and without internal transport barriers and with and without neon injection, were analyzed for this purpose, as indicated in Table 1. The measured density and temperature profiles for these shots are given in Figs. 1 and 2. A secondary purpose was to extend the investigation of the effect of neon impurity injection on momentum transport, for which purpose three “sister shot” pairs with and without neon injection were included.

#### A. Description of discharges

##### L-mode “sister shots” 98777 and 98775 @ 1.6s<sup>40</sup>

These were L-mode shots that were operated identically in every respect except for the injection of 2.8% neon impurity concentration in shot 98775. Long wavelength turbulence as well as heat and momentum transport were measured to be reduced with neon-injection. The intrinsic carbon concentrations were 1.1% in #98777 and 0.5% in the neon-injected #98775. (The cited carbon and neon concentrations correspond to the measured values at  $\rho = \frac{1}{2}$  in this and other shots.)

##### L-mode ITB “sister shots” 102942 and 102940 @ 1.4s<sup>41</sup>

These were co-injected shots with an internal transport barrier (ITB) and a typical L-mode edge. The measured temperature and toroidal velocity profiles were quite peaked throughout the discharge. The density profiles were flat early in the discharge, but sharp density and electron temperature gradients developed later in the discharge following an increase in beam power, indicating the formation of an internal transport barrier (ITB). The shots were operated identically except for neon injection in shot 102940, which produced broader profiles and higher temperatures (i.e. better energy confinement), larger toroidal rotation velocities, and reduced turbulence levels in the core as compared to the sister shot 102942 without neon injection.

##### H-mode shot 99411 @ 1.8s<sup>42</sup>

This was a high-performance ( $H_{89P} = 2.8$ ,  $\beta_N H_{89P} = 10$ ) ELMing H-mode shot with a typical H-mode edge pedestal and a relatively large (5%) carbon intrinsic impurity concentration.

##### H-mode QDB “sister shots” 106919 @ 3.5s & 106972 @ 2.9s<sup>43</sup>

These were counter-injected, quiescent double barrier (QDB) shots with both an internal transport barrier and an edge transport barrier typical of H-mode discharges. The edge was quiescent [i.e. free of edge localized modes (ELMs)], but a saturated coherent MHD edge harmonic oscillation (EHO) was present at the separatrix. The turbulence was reduced but not entirely suppressed in the internal transport barrier. These discharges had relatively low plasma densities and large and accumulating concentrations of Ni and Cu ( $Z_{\text{eff}}$  at  $\rho = \frac{1}{2}$  was 4.1 @ 2010 ms and 5.4 @ 3510 ms, more than half of which was due to Ni and Cu). The carbon concentration was 3.7% in 106919 and 3.1% in 106972. The shots were operated identically except for neon injection in shot 106972.

#### B. “2-Species” calculation model

The calculation model consisted of Eqs. (19)-(21) for the poloidal rotation velocities and density asymmetries for the main ion (deuterium) and an effective impurity ion species, the two Eqs. (25) for the

toroidal rotation velocities for the main and effective impurity ion species, and the radial component Eq. (24) of the momentum balance for the effective impurity species. We solved the two Eqs. (25) for the deuterium ion rotation velocity

$$V_{\phi i}^0 = \frac{(1 + \beta_i)y_i + y_I}{(1 + \beta_i)(1 + \beta_I) - 1} \quad (28)$$

and then solved the deuterium ion Eq. (25) for the effective impurity rotation velocity

$$V_{\phi I} = (1 + \beta_i)V_{\phi i} - y_i \quad (29)$$

The radial electric field was then calculated from the radial momentum balance Eq. (24) for the effective impurity species, for consistency with the way the experimental radial electric field was calculated.

### C. Evaluation of input parameters

We took the electron density distribution, the ion and electron temperature distributions, the toroidal electric field, and the radial gradient scale lengths  $L_n^{-1}$ ,  $L_T^{-1}$  and  $L_v^{-1}$  from experiment. The radial distribution of neutral beam angular momentum deposition was calculated with the code NBEAMS<sup>44</sup>. The value of the electrostatic potential  $\Phi$  used in Eq. (19) to calculate the poloidal rotation velocity was taken from TRANSP calculations<sup>45</sup> based on an integration inward of the experimental radial electric field. The calculation was only made out to  $\rho = 0.9$  or  $0.95$  because atomic physics effects (not taken into account in the calculation) become an important momentum transfer mechanism closer to the separatrix.

A brief discussion of the use of the experimental radial gradient scale lengths  $L_n^{-1}$ ,  $L_T^{-1}$  and  $L_v^{-1}$  is in order at this point so that their effect on the calculation is clear. Our intent in this paper is to test the validity of Eq. (9) and its approximate representation Eq. (12), the expression for the gyroviscous torque which determines the rate of radial transport of toroidal angular momentum. The radial derivatives enter Eq. (12) via the factor  $G_j$ . We are not able at this time to accurately calculate the radial distributions of  $n$ ,  $T$  and  $V_\phi$  needed to accurately evaluate  $G_j$ , yet the accurate evaluation the  $G_j$  is a necessary (but not sufficient) condition for Eq. (12) to predict the correct momentum transport rate. So we use the experimental gradient scale lengths to insure that an accurate evaluation of  $G_j$  is used to test Eq. (12). To put it another way, to calculate the correct momentum transport rate it is not only necessary to use the correct  $G_j$ , but also to use it in the correct equation, to use the correct viscosity coefficient  $\eta = \eta_4 = nmT/Z_eB$  and poloidal asymmetry factor given by Eq. (11). E.g., if Eq. (10) for the perpendicular viscosity with  $\eta = \eta_2 = (nmT/Z_eB)/\Omega\tau$  was used instead of Eq. (9) to represent the radial transport of toroidal angular momentum, and if the same experimental radial gradient scale lengths were used to evaluate the expression equivalent to Eq. (12) derived from Eq. (10), the resulting magnitude of the toroidal rotation velocity would be several orders of magnitude larger because  $\Omega\tau \approx 10^3 - 10^4$ .

In a similar vein, we have elected to use the value of the electrostatic potential  $\Phi$  calculated in TRANSP by integrating the experimental radial electric field, rather than integrating the calculated radial electric field, because there is some ambiguity about the boundary conditions that should be used.

### D. Modeling of multiple impurity species

Since the present model is limited (by implementation, not inherently) to two ion species—“main ion” and “impurity”—it was necessary to model the six charge states of carbon as a single impurity species with effective charge and mass determined by density weighting. This should be a good approximation over most of the plasma where carbon is fully ionized, but not in the edge. When neon was present it was similarly treated, and then the effective neon and carbon species were combined into a single effective impurity species. In the counter-injected shots with significant Cu and Ni impurities a similar treatment was used to obtain a single high-Z (Ni+Cu) impurity that was then combined with carbon and neon to obtain a single effective impurity species. (This single impurity species model was

found to cause the calculation to become inconsistent for the shots with multiple high-Z impurity charge states, as will be discussed.) Clearly, the association of the calculated “impurity” rotation velocity with the measured carbon VI rotation velocity in the presence of neon and high-Z impurities is valid only to the extent that the various impurity ion species are entrained by interspecies collisions to have a common rotation velocity, which is thus an implicit assumption of this work. We plan to introduce a multiple impurity species model in future work. Note that the less collisional main (deuterium) ions are not assumed to have the same rotation velocities as the more collisional impurity ions.

#### E. Numerical solution

Taking Eqs. (19)-(21) (for each species) and Eqs. (28)-(29) as our model for a two-species plasma of ions and impurities, we have an 8-dimensional system of coupled nonlinear equations. We solved this set of nonlinear equations for the rotation velocities and poloidal density coefficients  $(V_{\phi i}, V_{\phi I}, V_{\theta i}, V_{\theta I}, n_i^c, n_I^c, n_i^s, n_I^s)$  numerically. A scalar residual merit function over the unknown parameters was defined as the magnitude of the vector of the normalized residuals, and was evaluated at each radial location. The residual for each equation was the value of the equation, when all terms were collected to one side, using the parameter values as the trial solution, and was normalized by the root-mean-square of the individual terms. The merit function was minimized using a simplex search algorithm<sup>46,47</sup>. Solutions were generally accepted as converged only if the scalar residual was on the order of  $10^{-11}$  or less, though some few points were accepted with somewhat larger values if they were seen to be a continuation along the radius of accepted solutions at other radii.

#### F. Comparison of calculated and measured toroidal rotation frequencies

The measured and calculated toroidal rotation frequencies  $\Omega_\phi \equiv V_\phi / R$  are compared in Figs. 3a-9a. The corresponding poloidal rotation velocities are shown in Figs. 3b-9b, the density asymmetry coefficients of Eq. (11) are shown in Figs. 3c-9c, and the radial electric fields calculated from Eq. (24) using the rotation velocities calculated for the effective impurity species are compared with the  $E_r^{exp}$  calculated from the same equation using the measured rotation velocities for carbon VI in Figs. 3d-9d. It was not possible to find “accepted” solutions (as discussed above) to the coupled set of nonlinear equations described above at each radial location for all shots. This does not mean necessarily that such solution do not exist, only that they were not found.

For the L-mode shots 98775 and 98777 shown in Figs. 3 and 4, the toroidal rotation frequency is over-predicted by a factor of 1.5-3 in the center region, reducing with radius to rather good agreement in the outer region. The normalized density asymmetry coefficients satisfied  $-1 \leq n^{c,s} \leq 1$ , indicating that the effective impurity species model and low-order Fourier expansion model was adequate, except for  $\rho > 0.8$  in shot 98775 with neon. This difficulty probably arises from the inadequacy of a single effective impurity species representation of 10 neon charge states in the edge of shot 98775, not from the inadequacy of the low order Fourier expansion per se. The predicted radial electric field, calculated with Eq. (24) using the measured carbon VI pressure gradient and the calculated toroidal and poloidal rotation velocities of the effective impurity species, compares well with the “experimental” radial electric field, also calculated from Eq. (24) using the measured carbon VI pressure gradient but the measured toroidal and poloidal rotation velocities of carbon VI, for shot 98777 without neon, but the agreement is not so good for shot 98775 with neon. This disagreement is related to the larger poloidal rotation velocity calculated for the effective impurity species in shot 98775 with neon. The observed larger toroidal rotation in shot 98775 with neon than in shot 98777 is not apparent in the calculated results.

For the L-mode ITB shots 102940 and 102942 shown in Figs. 5 and 6, the predicted toroidal rotation frequencies for the effective impurity species agree quite well with the measured values for carbon VI ( $< 50\%$  over-prediction), for those radii at which it was possible to obtain a solution of the nonlinear set of equations. Again, the density asymmetry coefficients satisfied  $-1 \leq n^{c,s} \leq 1$  except for the effective impurity species coefficients in the outer regions of shot 102940 with neon. The calculated radial electric field agreed much better with the measured value for the shot 102942 without neon than for the shot 102940 with neon, and this latter can be attributed to the larger poloidal rotation velocity calculated for the effective impurity species in the shot 10940 with neon. Because of the difficulty in

getting solutions in the inner regions it is not possible to comment on the dependence on neon of the predicted toroidal rotation velocities.

For the H-mode shot 99411 shown in Fig. 7, the predicted toroidal rotation frequencies are a factor of  $< 3$  larger than the measured values. The normalized density asymmetry coefficients satisfied  $-1 \leq n^{c,s} \leq 1$ . The measured and calculated radial electric fields do not agree in the outer region where a large negative peak in the calculated carbon poloidal rotation causes a negative peak in the calculated  $E_{rad}^l$ . This peaking in  $E_{rad}^l$  and  $V_{\theta l}$  is correlated with a peaking in  $n_I^{c,s}$ .

Agreement between predicted and measured toroidal rotation frequencies is poorest for the counter-injected QDB shots 106919 and 106972. These shots had significant Cu and Ni impurities, and the normalized density asymmetry coefficients for the effective impurity species were  $n^{c,s} \geq 1$  over much of the radius, probably reflecting the inadequacy of treating such a large number of impurity charge states as a single effective species. The disparity in the calculated and measured toroidal rotation velocities is reflected in the disparity between calculated and measured radial electric fields.

So, what can be inferred about the ability of neoclassical gyroviscosity to account for the experimentally inferred radial transport rate of angular momentum? Considering only the shots with only carbon impurities (98777, 102942, 99411), for which the single effective impurity species model would be expected to work the best, we observe that neoclassical gyroviscosity leads to an over-prediction of the toroidal rotation by less than a factor of 2-3 at the most, from which we conclude that neoclassical gyroviscosity can account for one-third to one-half of the experimentally inferred radial transport of toroidal angular momentum in these shots. Considering next the shots with carbon and neon impurities (98775, 102940), there is evidence from the density asymmetries that the single effective impurity species model breaks down for  $\rho > 0.8$ , where multiple neon charge states are present. The toroidal rotation in these shots is generally over-predicted by only about 50% or less for  $\rho < 0.8$ , where the single effective impurity species model might be expected to work better, from which we conclude that neoclassical gyroviscosity can account for perhaps 2/3 of the experimentally inferred transport rate of angular momentum in these shots. Finally, consider the QDB shots (106919, 106972), in which multiple charge states of Ni and Cu, together with fully stripped carbon and neon are present throughout the plasma. The poloidal density coefficients indicate that the single effective impurity species model is breaking down over most of the plasma, so these shots do not provide a meaningful test of the ability of neoclassical gyroviscosity to account for the experimentally inferred transport rate of angular momentum. In summary, we conclude that about 1/3 to 2/3 of the experimentally inferred radial transport rate of angular momentum can be accounted for by neoclassical gyroviscosity.

Angular momentum outward convection was not modeled, and including this process would reduce the central peaking in the predicted toroidal rotation frequencies, bringing them into better agreement with measured values, and would account for some additional fraction of the experimentally inferred radial transport rate of toroidal angular momentum.

In addition to the shortcomings of the single effective impurity species representation of multiple impurity charge states discussed above, there are other modeling approximations and assumptions that could affect the above comparison. First, the magnetic flux surface approximation  $B = B^0 / (1 + \varepsilon \cos \theta)$  neglects Shafranov shift, elongation and geometry-driven up-down asymmetry effects due to a single-null divertor. It is expected that taking into account up-down asymmetry in the magnetic field would increase the up-down asymmetry in the density and rotation velocities, which in turn would increase the asymmetry factor of Eq. (13) and hence the gyroviscous momentum transport frequency  $\nu_d$  defined in Eq. (12). This would presumably result in an increase in the fraction of the experimentally inferred momentum transport rate that is accounted for by neoclassical gyroviscosity. Second, the Braginskii large rotation ordering  $V_\phi / v_{th} \approx 1$  was used in the gyroviscosity representation. The parameter  $V_\phi / v_{th}$  varied over the range 0.1-0.4 for deuterium in these shots (with larger values for the impurities), so that the Braginskii ordering  $V_\phi / v_{th} \approx 1$  used in this paper seems more appropriate than the Mikhailovski-Tsypin ordering  $V_\phi / v_{th} \ll 1$ , but we can not rule out that the gyroviscous stress tensor should be modified to include heat flux terms<sup>27</sup> that are needed in the ordering  $V_\phi \ll v_{th}$ .



#### IV. Summary and Conclusions

We have tested the neoclassical viscosity formalism for the radial transport of angular momentum by comparing predicted and measured radial profiles of toroidal rotation velocity in several DIII-D discharges spanning L-mode, L-mode with ITB, H-mode and H-mode with QDB confinement regimes with and without neon injection. The velocity calculations were based on using the neoclassical toroidal gyroviscous torque in equations for the toroidal velocities derived from toroidal momentum balance, and on using the neoclassical parallel viscosity in equations for the poloidal rotation velocities and poloidal asymmetries in density and rotation velocities derived from poloidal momentum balance. Measured background temperatures and densities were used, and radial gradients of temperature, density and toroidal velocity were evaluated using radial gradient scale lengths determined from experiment, but otherwise the calculations were “first-principles”.

The calculated toroidal rotation over-predicted the measured values in all cases, more in the center of the plasma (by factors of 1.5 to 3) than in the outer regions. We conclude from this that neoclassical viscosity can account for a significant part, but not all, of the radial transport of angular momentum observed in these shots. Several approximations in the calculation model—neglect of convection, one effective impurity species representation,  $B_\theta = B_\theta^0 / (1 + \varepsilon \cos \theta)$  representation of flux surface geometry—prevent us from unambiguously attributing this over-prediction entirely to the presence of other angular momentum transport (e.g. turbulence) or reverse torque input mechanisms.

We intend to improve the calculation model to remove these limitations on its implementation. In addition, we plan to implement a radial differential equation solution for the toroidal velocity profile, thereby removing the necessity of representing radial gradients by gradient scale lengths and taking convection and inertial effects into account automatically.

#### References

1. S. Suckewer, H. P. Eubank, R. J. Goldston, *et al.*, Phys. Rev. Lett., 43, 207 (1979).
2. R. C. Isler, L. E. Murray, E. C. Crume, *et al.*, Nucl. Fusion, 23, 1017 (1983).
3. R. J. Groebner, W. Pfeiffer, F. P. Blau, *et al.*, Nucl. Fusion, 26, 543 (1986).
4. S. D. Scott, V. Arunasalam, C. W. Barnes, *et al.*, Phys. Fluids B, 2, 1300 (1990).
5. H. P. L. deEsch, D. Stork and H. Weisen, Proc. Conf. Control. Fusion & Plasma Heating (Amsterdam), vol 14B, Part I (Geneva: Euro. Phys. Soc.) p90 (1990).
6. F. Wagner, F. Ryter, A. R. Field, *et al.*, Proc. 13<sup>th</sup> Int. Conf. Plasma Phys. Control. Fusion Res., Washington (Vienna: Int. Atomic Energy Agency) p277 (1991).
7. K-D. Zastrow, *et al.*, Proc. 22<sup>nd</sup> Euro. Conf. Control. Fusion Plasma Phys. (Bournemouth) vol 19C, part II (Geneva: Euro. Phys. Soc.) p453 (1995).
8. J. S. deGrassie, *et al.*, Proc. 26<sup>th</sup> Euro. Conf. Control. Fusion Plasma Phys. (Maastricht) vol 23J (Geneva: Euro. Phys. Soc.) p1189 (1999).
9. K-D. Zastrow, W. G. F. Core, L-G. Erickson, *et al.*, Nucl. Fusion, 38, 257 (1998).
10. J. S. deGrassie, D. R. Baker, K. H. Burrell, *et al.*, Nucl. Fusion, 43, 142 (2003).
11. A. N. Kaufmann, Phys. Fluids, 3, 610 (1960).
12. S. I. Braginskii, Rev. Plasma Phys., 1, 205 (1965).
13. M. N. Rosenbluth, P. H. Rutherford, J. B. Taylor, *et al.*, Proc. Conf. Plasma Phys. Control. Fusion (Vienna: Int. Atomic Energy Agency) vol. 1, p495 (1971).
14. R. D. Hazeltine, Phys. Fluids, 17, 961 (1974).
15. K. T. Tsang and E. A. Frieman, Phys. Fluids, 19, 747 (1976).
16. A. B. Mikhailovskii and V. S. Tsypin, Sov. J. Plasma Phys., 10, 51 (1984).
17. W. M. Stacey and D. J. Sigmar, Phys. Fluids, 28, 2800 (1985).
18. F. L. Hinton and S. K. Wong, Phys. Fluids, 28, 3082 (1985).
19. J. W. Connor, S. C. Cowley, R. J. Hastie and L. R. Pan, Plasma Phys. Control. Fusion, 29, 919 (1987).
20. W. M. Stacey, Phys. Fluids B, 4, 3302 (1992).

21. R. D. Hazeltine and J. D. Meiss, "Plasma Confinement", Addison-Wesley, Reading MA (1994), pp 208, 220 and 226.
22. A. L. Rogister, Phys. Plasmas, 1, 619 (1994).
23. H. A. Claassen, H. Gerhauser and A. Rogister, Phys. Plasmas, 7, 3699 (2000).
24. W. M. Stacey, Phys. Plasmas, 8 158 (2001); 9, 3874 (2002); and 11, 3096 (2004).
25. P. J. Catto and A. N. Simakov, Phys. Plasmas, 11, 91 (2004); also, Contrib. Plasma Phys., 44, 83 (2004).
26. S. K. Wong and V. S. Chan, Phys. Plasmas, 11, 3432 (2004).
27. P. J. Catto and A. N. Simakov, Phys. Plasmas, 12, 012501 (2005).
28. D. Nishijima, A. Kallenbach, S. Gunter, et al., Plasma Phys. Control. Fusion, 47, 89 (2005).
29. A.G. Peeters and C. Angioni, Phys. Plasmas 12, 072515 (2005).
30. W. M. Stacey and D. R. Jackson, Phys. Fluids B, 5, 1828 (1993).
31. W. M. Stacey and M. Murakami, Phys. Plasmas, 8, 4450 (2001).
32. W. M. Stacey and J. Mandrekas, Phys. Plasmas, 9, 1622 (2002).
33. W. M. Stacey, A. W. Bailey, D. J. Sigmar and K. C. Shaing, Nucl. Fusion, 25, 463 (1985); W. M. Stacey and D. J. Sigmar, Phys. Fluids, 27, 2076 (1984) and 22, 2000 (1979); and Nucl. Fusion, 19, 1665, (1979).
34. K. H. Burrell, T. Ohkawa and S. K. Wong, Phys. Rev. Lett., 47, 511 (1981).
35. A. Bondeson and D. J. Ward, Phys. Rev. Lett., 72, 2709 (1994).
36. M. S. Chu, J. M. Greene, T. H. Jensen, R. W. Johnson, *et al.*, Phys. Plasmas, 2, 2236 (1995).
37. A. M. Garofalo, M. S. Chu, E. D. Fredrickson, *et al.*, Nucl. Fusion, 41, 1171 (2001).
38. E. Hameiri, Phys. Plasmas, 5, 3270 (1998).
39. K. H. Burrell, Phys. Plasmas, 4, 1499 (1997).
40. G. R. McKee, M. Murakami, J. Boedo, G. L. Jackson *et al.*, Phys. Plasmas, 7, 1870 (2000); Nucl. Fusion, 41, 317 (2001).
41. E. J. Doyle, C. M. Greenfield, M. E. Austin, *et al.*, Nucl. Fusion, 42, 333 (2002).
42. M. Murakami, H. St. John, T. A. Caspar, *et al.*, Nucl. Fusion, 40, 1257 (2000).
43. W. P. West, M. R. Wade, C. M. Greenfield, *et al.*, Phys. Plasmas, 9, 1970 (2002).
44. J. Mandrekas, "Physics models and user's guide for the neutral beam module of the SUPERCODE", Georgia Tech Fusion report GTFR-102 (1992), available from National Technical Information Service, NTIS-PB93-121887INZ.
45. R. J. Goldston, "Topics in confinement analysis of tokamaks with auxiliary heating," in *Basic Physical Processes of Toroidal Fusion Plasmas* (Commission of the European Comm. and Monotypia Frachi Citta di Castello, Italy, 1985), Vol 1, EUR 10418 EN.
46. W. H. Press, "Numerical Recipes", Cambridge Univ. Press, Cambridge (1992).
47. T. Rowan, "Functional Stability Analysis of Numerical Algorithms", PhD Thesis, Dept. Computer Sciences, University of Texas at Austin (1990). <ftp://www.netlib.org/opt/>

**Table 1 Parameters of DIII-D shots selected for rotation analysis**

Shot (time)	Conf. Mode	P <sub>nbi</sub> (MW)	$\bar{n}$ (10 <sup>19</sup> /m <sup>3</sup> )	$n_{carb}/n_e$	$\left(n_{neon}/n_e\right)$	$\left(n_{ni,cu}/n_e\right)$	$T_{i0}, T_{e0}$ (keV)	$\tau_E^{\text{exp}}$ (ms)
98777 1.6s	L	4.5 CO	3.4	0.011	-----	-----	3.5,2.5	66
98775 1.6s	L	4.5 CO	4.1	0.005	0.028	-----	6.3,3.3	90
99411 1.8s	H	9.2 CO	4.8	0.050	-----	-----	8.3,3.9	168
106919 3.5s	H-QDB	9.3 CTR	2.8	0.037	-----	0.005	14.2,4.2	140
106972 2.9s	H-QDB	8.7 CTR	2.9	0.031	0.003	0.003	15.2,4.2	117
102942 1.4s	L- ITB	7.0 CO	2.9	0.016	-----	-----	12.0,4.7	94
102940 1.4s	L- ITB	7.0 CO	3.2	0.006	0.013	-----	9.7,4.1	128

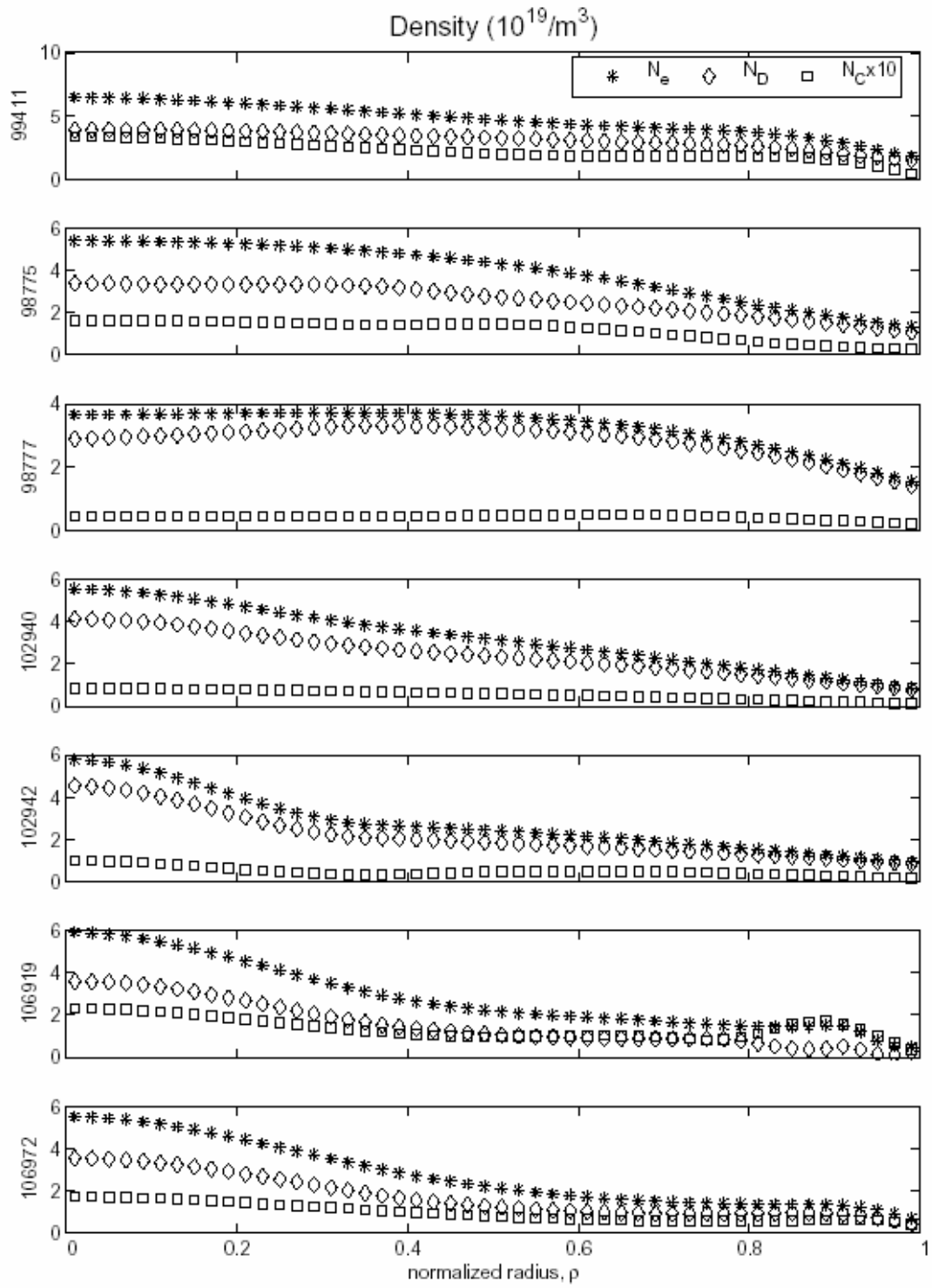


Fig. 1 Experimental electron, deuterium and carbon density distributions.

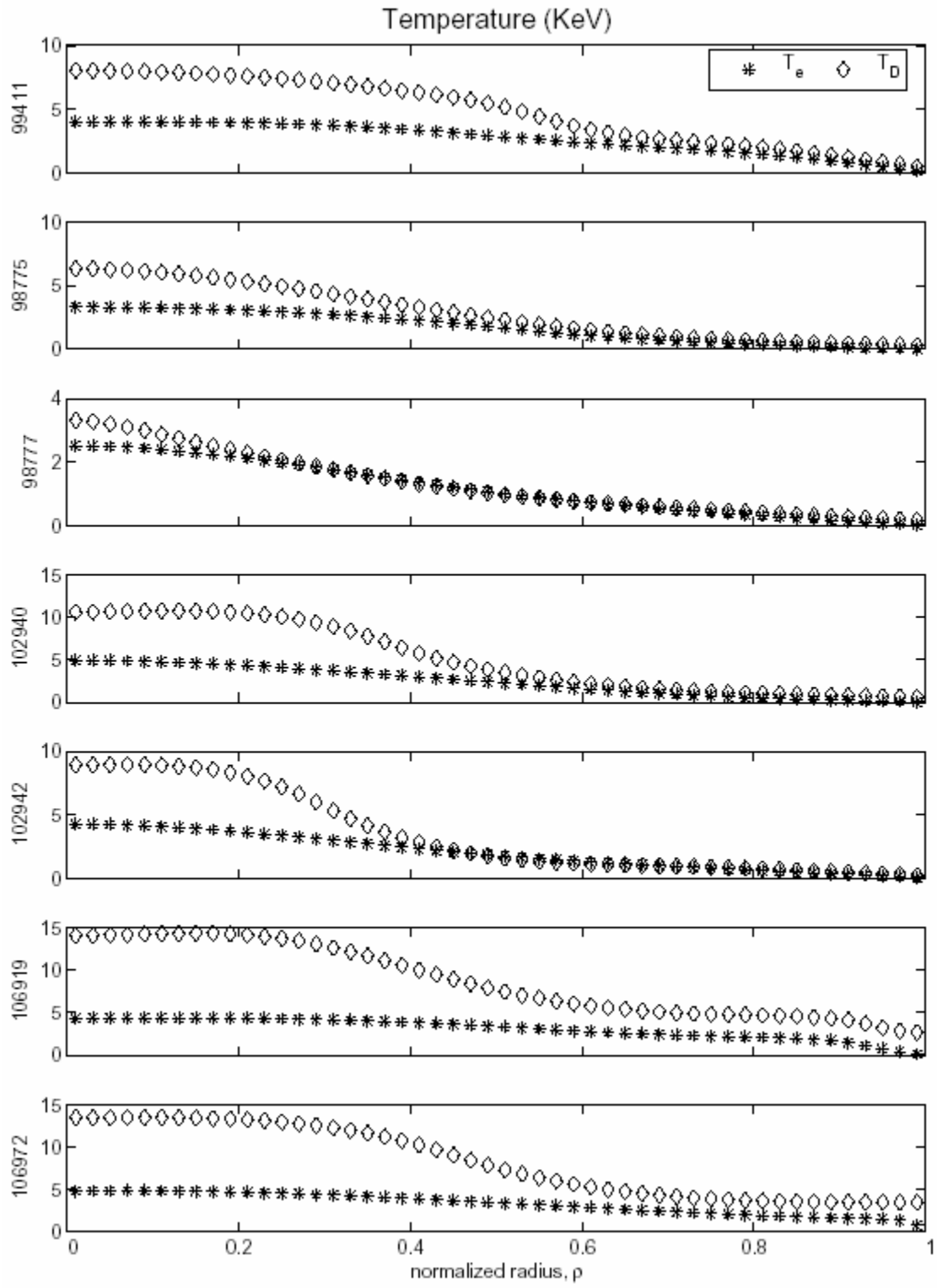


Fig. 2 Experimental deuterium ion and electron temperature distributions.

98777 (L-mode)

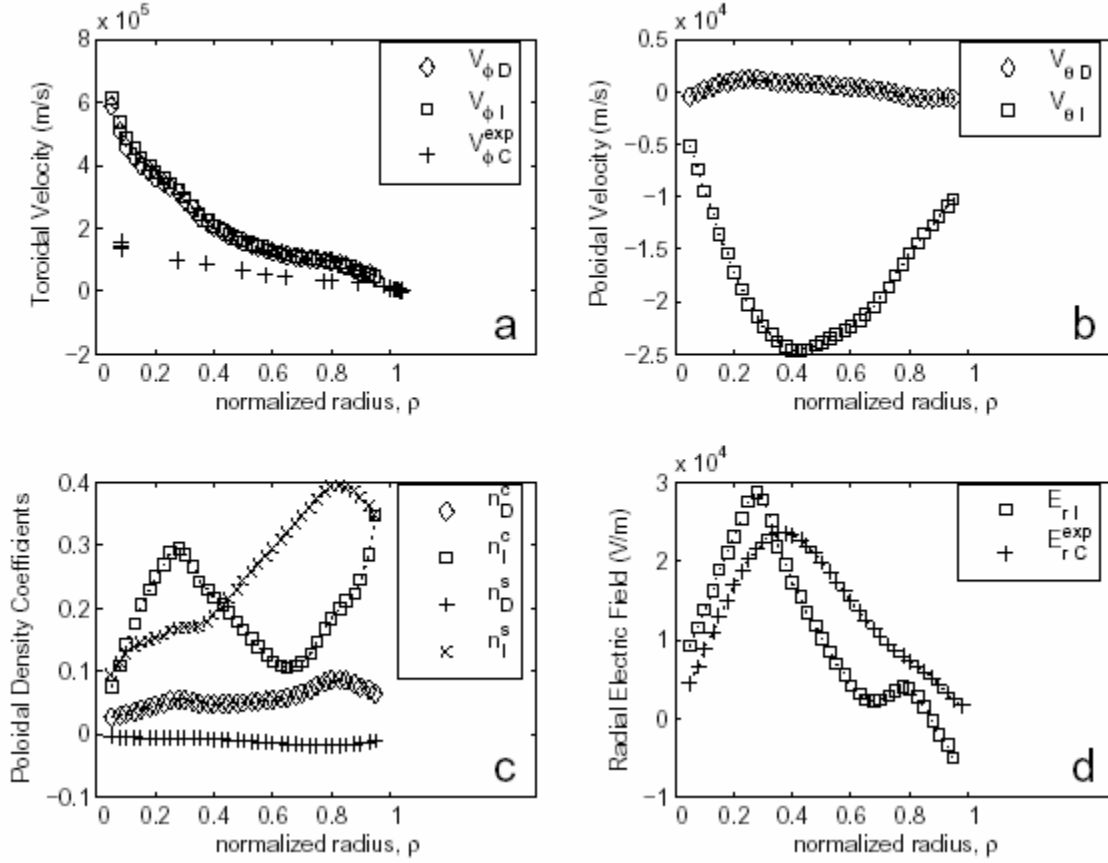


Fig. 3 Rotation calculations and experimental rotation velocities for CO-injected L-mode shot 98777: a) toroidal rotation frequencies  $\Omega_{\phi} \equiv V_{\phi} / R_0$  for deuterium and carbon; b) poloidal rotation velocities  $V_{\theta}$  for deuterium and carbon; c) normalized density asymmetry coefficients  $n^{s,c}$  for deuterium and carbon; d) radial electric field from carbon force balance using calculated and experiment  $V_{\theta,\phi}$  for carbon.

98775 (L-mode, w/Ne)

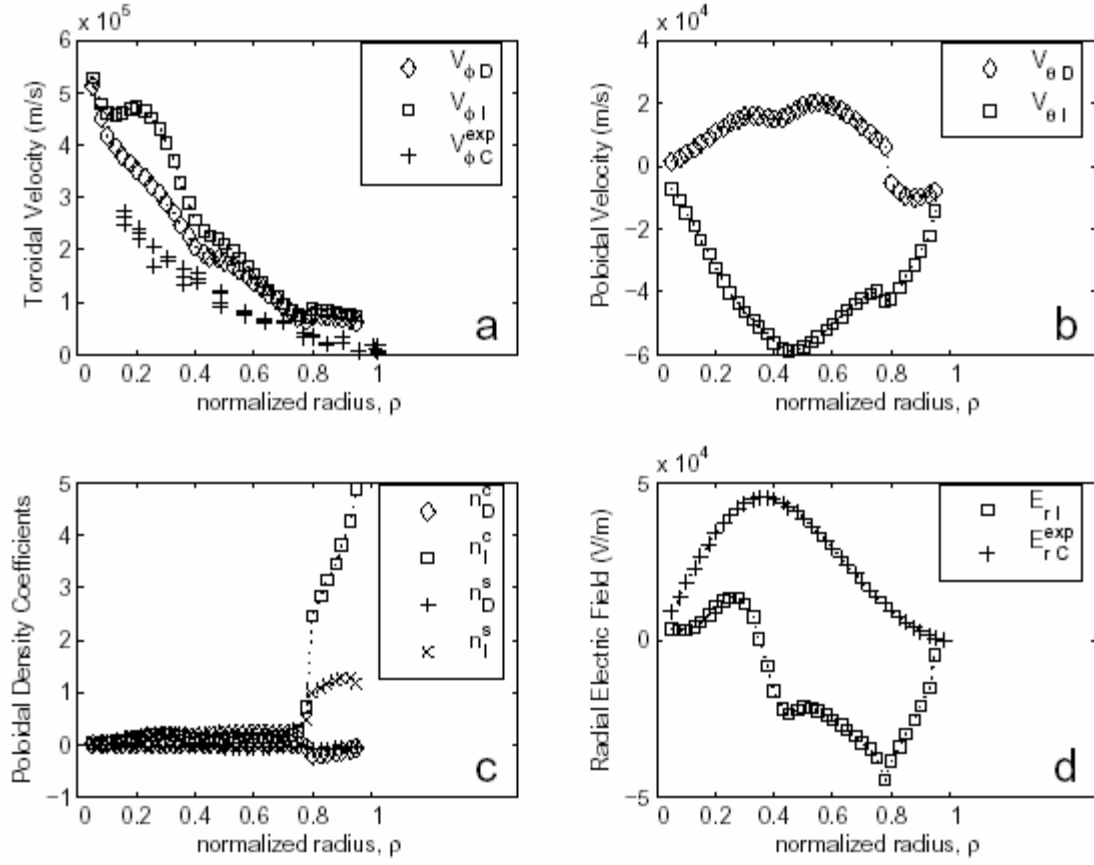


Fig. 4 Rotation calculations and experimental rotation velocities for CO-injected L-mode shot 98775 with neon: a) toroidal rotation frequencies  $\Omega_{\phi} \equiv V_{\phi} / R_0$  for deuterium and “impurity”; b) poloidal rotation velocities  $V_{\theta}$  for deuterium and “impurity”; c) normalized density asymmetry coefficients  $n^{s,c}$  for deuterium and “impurity”; d) radial electric field from carbon force balance using calculated  $V_{\theta,\phi}$  for “impurity” and experimental  $V_{\theta,\phi}$  for carbon.

102942 (L-mode, ITB)

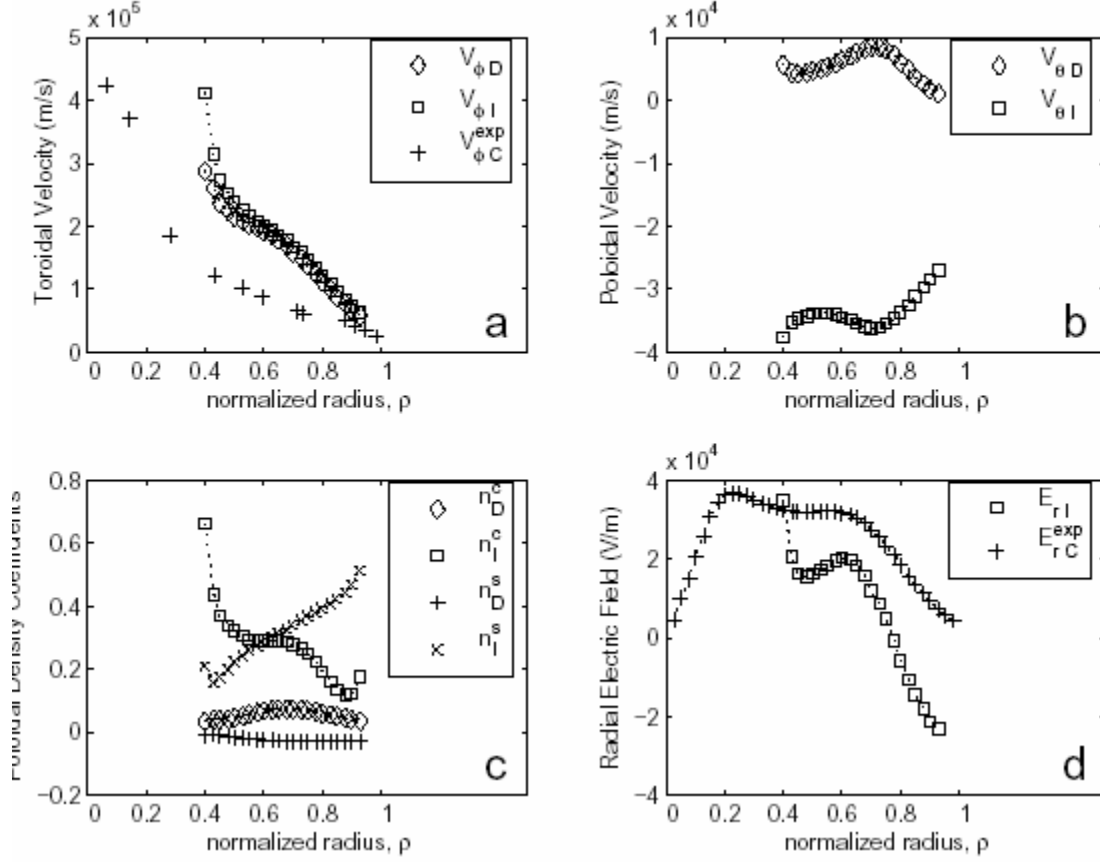


Fig. 5 Rotation calculations and experimental rotation velocities for CO-injected L-mode ITB shot 102942: a) toroidal rotation frequencies  $\Omega_{\phi} \equiv V_{\phi} / R_0$  for deuterium and “impurity”; b) poloidal rotation velocities  $V_{\theta}$  for deuterium and “impurity”; c) normalized density asymmetry coefficients  $n^{s,c}$  for deuterium and “impurity”; d) radial electric field from carbon force balance using calculated  $V_{\theta,\phi}$  for “impurity” and experimental  $V_{\theta,\phi}$  for carbon.



102940 (L-mode, ITB, w/Ne)

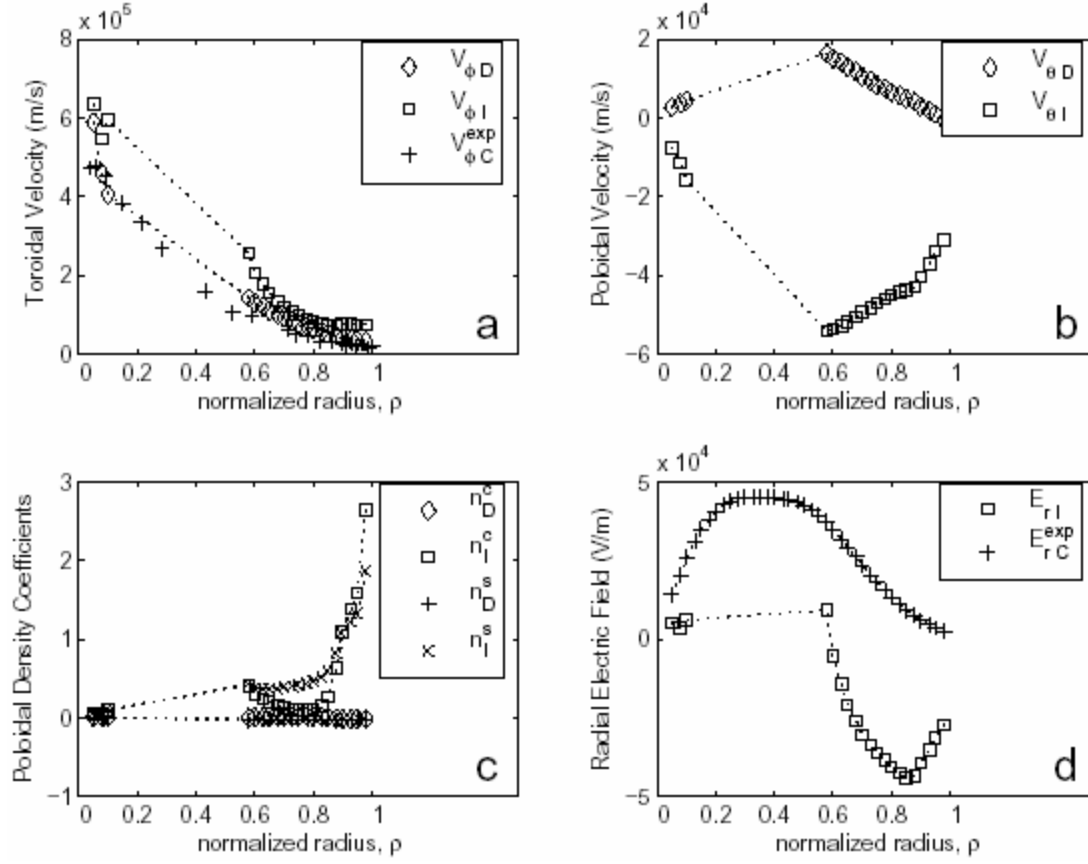


Fig. 6 Rotation calculations and experimental rotation velocities for CO-injected L-mode ITB shot 102940 with neon: a) toroidal rotation frequencies  $\Omega_{\phi} \equiv V_{\phi} / R_0$  for deuterium and “impurity”; b) poloidal rotation velocities  $V_{\theta}$  for deuterium and “impurity”; c) normalized density asymmetry coefficients  $n^{s,c}$  for deuterium and “impurity”; d) radial electric field from carbon force balance using calculated  $V_{\theta,\phi}$  for “impurity” and experimental  $V_{\theta,\phi}$  for carbon.

99411 (H-mode)

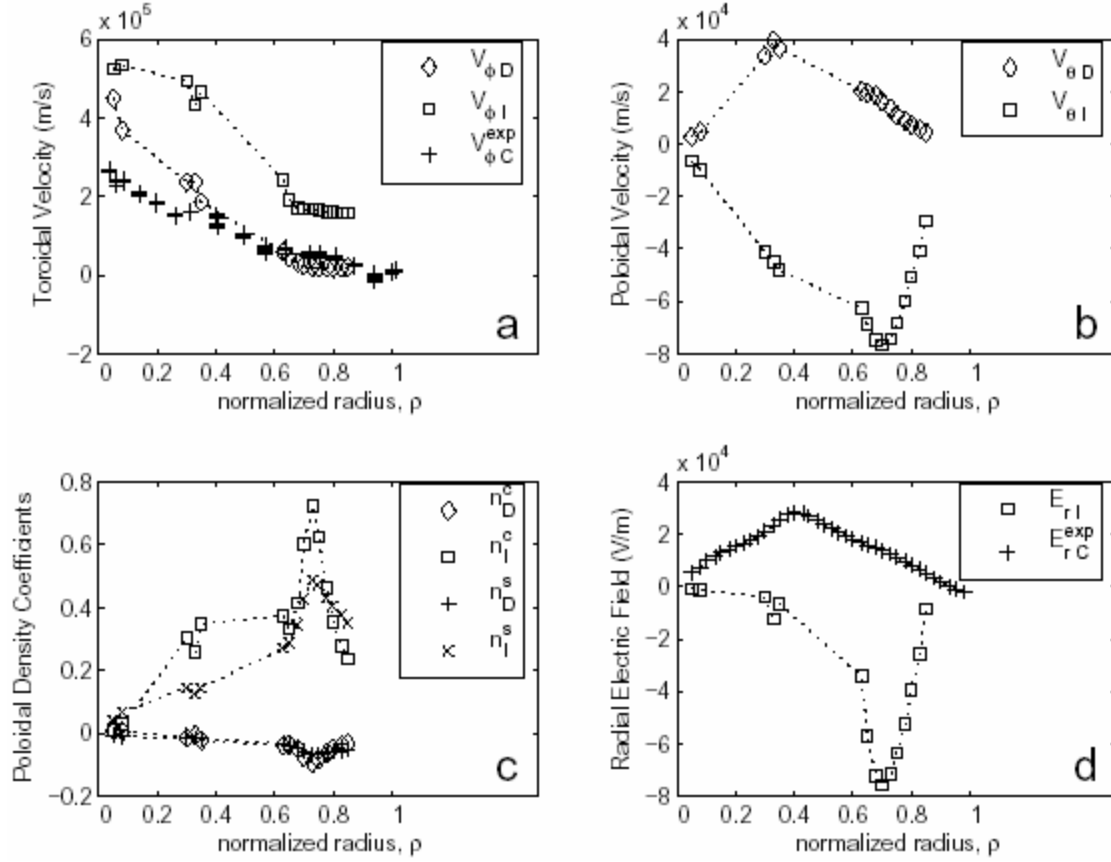


Fig. 7 Rotation calculations and experimental rotation velocities for CO-injected H-mode shot 99411: a) toroidal rotation frequencies  $\Omega_{\phi} \equiv V_{\phi} / R_0$  for deuterium and carbon; b) poloidal rotation velocities  $V_{\theta}$  for deuterium and carbon; c) normalized density asymmetry coefficients  $n^{s,c}$  for deuterium and carbon; d) radial electric field from carbon force balance using calculated and experiment  $V_{\theta,\phi}$  for carbon.

## V. Investigation of edge pedestal structure in DIII-D (DoE Grant ER54538)

W. M. Stacey and R. J. Groebner

(to be published in *Physics of Plasmas*, 2006)

### ABSTRACT

A calculation based on the requirements of particle, momentum and energy conservation, conductive heat transport and atomic physics resulting from a recycling and fueling neutral influx was employed to investigate the experimental density, temperature, rotation velocities and radial electric field profiles in the edge of three DIII-D [J. Luxon, Nucl. Fusion, 42, 614 (2002)] high-mode plasmas. The calculation indicated that the cause of the pedestal structure in the density was a momentum balance requirement for a steep negative pressure gradient to balance the forces associated with an edge peaking in the inward pinch velocity (caused by the observed edge peaking in the radial electric field and rotation velocity profiles) and, to a lesser extent, in the outward radial particle flux (caused by the ionization of recycling neutrals). Thermal and angular momentum transport coefficients were inferred from experiment and compared with theoretical predictions, indicating that thermal transport coefficients were of the magnitude predicted by neoclassical and ion-temperature-gradient theories (ions) and electron-temperature-gradient theory (electrons), but that neoclassical gyroviscous theory plus atomic physics effects combined were not sufficient to explain the inferred angular momentum transfer rate throughout the edge region.

### I. INTRODUCTION

A signature feature in high performance (H-mode) plasmas is the formation of a steep gradient edge region leading to pedestals in the density and temperature profiles in the plasma edge. The edge pedestal has been a subject of strong research interest, both experimental and theoretical, over the past decade, but an understanding of the physics of the pedestal structure remains elusive today. A review of work through 2000 may be found in Ref. 1.

The motivation for understanding the edge pedestal is based, at least in part, on calculations<sup>2,3</sup> which indicate that because of “stiffness” in temperature profiles the performance of future tokamaks will be sensitive to the value of the density and particularly the temperature at the top of the edge pedestal. Thus, understanding the edge pedestal characteristics would seem to be a prerequisite to predicting the performance of future tokamaks.

Recent work has focused on several different aspects of understanding the physics of the edge pedestal. Investigations (e.g. Refs. 4-6) of the MHD stability of the edge pressure pedestal against ballooning and peeling (surface kink) modes have advanced the ability to predict the onset of edge-localized-mode (ELM) instabilities which momentarily destroy the edge pedestal structure. Other investigations<sup>7-9</sup> have employed the physical conservation, transport and atomic physics constraints to understand the mechanisms that determine the observed edge pedestal structure that exists in the absence of or in between ELMS. A particle guiding center analysis<sup>10</sup> was employed to explain the pedestal formation in terms of the ionization of recycling neutrals, together with orbit squeezing and the presence of an X-point transport mechanism. Other studies<sup>11-13</sup> investigated the possibility that the width of the steep-gradient region was associated with the neutral penetration mean-free-path. Yet other studies (e.g. Refs. 14 and 15) had the objective of developing theory-based predictive correlations of measured pedestal parameters.

This paper falls in the second category of investigations mentioned above, in which the calculation is based rigorously on the particle balance, the three components of the momentum balance, the energy balance, the neutral transport equations that calculate the atomic physics terms in these equations, and the conductive heat transport relation  $q = -n\chi\nabla T$ ; i.e. on “physical conservation, transport and atomic physics constraints”. We extend our previous calculation of density and temperature profiles<sup>7-9</sup> to include the calculation of rotation velocities and the radial electric field in the plasma edge.

Such a calculation model is correct to the extent that all particle, torque, and energy sources are included, that all the cross-field energy and momentum transport processes are included, and that the approximations made in implementation are adequate. Therefore, it can be employed, together with experimental data, to relate the various measured profiles in the plasma edge for the purpose of identifying any missing particle, torque or energy sources and thermal and momentum transport processes

in the model, and to identify the cause-and-effect relations that determine the edge pedestal structure, which are the overarching objectives of this paper. We employ this calculation model: i) to infer thermal and momentum transport coefficients from experiment for comparison with theoretical predictions; ii) to check the agreement of the measured density, temperature, rotation velocities and radial electric field profiles with profiles calculated from these physical conservation, transport and atomic physics constraints, for the purpose of identifying any missing phenomena in the model; and iii) to interpret the causes of various features in the profiles (e.g. the density pedestal structure).

## II. EDGE DENSITY & TEMPERATURE PROFILES

### A. DIII-D shot parameters

We have chosen for detailed analysis a pair of heavily gas-fueled “density limit” shots (#97979 and #98893), with steep density pedestals and low to modest pedestal temperatures, and a quite different shot (#118583) with modest pedestal density and high pedestal temperatures. This choice of shots was guided by the wish to include shots with different neutral particle influxes<sup>11-13</sup> and plasma shapes<sup>16,17</sup>. The parameters of these shots are given in Table 1.

These shots have quite different collisionality profiles in the plasma edge, as shown by the normalized ion-impurity collision frequency in Fig. 1, which might be expected to cause somewhat different profiles in other variables. Here and in subsequent figures the separatrix is at 1.0.

**Table 1 Parameters of DIII-D Shots (R=1.71-1.77 m, a=0.6 m)**

Shot	$q_{95}$	$\kappa$	$\delta$	$P_{nb}$ (MW)	$f_{carb}$ (%)	$n_{ped}$ ( $m^{-3}$ )	$T_{eped}$ (eV)	$B$ (T)	$I$ (MA)
97979	3.9	1.7	0.75	6.5	1.1	6.3	525	1.6	1.4
98893	4.2	1.8	0.14	2.1	0.8	8.3	120	1.6	1.2
118583	3.8	1.8	0.37	9.2	6.0	2.8	720	1.9	1.4

### B. Requirement on pressure gradient

We found previously<sup>7-9</sup> that momentum balance and particle conservation requirements led to a constraint on the radial pressure gradient which for a two-species ion-impurity (i-I) model is of a simple pinch-diffusion form for the main ion species

$$L_{pi}^{-1} \equiv -\frac{1}{p_i^0} \frac{dp_i^0}{dr} = \frac{V_{ri} - V_{pinch,i}}{D_i} \quad (1)$$

where  $V_{ri} = \Gamma_{ri}/n_i^0$  is the radial particle velocity and  $V_{pinch,i}$  is a collection of terms

$$V_{pinch,i} = \frac{\left[ -M_{\phi i} - n_i e_i E_{\phi}^A + n_i m_i (\nu_{il} + \nu_{di}^*) \left( f_p^{-1} V_{\theta i} + \frac{E_r}{B_{\theta}} \right) - n_i m_i \nu_{il} V_{\phi I} \right]}{n_i e_i B_{\theta}} \quad (2)$$

which arises in the derivation from momentum balance,  $M_{\phi i}$  is the external momentum input (e.g. from neutral beams),  $E_{\phi}^A$  is the induced toroidal electric field,  $\nu_{il}$  is the interspecies collision frequency,  $\nu_{di}^*$  is the total frequency for radial momentum transfer by viscous, inertial, atomic physics and ‘anomalous’ processes,  $f_p \equiv B_{\theta}/B_{\phi}$ , and the other notation is standard. The quantity

$$D_i = \frac{m_i T_i \nu_{il}}{(e_i B_{\theta})^2} \left[ 1 + \frac{\nu_{di}}{\nu_{il}} - \frac{Z_i}{Z_I} \right] \quad (3)$$

is of the form of a diffusion coefficient. While the nomenclature ‘pinch velocity’ and ‘diffusion coefficient’ is used because Eq. (1) has the form of a pinch-diffusion relation for the particle flux

$(n_i V_{ri} = -(D_i/T_i)(dp_i/dr) + n_i V_{pinch,i})$ , we stress that Eqs. (1)-(3) were derived from momentum and particle balance requirements<sup>7</sup>.

The relatively simple form of Eq. (1) resulted because of the assumption that the impurity ion density distribution was the same as for the main ions and that the temperatures were the same. If these assumptions are relaxed, a more general matrix pinch-diffusion relation is obtained<sup>7</sup>.

### C. Requirements on temperature gradients

The heat conduction relations may be written as transport requirements on the temperature gradient scale lengths

$$L_{Ti,e}^{-1} = \frac{1}{\chi_{i,e}} \left[ \frac{Q_{i,e}}{n_{i,e} T_{i,e}} - \frac{5}{2} \frac{\Gamma_{i,e}}{n_{i,e}} \right] \quad (4)$$

where  $Q_j$  is the total heat flux for species “j”, and then subtraction of Eq. (4) from Eq. (1) yields a requirement on the density gradient scale length  $L_{ni}^{-1} = L_{pi}^{-1} - L_{Ti}^{-1}$ .

### D. Particle and heat flux, density and temperature profile calculations

The heat and particle balance equations may be integrated inwards from the separatrix, using experimental separatrix boundary conditions, to obtain the  $Q_{i,e}(r)$  and  $\Gamma(r)$  profiles<sup>7-9</sup> that are needed to evaluate Eqs. (4) and  $V_{ri}$ . This procedure takes into account the effect of atomic physics and radiation cooling in reducing the non-radiative heat fluxes with increasing radius and the effect of the ionization of recycling (and beam deposited) neutrals in increasing the particle flux with radius.

The gradient scale lengths can then be evaluated as a function of position from the above relations, and the definitions  $-(1/n)(dn/dr) = L_n^{-1}$  and  $-(1/T_{i,e})(dT_{i,e}/dr) = L_{Ti,e}^{-1}$  can be integrated inward from the separatrix, using experimental separatrix boundary conditions, to obtain the  $n(r)$  and  $T_{i,e}(r)$  profiles<sup>7-9</sup>.

Since these equations and the equations for the neutral density profile are coupled, the calculation is performed iteratively.

These equations are solved on a circular cross section toroidal model in which the model minor radius  $r$  is related to the non-circular plasma minor radius  $r'$  in the horizontal mid-plane by the mapping  $r = r' \sqrt{1/2(1 + \kappa^2)}$  that defines an effective circle that preserves the surface area of an ellipse of elongation  $\kappa$  with horizontal midplane radius  $r'$ . The normalized radius  $\rho = r/a$  (where  $a$  is related to plasma horizontal radius  $a'$  by the same mapping) is then identified with the flux surface function  $\rho$  for the purpose of comparison with experiment.

### E. Neutral transport

In order to evaluate the atomic physics particle sources and cooling terms in the particle and energy balance equations and to evaluate the charge-exchange/recombination enhancement of the radiation function for the carbon impurities, it is necessary to calculate the neutral deuterium concentration in the edge plasma. We employ a global code<sup>18</sup> which i) performs core plasma particle and power balance calculations (including beam heating and particle sources, neutral influx and radiative cooling) to determine the outward plasma particle and heat fluxes across the separatrix into the SOL, which ii) are input to a “2-point” divertor model (including atomic physics and radiative cooling, particle sources and momentum sinks) to calculate the background plasma density and temperature in the SOL and divertor and the ion flux incident on the divertor target plate, which in turn iii) determines the recycling neutral particle source for a 2D neutral transport calculation<sup>19</sup> that provides the neutral influx and density in the plasma edge. The neutral transport model explicitly represents the poloidal asymmetry of the neutral influx arising from the divertor plate recycling source and from external fueling sources. A

more detailed discussion of the neutral transport model and comparison with DIII-D neutrals measurements and Monte Carlo calculations can be found in Ref. 19.

#### F. *Experimental input to calculations*

In order to solve the six non-linear 1D differential equations and the 2D neutral transport equations described above for the radial profiles of the plasma quantities  $n, T_{i,e}, Q_{i,e}, \Gamma$  and the neutral density  $n_o$  in the edge region inside the separatrix, it is necessary to know the heat and momentum transport coefficients  $(\chi_{i,e}, \nu_{di,l}^*)$  and the rotation velocities and radial electric field profiles in the plasma edge, which latter enter Eq. (2) for the ‘pinch velocity’. Note that the particle transport (diffusion) coefficient of Eq. (3) is determined as part of the calculation.

Since one of our purposes in this section is to determine if the measured density and temperature profiles can be calculated from the physical conservation, transport and atomic physics constraints, and the experimental rotation velocities and radial electric field profiles, we use experimental values of the rotation velocities and radial electric field profiles  $(E_r = E_r^{ex}, V_{\theta i} = V_{\theta I} = V_{\theta carb}^{ex}, V_{\phi i} = V_{\phi I} = V_{\phi carb})$ , as well as experimental values of  $n(r_{sep}), T_{i,e}(r_{sep})$  and power and particle balance values of  $Q_{i,e}(r_{sep}), \Gamma(r_{sep})$  at the separatrix, in the calculations of the  $n, T_{i,e}, Q_{i,e}, \Gamma$  profiles discussed in this section.

#### G. *Inference of heat transport coefficients from experiment*

In order to calculate density, temperature and rotation profiles from the above equations we need to know the values of the heat,  $\chi_j$ , and momentum,  $\nu_{dj}^*$ , transport coefficients. The heat transport coefficient profiles for the main ions and electrons can be inferred from measured temperature gradients, densities and temperature, and calculated particle and heat fluxes. Conceptually, Eq. (3) can be rewritten as

$$\chi_{i,e} = L_{Ti,e} \left[ \frac{Q_{i,e}}{n_{i,e} T_{i,e}} - \frac{5}{2} \frac{\Gamma_{i,e}}{n_{i,e}} \right] \quad (5)$$

and the experimental gradients can be used to infer the heat conductivities, if the density, temperatures, and heat and particle fluxes are known. In practice, we have varied the  $\chi_{i,e}$  and repeated the entire solution procedure described in the previous sections until the calculated temperature profiles were in reasonable agreement with experiment; i.e. we have treated the  $\chi_{i,e}$  as adjustable parameters chosen to predict the experimental temperature profiles, within the context of the overall calculation. As such, these inferred values of the transport coefficients have intrinsic interest in their own right for comparison with theoretical predictions.

We previously found<sup>7,9</sup> that inferred heat transport coefficients (using a less sophisticated procedure of inference) did not vary greatly over the edge region for the DIII-D shots that we have examined, so we used a single value of  $\chi_{i,e}$  over the entire steep-density-gradient region and another single value over the flattop density region (in fact, we found the same value can be used over both regions in two of the three shots). This procedure could, of course, be fine-tuned by adjusting transport coefficients pointwise to obtain a more exact match to the measured temperature profiles, but this is not necessary for the purposes of this paper.

The heat transport coefficients thus inferred from experiment are given in Figs. 2. For shots 97979 and 118583, constant values of  $\chi_i$  and  $\chi_e$  over the entire edge region  $\rho > 0.85$  (including both the steep-density-gradient and flattop density regions) sufficed for the calculated temperature profiles to match the measured values, while somewhat different constant values in the sharp-gradient and flattop density regions were needed to get a good match for shot 98893. The resulting calculated ion and electron temperature distributions are compared with measured values in Figs. 3 and 4.

The inferred constant value of the heat transport coefficients shown in Figs. 2a and 2c differ from the usual inference (e.g. Ref 20) that the steep gradient observed in the edge temperature pedestal (more pronounced for the electrons than the ions) is due to a sharply decreasing with radius value of  $\chi_{i,e}$ . Figures 3a and 3c, and to a lesser degree Figs. 4a and 4c, show that a single value of  $\chi_{i,e}$  suffices to produce a reasonable match to the measured temperature profiles in shots 97979 and 118583 in both the “flat-top” and “steep-gradient” regions. While the temperature pedestals are not as sharp as the density pedestals in these shots, these results clearly show that a sharp reduction in the transport coefficient in the steep-gradient region just inside the separatrix is not a necessary condition for an edge temperature pedestal. We defer a discussion of the cause of the temperature pedestal in these shots until a later section.

We note that the magnitudes of the inferred  $\chi_{i,e}$ ’s in both the “flat-top” and “steep-gradient” edge regions are significantly smaller than are usually inferred in both the core plasma of H-mode discharges and in the edge plasma of L-mode discharges consistent with the usual observation of reduced thermal diffusivity in the edge regions of H-mode discharges.

For comparison with theory, Chang-Hinton neoclassical (w/orbit squeezing) and ITG mode predictions of the deuterium ion heat transport coefficients and the ETG mode prediction of the electron heat transport coefficients are also shown in Figs. 2. These heat transport coefficient predictions, expressions for which are given in appendix A, are certainly ‘in the ballpark’, and the agreement of the ETG  $\chi_e$  with the value inferred from experiment for the low collisionality shot 118583 is remarkable. These comparisons encourage the suggestion that more detailed transport calculations be undertaken to understand the transport in the edge plasma.

#### H. Inference of momentum transfer rates from experiment

In order to evaluate Eqs. (1)-(3) for the pressure gradient, we need to know the momentum transfer frequency  $\nu_{dj}^*$ . This quantity can be inferred from the measured toroidal rotation velocity.

The flux surface average of the toroidal component of the momentum balance equation for each ion species ‘j’ can be written

$$n_j^0 m_j \nu_{jk}^0 \left( (1 + \beta_j) V_{\phi j}^0 - V_{\phi k}^0 \right) = n_j^0 e_j E_\phi^A + e_j B_\theta^0 \Gamma_j + M_{\phi j}^0 \equiv n_j^0 m_j \nu_{jk}^0 y_j, \quad (6)$$

where  $M_{\phi j}$  is the momentum input from the neutral beams,  $M_{\phi j}^{nb}$ , and possibly from other “anomalous” mechanisms,  $M_{\phi j}^{anom}$ , and the radial transfer of toroidal momentum by viscous, inertial, and atomic physics and perhaps other processes is represented by the parameter

$$\beta_j \equiv \frac{\nu_{dj}^0 + \nu_{nj}^0 + \nu_{ionj,nb}^0 + \nu_{ionj}^0 + \nu_{elcx,j}^0 + \nu_{anom,j}^0}{\nu_{jk}^0} \equiv \frac{\nu_{dj}^0 + \nu_{nj}^0 + \nu_{atom,j}^0 + \nu_{anom,j}^0}{\nu_{jk}^0} \equiv \frac{\nu_{dj}^*}{\nu_{jk}^0} \quad (7)$$

where

$$\nu_{dj}^0 \equiv \frac{\langle R^2 \nabla \phi \cdot \nabla \cdot \boldsymbol{\pi}_j \rangle}{R_0 n_j^0 m_j V_{\phi j}^0} \quad (8)$$

is the frequency for the radial viscous transport of toroidal angular momentum,

$$\nu_{nj}^0 \equiv \frac{\langle R \nabla \phi \cdot (n_j m_j (\mathbf{V}_j \cdot \nabla) \mathbf{V}_j) \rangle}{R_0 n_j^0 m_j V_{\phi j}^0} \quad (9)$$

is the frequency for the radial transport of toroidal angular momentum due to inertial effects,  $\nu_{atom,j}^0$  is the frequency for loss of toroidal momentum due to atomic physics processes (ionization, charge-exchange, elastic scattering), and  $\nu_{anom,j}$  is the frequency for loss of toroidal momentum by “anomalous” processes (e.g. turbulent transport, ripple viscosity).

The ion-electron friction term has been neglected, a sum over other species ‘k’ is implied in general, and the collisional momentum conservation requirement  $n_j^0 m_j v_{jk}^0 = n_k^0 m_k v_{kj}^0$  has been used in writing Eq. (6). The “0” superscript denotes the flux surface averaged value.

In the above formulation, we have distinguished between external angular momentum torque sources or sinks ( $RM_{\phi j}, Rn_j e_j E_\phi^A, Re_j B_\theta \Gamma_{rj}$ ) which do not depend on the rotation velocity, on one hand, and angular momentum loss rates due to neoclassical viscosity, inertia and atomic physics processes of the form  $Rn_j m_j v_d V_{\phi j}$  which do depend on the rotation velocity. The latter processes are “drag” processes which can reduce, but not reverse, the predominant direction of toroidal rotation velocity determined by the direction of the neutral beam injection, while the torque input processes are capable of increasing, decreasing or reversing the toroidal velocity.

Our objective in this section is to use the measured toroidal rotation velocity (for C VI) in Eq. (6) to infer a value of the quantity  $v_{dj}^*$ , then calculate the neoclassical gyroviscous, inertial and atomic physics  $v_{dj}$  for comparison, and attribute any difference to “anomalous” transport processes. We note that the observation of toroidal rotation in plasmas without neutral beam injection or other obvious sources of torque input implies that there are “anomalous” input torques present under certain conditions. (Here we are using “anomalous” in the usual sense of “not understood”, rather than not understandable.) We could, alternatively, solve Eq. (6) for  $M_{\phi j}^{anom}$  by using a calculated  $v_{dj}^*$ , but this would have the problem of neglecting the possibility of any other momentum transport processes increasing  $v_{dj}^*$ . Since there is no way to solve one equation for two unknowns, we elect to infer  $v_{dj}^*$  from Eq. (6), with the caveat that we may thereby be forcing an “anomalous” torque input process to be represented by an “anomalous” angular momentum loss rate formalism.

The toroidal momentum balance equations, Eqs. (6), can be solved for the main and impurity ion momentum transfer, or “drag”, frequencies

$$v_{di}^* = \frac{\frac{M_{\phi i}^0}{n_i^0 m_i} + \frac{e_i}{m_i} E_\phi^A + \frac{e_i}{m_i} B_\theta V_{ri} - v_{il}^0 (V_{\phi i}^0 - V_{\phi I}^0)}{V_{\phi I}^0 - (V_{\phi i}^0 - V_{\phi I}^0)} \quad (10)$$

and

$$v_{dl}^* = \frac{\frac{M_{\phi I}^0}{n_I^0 m_I} + \frac{e_I}{m_I} E_\phi^A + v_{il}^0 (V_{\phi i}^0 - V_{\phi I}^0)}{V_{\phi I}^0} \quad (11)$$

in a 2-species model, where  $V_{ri}^0 = 0$  has been assumed. Alternatively, a single drag frequency applicable to both ion species can be evaluated by adding the two Eqs. (6) for ions and impurities to obtain

$$v_d^* = \frac{(M_{\phi i}^0 + M_{\phi I}^0) + e(n_i Z_i + n_I Z_I) E_\phi^A + n_i e Z_i B_\theta V_{ri}}{(n_i m_i + n_I m_I) V_{\phi I}^0 + n_i m_i (V_{\phi i}^0 - V_{\phi I}^0)} \quad (12)$$

The measured carbon rotation velocity can be used to evaluate  $V_{\phi I}^0 = V_{\phi carbon}^{exp}$  in the above equations. However, we do not know the ion toroidal velocity from experiment. We could subtract the radial components of the momentum balance equations for each ion species

$$\left( \frac{E_r^0}{B_\theta^0} \right) = V_{\phi j}^0 - f_p^{-1} V_{\theta j}^0 + P_j^0 \quad (13)$$



where

$$P_j^{0'} \equiv \frac{1}{B_\theta^0 n_j^0 e_j} \frac{\partial p_j^0}{\partial r}, \quad (14)$$

to evaluate the velocity difference

$$(V_{\phi i}^0 - V_{\phi l}^0) = (V_{\theta i}^0 - V_{\theta l}^0) f_p^{-1} - (P_i^{0'} - P_l^{0'}) \quad (15)$$

However, this requires knowledge the poloidal velocities, one of which (C VI) is measured, but with considerable uncertainty, and the other of which is not measured. Thus, for the purpose of evaluating the inferred momentum transport frequency, the toroidal velocity difference term in Eq. (12) is set to zero.

We note that the difference in toroidal rotation velocities for deuterium and carbon has been calculated from Eq. (15) to be significant in some low collisionality DIII-D shots<sup>21</sup>. When we calculated separate toroidal rotation velocities for deuterium and carbon ions for the shots considered in this paper, they were identical for the higher collisionality shots #97979 and #98893, but differed somewhat for the less collisional shot #118583, as discussed in a later section. We further note that the error introduced by this approximation is of the order of the difference in species rotation velocities, not of the order of the rotation velocities, and is small for these shots.

The experimental angular momentum radial transfer frequency of Eq. (12) is plotted for the edge region of shots #97979 and #98893 in Figs. 5. Also shown for comparison are the calculated atomic physics angular momentum loss frequency,  $\nu_{atom,j}^0 = \nu_{ionj,nb}^0 + \nu_{ionj}^0 + \nu_{elcx,j}^0$ , neoclassical gyroviscous angular momentum transport frequency,  $\nu_{gyro,j}$ , and inertial transfer frequency,  $\nu_{nj}^0$ , the latter two being defined in appendix B. It would appear that atomic and neoclassical momentum transfer processes are not large enough to account for the experimentally inferred momentum transfer rate throughout the steep-gradient and flat-top regions of the plasma edge in these discharges, although they become large enough to do so just inside the separatrix. We further note that the form of the gyroviscosity used in this paper, which depends only on flow gradients, may over-predict momentum transport in regions of subsonic flow with steep gradients<sup>22</sup> such as these edge regions. We interpret these results as evidence that some additional “anomalous” moment transport (e.g. magnetic braking, ripple viscosity, turbulent transport) or torque input processes must be involved, at least further inside the separatrix.

For shot #118583, the carbon toroidal rotation velocity reversed direction and became negative over  $0.92 \leq \rho \leq 0.97$ , possibly indicating the presence of an “anomalous” input torque. On the other hand, Eq. (15) allows the possibility that the deuterium ions, which constitute the majority of the plasma mass, were rotating in the direction of beam injection but the pressure gradient and poloidal velocity differences reversed the rotation of the impurity ions. For consistency with the treatment of the other two shots, the drag frequency was determined from Eq. (12) with the same  $V_{\phi i}^0 = V_{\phi l}^0 = V_{\phi carbon}^{exp}$  assumption, which correctly incorporated the effect of the experimental toroidal rotation velocity into the overall calculation, but resulted in a negative value of the inferred  $\nu_{dj}^*$  over this radial interval of negative rotation velocity.

### I. Cause of the pedestal structure

With reference to Eq. (2), the pinch velocity depends on 1) the momentum input due to the beams and to the toroidal electric field, 2) the toroidal rotation velocity for the impurity species, 3) the radial electric field, and 4) the poloidal rotation velocity of the deuterium ions. (We note that this expression may be written in different ways by making use of the above radial and toroidal momentum equations; this particular form has been chosen to best make use in its evaluation of measured quantities.) The beam momentum input was calculated from a simple beam attenuation model, and the induced toroidal electric field was measured; both contributions were small. The carbon toroidal rotation velocity and the radial electric field were determined from experiment. Consistent with the assumption  $V_{\theta i} = V_{\theta l} = V_{\theta carb}^{ex}$  made

in this section, the deuterium poloidal velocity that enters the equation was evaluated from the measured carbon poloidal velocity, introducing an error of order of the difference  $V_{\theta i} - V_{\theta carb}^{ex}$ . The contributions of these different terms to the pinch velocity are plotted in Figs. 6a and 6b for shots #97979 and #98893. In both shots there is a strong negative peaking in the pinch velocity just inside the separatrix that is driven mainly by the radial electric field, but also in part by edge peaking in the rotation velocities.

As shown in Eq. (1), the pressure gradient is determined by the difference in the forces associated with the (outward) radial particle flux and the (inward) pinch velocity. The radial deuterium ion velocity  $V_{ri} = \Gamma/n_i$  peaks just inside the separatrix because of the peaking in  $\Gamma$  due to the ionization of recycling and fueling neutrals and because of the decrease in  $n_i$ . As discussed above, the pinch velocity has a strong negative peaking just inside the separatrix. These two effects add to produce a strong negative pressure gradient just inside the separatrix that decreases with distance from the separatrix, as shown in Figs. 6c and 6d. We note that  $V_{ri} = \Gamma/n_i$  is the ion velocity that would be measured if it were possible to do so, but that  $V_{pinch}$  is a constructed quantity and that no particles would actually be found moving with this velocity; diffusion down the density gradient is driving particles outward and  $V_{pinch}$  is driving them inward—the resultant is  $V_r$ .

Since the ion pressure gradient is much steeper than the ion temperature gradient  $L_{pi}^{-1} \gg L_{Ti}^{-1}$  just inside the separatrix, but the two become comparable further inside the separatrix, the ion density gradient  $L_{ni}^{-1} = L_{pi}^{-1} - L_{Ti}^{-1}$  is large just inside the separatrix but becomes small with increasing distance inside the separatrix. When  $-(1/n_i)(dn_i/dr) = L_{ni}^{-1}$  is then integrated inward from the separatrix, using an experimentally determined separatrix boundary condition, the resulting electron density profiles shown in Figs. 7 are obtained. These clearly are in sufficiently good agreement with the measured (Thomson) density profiles to support the conclusion that the edge pedestal density structure is a consequence of the requirement of Eq. (1) on the edge pressure gradient, given the experimentally determined rotation velocities and radial electric field profiles. It does not, of course, explain the cause of the experimentally inferred transport coefficients nor of the measured rotation velocities and radial electric fields that were used as input for the calculations. We will return to this latter matter in the next section.

The usual explanation for the cause of temperature pedestals is based on the heat fluxes in the edge “flat-top” and “steep-gradient” regions being approximately the same and both satisfying the conductive relation  $q = -n\chi dT/dr = const$ . Since  $dT/dr$  is much larger in the pedestal “steep-gradient” region than in the “flat-top” region, the product  $n\chi$  must be proportionally smaller in the “steep-gradient” than in the “flat-top” region. The conventional wisdom is that this requires that  $\chi$  be smaller in the “steep-gradient” than “flat-top” region. However, in these shots  $n$  is observed and calculated to decrease rapidly with radius just inside the separatrix, and a constant value of  $\chi$  over the flat-top and steep gradient regions was inferred from experiment for two of the shots, as discussed previously. Thus, we conclude that the main cause of the steep gradient that causes the temperature pedestal (at least for  $T_e$ ) in these shots is the requirement that the temperature gradient must increase to offset the decrease of density in the steep gradient region. In other words, the temperature pedestals are required by heat removal requirements to exist because there is a density pedestal.

We have discussed the calculations of this section in sequence, as if one followed the other, for the sake of exposition. It is necessary to emphasize that this was not the case. The equations are coupled and non-linear, and they had to be solved by iterating to convergence.

#### J. *Role of neutrals in pedestal formation*

The calculated edge neutral density profiles are shown for the three shots in Fig. 8. Comparison of Figs. 7 and 8 clearly indicate that the shot (#98893) with the largest pedestal density and most rapidly attenuated neutral density profile inside the separatrix is also the shot with the steepest edge density gradient and smallest edge density width, and conversely that shot #118583 with the smallest pedestal density and weakest neutral density attenuation has the largest pedestal width. Also the effective neutral attenuation mean free path (the distance over which the neutral density attenuates by a factor of  $e^{-1}$ ) in all three shots is comparable to the pedestal width, as has been noted previously<sup>11-13</sup>. However, by

comparison with Figs. 6, we also note that the phenomena which cause the steep edge pressure gradient extend several neutral mean free paths inside the separatrix. In this section we try to identify ‘cause and effect’ physical relationships by which neutrals affect the pedestal structure.

We have already discussed the effect of the ionization of the influx of recycling and fueling neutrals in causing a peaking in the ion radial velocity profile just inside the separatrix, which in turn produced an increase in the negative ion pressure gradient just inside of the separatrix, as illustrated in Figs. 6. However, the edge peaking of the pinch velocity produced a larger effect on the edge pressure gradient in the shots considered in this paper. Thus, it is interesting to investigate whether the ionization of recycling and fueling neutrals also indirectly affected the edge pressure gradient through effects on the phenomena that caused the edge peaking in the pinch velocity.

Because we are modeling shots which are primarily fueled by the influx of recycling and injected neutrals, we can’t just turn the neutrals off in the calculation and see what happens—we would no longer get a solution even remotely close to the experimental conditions. So we had to resort to a different stratagem to infer the magnitude of neutral ionization effects on the phenomena that cause the edge peaking in the pinch velocity. When we included the recycling and fueling neutrals in the particle balance but ignored their effect in the solution of the particle continuity equation (i.e. used a spatially constant  $\Gamma$ ), we of course obtained a reduced edge peaking in the radial ion velocity  $V_{ri} = \Gamma / n_i$  due only to the decreasing  $n_i$ . We also obtained a resulting factor of 2 reduction in the edge peaking in the pinch velocity due to using a constant  $\Gamma$  over the calculation region. The two effects combined to predict a reduction in the edge pressure gradient by a smaller factor, which when integrated inward from the separatrix predicted a pedestal with a larger width and about 70% of the original pedestal flattop density.

Thus, the direct mechanism by which the neutral influx contributes to the pedestal formation is to cause a peaking in the ion flux just inside the separatrix due to ionization. This peaking in the particle flux causes a peaking in the ion radial velocity  $V_{ri} = \Gamma / n_i$  just inside the separatrix, which contributes directly to a strong negative pressure gradient  $-(1/p_i)(dp_i/dr) = (V_{ri} - V_{pinch,i})/D_i$  just inside the separatrix. There are further indirect effects of the neutral ionization on the density profile--the effect of the peak in  $\Gamma$  on the particle and temperature distributions and the effect of the peaking in  $V_{ri}$  on  $V_\theta$ , and hence on  $V_{pinch,i}$ . However, these indirect effects of neutral ionization do not dominate  $V_{pinch,i}$ , hence do not dominate the determination of the strong pressure gradient just inside the separatrix that causes the density pedestal structure, at least not in the shots that we have examined.

#### K. Diffusion coefficient

The diffusion coefficient of Eq. (3) is plotted for shots #9797 and #98893 in Fig. 9. The variation is caused mainly by the variations in collision frequency and momentum transfer frequency given in Figs. 1 and 5. The calculated diffusion coefficient clearly does not reduce significantly in the “steep-gradient” region relative to the “flat-top” region for these shots.

### III. ROTATION VELOCITIES AND RADIAL ELECTRIC FIELD

We established in the previous section that, given the experimental rotation and radial electric field profiles in the edge plasma and the experimentally inferred transport coefficients, the physical conservation requirements (particle, momentum, energy), the heat conduction transport relation, and atomic physics effects of recycling and fueling neutrals were sufficient to determine the observed density and temperature pedestal structure. We now turn the situation around and investigate if, given the profiles of heat and particle fluxes, plasma and neutral densities, and ion and electron temperatures determined in the previous section (and the experimentally inferred transport coefficients), the physical conservation, transport and atomic physics requirements are sufficient to determine the observed rotation and radial electric field profiles. In other words, we check to see if the calculation model of this paper contains an adequate representation of the particle, torque, and energy sources and the momentum transport mechanisms to enable calculation of the measured rotation velocities and radial electric field profiles from

the measured density and temperature profiles using the physical conservation, transport and atomic physics constraints.

#### A. Poloidal rotation

Equations for the poloidal rotation velocities were derived from poloidal momentum balance using a neoclassical expression for the parallel viscosity (Appendix C). These equations were solved numerically, using fixed density and temperature profiles calculated in the previous section and using  $V_{\phi i}^0 = V_{\phi l}^0 = V_{\phi carbon}^{\text{exp}}$  consistent with the assumptions of the previous section. (The subsequent calculation of toroidal rotation velocities for deuterium and carbon supports this approximation.) The results are shown in Figs. 10. The positive sense of the velocities is in the positive  $\theta$ -direction in a right-hand ( $r$ - $\theta$ - $\phi$ ) system with the positive  $\phi$ -direction in the direction of the plasma current (fingers of the right hand in the positive  $\theta$ -direction when right thumb in the plasma current direction). For these Co-injected shots, the positive sense of the poloidal rotation shown in Figs. 9 was downward at the outboard mid-plane.

Both the measured and calculated C VI poloidal rotation velocities are small, and there is no significant disagreement within the uncertainty of the measurements, except in the outer region in shot #118583, over roughly the same radial interval in which the measured and calculated toroidal rotation velocities are negative. The predicted deuterium poloidal rotation velocity is the same as the carbon rotation velocity for the highest pedestal density shot #98893, but departs progressively from the calculated carbon rotation velocity with decreasing collisionality, and the two calculated velocities had opposite signs for the least collisional shot #118583. With the possible exception of this outer region in shot #118583, the agreement of calculated and measured poloidal rotation velocities for carbon would seem to indicate that the relevant poloidal torques and momentum loss rates (neoclassical parallel viscosity, atomic physics) are being included in the poloidal rotation equations of appendix C.

#### B. Toroidal rotation

The toroidal momentum balance Eqs. (6) for ions and impurities can be summed to obtain an expression for the deuterium ion toroidal velocity

$$V_{\phi i}^0 = \frac{eZ_i B_\theta^0 \Gamma_i + (M_{\phi i} + M_{\phi l}) + e(n_i^0 Z_i + n_l^0 Z_l) E_\phi^A}{n_i^0 m_i v_{il} (\beta_i + \beta_l)} + \frac{\beta_l (V_{\phi i}^0 - V_{\phi l}^0)}{(\beta_i + \beta_l)} \quad (16)$$

and then the impurity momentum balance equation can be solved for

$$V_{\phi l}^0 = \frac{V_{\phi i}^0}{(1 + \beta_l)} + \frac{M_{\phi l} + n_l^0 e Z_l E_\phi^A}{n_l^0 m_l v_{il} (1 + \beta_l)} \quad (17)$$

The difference in species' toroidal rotation in Eq. (16) can be evaluated by subtracting the radial momentum balance equations for the two species to obtain Eq. (15) and using the difference in poloidal velocities calculated in the previous section, along with the difference in pressure gradients, to evaluate that expression.

The results of this calculation are compared with experiment in Figs. 11. Since Eq. (12) was used to solve the summed Eqs. (6) for  $v_{di}^*$ , under the assumption  $V_{\theta i}^0 = V_{\theta l}^0 = V_{\theta carbon}^{\text{exp}}$ , and then  $v_{di}^*$  was used in the same set of equations, but without this assumption, to calculate the toroidal rotation in Eqs. (16) and (17), the agreement for the carbon toroidal velocities shown in Figs. 11 is a check on the assumption  $V_{\phi i}^0 = V_{\phi l}^0 = V_{\phi carbon}^{\text{exp}}$  used to evaluate Eq. (12) for  $v_{di}^*$  and on the consistency of the overall calculation procedure. We have already drawn conclusions about the need for an additional input negative torque or momentum loss rate to explain the inferred  $v_{di}^*$ .

#### C. Radial electric field

The radial electric field was calculated by evaluating the radial momentum balance of Eq. (13) for the carbon species, using the calculated values of the carbon pressure gradient and rotation velocities. The results are compared with the “measured” radial electric field, also constructed using Eq. (13) but with the measured values of the CVI pressure gradient and rotation velocities, in Figs. 12. The agreement is good except just inside the separatrix in shot #98893, where a much stronger negative peaking is predicted than measured; this is a result of the stronger predicted than measured negative carbon pressure gradient (i.e. to the inadequacy of the assumption in the calculation that the carbon concentration was uniform). Particularly noteworthy is that the measured negative well structure in the radial electric field for shot #118583 was predicted. The pressure gradient and rotation velocity components of  $E_r$  are also shown for shot #118583.

#### IV. SUMMARY AND CONCLUSIONS

A detailed analysis of the edge pedestal structure (density, temperature, rotation velocities, and radial electric field profiles) in three DIII-D H-mode discharges was carried out using equations based on the physical conservation (particles, three components of momentum, energy) and transport (heat conduction) requirements and including the atomic physics processes involving recycling and fueling neutrals. The calculation model was employed, together with experimental data, to infer the thermal and momentum transport coefficients, to relate the various measured profiles in the plasma edge for the purpose of identifying any missing particle, torque or energy sources and thermal and momentum transport processes in the model, and to identify the cause-and-effect relations that determine the edge pedestal structure---the overarching objectives of this paper.

The heat conduction and momentum transport coefficients were inferred from measured temperature and toroidal velocity profiles, as part of the overall computation procedure, and compared with theoretical predictions. The inferred thermal transport coefficients were of comparable magnitude to those predicted by simple prescriptions based on neoclassical and ion-temperature-gradient theory (ions) and electron-temperature-gradient theory (electrons). Toroidal angular momentum transport rates inferred from experiment were not fully accounted for over the entire steep-gradient and flattop region of the edge by neoclassical gyroviscous and atomic physics momentum transfer mechanisms, indicating a need for additional “anomalous” momentum transport or torque input mechanisms to explain the edge toroidal and poloidal rotation velocities profiles, and hence the radial electric field profile—a significant new result of this paper.

Next, the experimental rotation velocities and radial electric field profiles, the experimentally inferred transport coefficients, and the calculated fueling and recycling neutral influx were used together with the equations derived from the physical conservation, transport and atomic physics constraints to calculate the density and temperature profiles, which were in reasonable agreement with measured values, including the prediction of the observed edge density pedestal structure. These calculations confirmed our previous conclusion<sup>7-9</sup> that the principal mechanism for the edge density pedestal formation was the momentum balance requirement for a large negative pressure gradient to balance the force associated with the edge peaking of an inward particle pinch velocity and (to a lesser extent) the force associated with the edge peaking of the radial ion particle velocity. A new result of this paper was the demonstration that the edge peaking of the inward pinch velocity was driven via momentum balance by the observed edge peaking of the radial electric field and of the rotation velocities. The edge peaking of the radial ion particle velocity was required by the particle balance in the presence of an ionization source of recycling neutrals and by a decreasing plasma density in the edge.

Then the calculation was turned around. A set of equations for the poloidal and toroidal rotation velocities and the radial electric field was derived from the physical conservation, transport and atomic physics requirements. The density and temperature profiles calculated in the first part (which were close to the measured profiles), the particle and heat flux profiles calculated in the first part, the toroidal angular momentum transport coefficients inferred from experiment, and the influx of recycling and fueling neutrals calculated in the first part were used as input to solve this second set of equations. The calculated poloidal and toroidal rotation velocities profiles for carbon and the radial electric field profile generally agreed with experimental values within the uncertainty in the measurements. The agreement of toroidal velocities only confirmed the consistency of the calculation, since the experimentally inferred angular momentum transport coefficients were used in the calculation, but the agreement of poloidal velocities

confirmed that the important poloidal torques and momentum loss rates (neoclassical parallel viscosity, atomic physics) were being included in the poloidal rotation equations—a significant new result of this paper.

It was possible to obtain reasonable agreement between the calculated and measured temperature profiles in both the “flat-top” and “steep-gradient” regions of the edge plasma ( $\rho > 0.85$ ) by using a radially constant value of the inferred thermal conduction coefficient in two of the three shots considered. Moreover, the calculated diffusion coefficient decreased only slightly in the steep-gradient region in one shot, while increasing in the other two. Thus, it seems that the steep-gradient-region in the edge of H-mode shots is not necessarily associated with a sharp decrease in transport coefficients, as is commonly thought—another new result of this paper. The inferred and calculated particle and heat transport coefficients in the edge were smaller than are usually inferred either in the core of H-mode plasmas or the edge of L-mode plasmas, consistent with other observations.

A secondary objective of this investigation was to better understand the physical mechanisms by means of which recycling and fueling neutrals affected the edge pedestal structure. Our calculations indicated that the observed density pedestals were caused by the momentum balance requirement for a steep negative pressure gradient to balance forces associated with edge peaking and inward pinch velocity and in an outward radial ion particle velocity. The ionization of recycling and fueling neutrals in the edge directly caused the peaking in the outward radial particle velocity, but this term was calculated to be less important than the inward pinch velocity, in the shots considered. The neutral influx also affects the terms that constitute the inward pinch velocity in at least two ways: 1) the edge peaking in the radial particle velocity produces a peaking in the  $eV_r \times B_\phi$  torque in the poloidal momentum balance equations that contributes to the edge peaking in  $V_\theta$ ; and 2) charge exchange, elastic scattering and ionization constitute angular momentum damping mechanisms that affect the toroidal and poloidal rotation velocities in the edge; both of which in turn affect the radial electric field. Subsidiary calculations indicated that the first above indirect effect on the pinch velocity plus the direct effect of the edge peaking in the radial particle flux could account for  $\approx 30\%$  of the edge pressure gradient requirement being due to neutrals—another interesting new result. There may be other effects of the neutral influx that have not been taken into account in the calculations.

Further efforts along this line of investigation are suggested by the above discussion: 1) detailed gyro-kinetic or gyro-fluid thermal transport calculations in the plasma edge to obtain more accurate predictions of ion and electron thermal diffusivities; 2) investigation of torque input and angular momentum transport mechanisms in the plasma edge in addition to those included in the calculation model of this paper, including kinetic phenomena; 3) improvement of some of the approximations made in implementing the physical conservation and transport constraints (e.g. uniform impurity concentration); 4) improvement in solution procedures for the constraint equations; and 5) further detailed analysis of measured edge profiles.

## Appendix A: Thermal Transport Coefficients

### Neoclassical

The Chang-Hinton expression for the ion thermal conductivity is<sup>23</sup>

$$\chi_i^{ch} = \varepsilon^{1/2} \rho_{i\theta}^2 v_{ii} \left[ a_1 g_1 + a_2 (g_1 - g_2) \right] \quad (\text{A1})$$

where the  $a$ 's account for impurity, collisional and finite inverse aspect ratio effects and the  $g$ 's account for the effect of the Shafranov shift. These parameters are collected in the appendix to Ref. 7.

In the presence of a strong shear in the radial electric field, the particle banana orbits are squeezed, resulting in a reduction in the ion thermal conductivity by a factor of  $S^{-3/2}$ , where<sup>24</sup>

$$S = \left| 1 - \rho_{i\theta} \left( \frac{d \ln E_r}{dr} \right) \left( \frac{E_r}{v_{thi} B_\theta} \right) \right| \quad (\text{A2})$$

Here  $\rho_{i\theta}$  is the ion poloidal gyroradius.

### *Ion temperature gradient modes*

For a sufficiently large ion temperature gradient ( $L_{Ti} < L_{Ti}^{crit} \simeq 0.1R$ ) the toroidal ion temperature gradient (ITG) modes become unstable. An estimate of the ion thermal conductivity due to ITG modes is<sup>25</sup>

$$\chi_i^{ig} = \frac{5}{2} \left( \frac{1}{RL_{Ti}} \right)^{1/2} \left( \frac{T_e}{m_i} \right) \left( \frac{m_i}{e_i B} \right) \frac{1}{2} \rho_i \quad (\text{A3})$$

where  $\rho_i$  is the gyroradius in the magnetic field  $B$ , and  $k_\perp \rho_i = 2$  has been used..

### *Electron temperature gradient modes*

The electron temperature gradient (ETG) modes (electrostatic drift waves with  $k_\perp c_s \leq \omega_{pe}$ ) are unstable when  $\eta_e \equiv L_n / L_{Te} \geq 1$ . An expression for the thermal conductivity due to the ETG modes is given by<sup>26</sup>

$$\chi_e^{etg} = 0.13 \left( \frac{c_s}{\omega_{pe}} \right)^2 \frac{v_{the} S_m}{qR} \eta_e (1 + \eta_e) \quad (\text{A4})$$

where  $S_m \equiv (r/q)(dq/dr)$  is the magnetic shear and  $\omega_{pe}$  is the electron plasma frequency.

## **Appendix B: Neoclassical viscous and inertial momentum transport frequencies**

### *Viscous ‘‘Drag’’*

The largest component of neoclassical viscosity that enters the flux surface averaged toroidal momentum balance equation is the gyroviscous component<sup>27-30</sup>. An expression for the neoclassical gyroviscous momentum transfer, or drag, frequency can be derived<sup>28</sup> in toroidal geometry by using the representations  $R = R_0 (1 + \varepsilon \cos \theta)$  and  $B = B^0 / (1 + \varepsilon \cos \theta)$ , replacing the radial gradients by gradient scale lengths (e.g.  $L_n^{-1} = -1/n \partial n / \partial r$ ), and expanding the poloidal dependence of densities and velocities in a low-order Fourier series of the form

$$n_j(r, \theta) = n_j^0 \left[ 1 + n_j^c(r) \cos \theta + n_j^s(r) \sin \theta \right] \quad (\text{B1})$$

to obtain a representation of the toroidal viscous torque in terms of an angular momentum transfer, or ‘‘drag’’, frequency,  $\nu_{di}$

$$\left\langle R^2 \nabla \phi \cdot \nabla \cdot \boldsymbol{\pi}_j \right\rangle_{\text{gv}} \simeq \frac{1}{2} \tilde{\theta}_j G_j \frac{n_j m_j T_j}{e_j B_\phi} \frac{V_{\phi j}^0}{R} \equiv R n_j m_j \nu_{dj} V_{\phi j}^0 \quad (\text{B2}) \text{ where}$$

$$\begin{aligned} \tilde{\theta}_j &\equiv (4 + \tilde{n}_j^c) \tilde{V}_{\phi j}^s + \tilde{n}_j^s (1 - \tilde{V}_{\phi j}^c) \\ &= (4 + \tilde{n}_j^c) \left( -(\hat{V}_{\theta j} / \hat{V}_{\phi j}) (\tilde{\Phi}^s + \tilde{n}_j^s) + \tilde{\Phi}^s \left( 1 + \left( \hat{P}_j' / \hat{V}_{\phi j} \right) \right) \right) + \\ &\tilde{n}_j^s \left( (\hat{V}_{\theta j} / \hat{V}_{\phi j}) (\tilde{\Phi}^c + \tilde{n}_j^c + 2) - \tilde{\Phi}^c \left( 1 + \left( \hat{P}_j' / \hat{V}_{\phi j} \right) \right) \right) \end{aligned} \quad (\text{B3})$$

represents poloidal asymmetries and

$$G_j \equiv -\frac{r}{\eta_{4j} V_{\phi j}} \frac{\partial(\eta_{4j} V_{\phi j})}{\partial r} = r(L_n^{-1} + L_T^{-1} + L_{V_\phi}^{-1}) \quad (\text{B4})$$

represent radial gradients. We have used the gyroviscosity coefficient  $\eta_{4j} \approx n_j m_j T_j / e_j B$  and introduced the notation

$$\hat{V}_{\theta j} \equiv \frac{V_{\theta j}^0}{f v_{thj}}, \hat{V}_{\phi j} \equiv \frac{V_{\phi j}^0}{v_{thj}}, \hat{P}_j \equiv \frac{1}{n_j^0 e_j B_\theta^0 v_{thj}} \frac{\partial \bar{p}_j}{\partial r}, f_p \equiv \frac{B_\theta}{B_\phi}, \tilde{n}_j^{c/s} \equiv \frac{n_j^{c/s}}{\varepsilon}, \tilde{\Phi}^{c/s} \equiv \frac{\Phi^{c/s}}{\varepsilon} = \frac{n_e^{c/s}}{\varepsilon(e\Phi/T_e)} \quad (\text{B5})$$

with the last relation following from electron momentum balance, and neglected radial gradients in the density asymmetry coefficients  $n_j^{c,s}$ .

The radial gradient scale lengths needed to evaluate the  $G_j$  from Eq. (B4) are taken from experiment, and the density asymmetries needed to evaluate  $\tilde{\theta}_j$  from Eq. (B3) from the poloidal momentum equations described in appendix C.

*Inertial “drag”*

The toroidal component of the inertial term in the angular momentum balance equation in toroidal geometry is

$$R^2 \nabla \phi \cdot n_j m_j (\mathbf{V}_j \cdot \nabla) \mathbf{V}_j = R n_j m_j \left( V_{rj} \frac{\partial V_{\phi j}}{\partial r} + \frac{V_{rj} V_{\phi j}}{R} - \frac{V_{\phi j}}{r} \frac{\partial V_{\theta j}}{\partial \theta} - \frac{V_{\phi j} V_{\theta j}}{R} \sin \theta \right) \quad (\text{B6})$$

Flux surface averaging and following a procedure similar to that outlined above leads to an equivalent expression for the “inertial drag” term

$$\nu_{nj} \equiv V_{rj} \left[ \frac{1}{R_0} - \frac{1}{L_{v\phi}} \right] - \frac{1}{2} \frac{\varepsilon V_{\theta j}^0}{R_0} \left[ -\tilde{V}_{\theta j}^c (\tilde{V}_{\phi j}^s + \tilde{n}_j^s) + V_{\theta j}^s ((2 + \tilde{V}_{\phi j}^c + \tilde{n}_j^c) + (\tilde{V}_{\theta j}^s + \tilde{V}_{\phi j}^s + \tilde{n}_j^s)) \right] \quad (\text{B7})$$

where

$$\tilde{V}_{\theta j}^s = \tilde{I}_j^s B_\theta^0 / \varepsilon n_j^0 - \tilde{n}_j^s V_{\theta j}^0, V_{\theta j}^c = \tilde{I}_j^c B_\theta^0 / \varepsilon n_j^0 - (1 + \tilde{n}_j^c) V_{\theta j}^0 \quad (\text{B8})$$

and the quantities

$$\tilde{I}_j^s = r \tilde{S}_j^c, \tilde{I}_j^c = -r \tilde{S}_j^s \quad (\text{B9})$$

represent the sine and cosine components of the asymmetry in the ionization source.

### Appendix C: Poloidal rotation and density asymmetry calculation

We follow and extend somewhat our previous work<sup>31</sup> to develop equations for the poloidal rotation velocities and density asymmetries in the plasma edge in this section. The poloidal component of the momentum balance equation for ion species “j” is

$$n_j m_j \left[ (\mathbf{V}_j \cdot \nabla) \mathbf{V}_j \right]_\theta + [\nabla \cdot \Pi_j]_\theta + \frac{1}{r} \frac{\partial p_j}{\partial \theta} - M_{\theta j} - F_{\theta j} + \quad (\text{C1})$$

$$n_j e_j (V_{rj} B_\phi - E_\theta) + m_j (n_j v_{elcx} + V_{\theta j} \tilde{S}_j) = 0$$

where  $S_j - \langle S_j \rangle \equiv \tilde{S}_j$  and the poloidal components of the inertial and viscous terms are



$$n_j m_j [(\mathbf{V}_j \cdot \nabla) \mathbf{V}_j]_\theta = n_j m_j \left[ V_{rj} \frac{\partial V_{\theta j}}{\partial r} + \frac{V_{rj} V_\theta}{r} + \frac{1}{2} \frac{1}{r} \frac{\partial V_{\theta j}^2}{\partial \theta} + \frac{V_{\phi j}^2}{R} \sin \theta \right] \quad (C2)$$

and

$$[\nabla \cdot \Pi_j]_\theta = \eta_{0j} \left( \frac{1}{2} A_{0j} \right) \left\{ \frac{1}{r} \frac{\partial \ln(\eta_{0j} A_{0j})}{\partial \theta} - 3 \frac{\sin \theta}{R} \right\} \quad (C3)$$

where

$$A_0 = 2 \left\{ -\frac{1}{3} \left( \frac{\partial V_p}{\partial l_p} \right) + \left[ \left( \frac{1}{R} \right) \frac{\partial R}{\partial l_p} + \frac{1}{3} \left( \frac{1}{B_p} \right) \frac{\partial B_p}{\partial l_p} \right] V_p + f_p R \frac{\partial \left( \frac{V_\phi}{R} \right)}{\partial l_p} \right\} \quad (C4)$$

and the neoclassical parallel viscosity coefficient is represented by<sup>32</sup>

$$\eta_{0j} = \frac{n_j m_j \nu_{thj} q R \varepsilon^{-3/2} \nu_{jj}^*}{(1 + \varepsilon^{-3/2} \nu_{jj}^*)(1 + \nu_{jj}^*)} \equiv n_j m_j \nu_{thj} q R f_j (\nu_{jj}^*) \quad (C5)$$

where  $\nu_{jj}^* = \nu_{jj} q R / \nu_{thj}$  and  $\varepsilon = r/R$ .

Making low-order Fourier expansions of the form

$$n_j(r, \theta) = n_j^0(r) + n_j^s \sin \theta + n_j^c \cos \theta \quad (C6)$$

and taking the flux surface average with weighting functions 1,  $\sin \theta$  and  $\cos \theta$  results in a coupled set of equations (three times the number of ion species) that can be solved for the  $V_{\theta j}^0$  and  $\tilde{n}_j^{s,c}$  for all the plasma ion species. If the first term on the right in Eq. (C2) is neglected, these equations can be solved locally on each radial flux surface. The justification for this neglect would be the plausible assumption  $V_{rj} \ll V_{\theta j} < V_{\phi j}$ , which would also justify neglect of the second term on the right in Eq. (C2), relative to the last two terms. The resulting equations are

$$\begin{aligned} & \hat{V}_{\theta j} \left[ -q \hat{V}_{\phi j} \varepsilon \left( \tilde{n}_j^s + \tilde{\Phi}^s \right) - q^2 f_j f_p \left( 1 + \tilde{\Phi}^c + \frac{2}{3} \tilde{n}_j^c \right) + f_p \sum_{k \neq j} \nu_{jk}^* + \right. \\ & \left. \frac{q}{\varepsilon} \nu_{elcx,j}^* f_p + \frac{1}{2} f_p \varepsilon \nu_{ionj}^* \left\{ \left( 1 + \tilde{n}_j^c \right) \left( \frac{n_e^0}{n_j^0} \left( \tilde{n}_e^c + \tilde{n}_{oj}^c \right) - \left( \tilde{n}_j^c + \tilde{n}_{oj}^c \right) \right) + \right. \right. \\ & \left. \left. \tilde{n}_j^s \left( \frac{\tilde{n}_e}{n_j} \left( \tilde{n}_e^s + \tilde{n}_{oj}^s \right) - \left( \tilde{n}_j^s + \tilde{n}_{oj}^s \right) \right) \right\} \right] - \sum_{k \neq j} \hat{V}_{k\theta} \left[ f_p \nu_{jk}^* \sqrt{\frac{m_j}{m_k}} \right] = \\ & -\hat{V}_{rj} - q \varepsilon \frac{1}{4} \tilde{n}_j^s - q \varepsilon \hat{\Phi}_j \left[ \frac{1}{4} \left( \tilde{\Phi}^s + \tilde{n}_j^c \tilde{\Phi}^s - \tilde{n}_j^s \tilde{\Phi}^c \right) \right] - q^2 f_j f_p \left( \hat{V}_{\phi j} + \hat{P}_j \right) \tilde{\Phi}^c \\ & - q \varepsilon \hat{V}_{\phi j} \left[ \left( \hat{V}_{\phi j} + \hat{P}_j \right) \tilde{\Phi}^s + \frac{1}{2} \hat{V}_{\phi j} \tilde{n}_j^s \right] - \frac{n_e^0}{n_j^0} \nu_{ionj}^* q \left[ \hat{V}_{\phi j} \varepsilon \left( \tilde{n}_e^c + \tilde{n}_{oj}^c \right) \right. \\ & \left. - \frac{2}{3} q f_j \left( \tilde{n}_e^s + \tilde{n}_{oj}^s \right) \right] \end{aligned} \quad (C7)$$

$$\begin{aligned}
& \tilde{n}_j^s \left[ \frac{1}{3} \frac{q^2}{\varepsilon} f_j f_p \hat{V}_{\theta j} + \frac{1}{2} \varepsilon \hat{V}_{rj} - \frac{1}{2} \varepsilon f_p \sum_{k \neq j} v_{jk}^* \hat{V}_{\theta k} \sqrt{\frac{m_j}{m_k}} + \frac{1}{2} q v_{ionj}^* f_p \hat{V}_{\theta j} \right] \\
& + \tilde{n}_j^c \left[ \frac{1}{2} q f_p^2 \hat{V}_{\theta j}^2 - \frac{1}{4} q + \frac{1}{2} q v_{elcx,j}^* v_{ionj}^* \right] = -\frac{1}{2} \varepsilon f_p \sum_{k \neq j} v_{jk}^* \hat{V}_{\theta j} \tilde{n}_k^s \\
& - \frac{1}{4} q \hat{\Phi}_j \left[ -\bar{\Phi}^c \right] - \frac{q^2}{\varepsilon} f_j f_p \left[ \frac{1}{2} \left( \hat{V}_{\theta j} - \hat{V}_{\phi j} - \hat{P}_j \right) \bar{\Phi}^s - \frac{1}{2} q f_p^2 \hat{V}_{\theta j}^2 - \frac{1}{2} q \hat{V}_{\phi j}^2 \right. \\
& \left. - \frac{1}{2} q v_{elcx,j}^* \left[ f_p \hat{V}_{\theta j} \tilde{n}_{oj}^s + v_{ionj}^* \tilde{n}_{oj}^c \right] - q v_{ionj}^* f_p \left[ \frac{1}{2} \hat{V}_{\theta j} \left\{ \tilde{n}_{oj}^s \left( 1 + \frac{n_e^0}{n_j^0} \right) + \frac{n_e^0}{n_j^0} \tilde{n}_e^s \right\} \right. \right. \\
& \left. \left. + \frac{1}{3} \frac{q}{\varepsilon} f_j \frac{n_e^0}{n_j^0} \left( \tilde{n}_e^c + \tilde{n}_{oj}^c \right) \right] \right]
\end{aligned} \tag{C8}$$

and

$$\begin{aligned}
& \tilde{n}_j^c \left[ \frac{1}{3} \frac{q^2}{\varepsilon} f_j f_p \hat{V}_{\theta j} + \frac{1}{2} \varepsilon \hat{V}_{rj} - \frac{1}{2} \varepsilon f_p \sum_{k \neq j} v_{jk}^* \hat{V}_{\theta k} \sqrt{\frac{m_j}{m_k}} + \frac{1}{2} q v_{ionj}^* f_p \hat{V}_{\theta j} \right] \\
& + \tilde{n}_j^s \left[ -\frac{1}{2} q f_p \hat{V}_{\theta j}^2 + \frac{1}{4} q - \frac{1}{2} q v_{elcx,j}^* v_{ionj}^* \right] = -\sum_{k \neq j} \tilde{n}_k^c \left[ \frac{1}{2} \varepsilon f_p v_{jk}^* \hat{V}_{\theta j} \right] \\
& - \frac{1}{4} q \hat{\Phi}_j \left[ \bar{\Phi}^s \right] - \frac{q^2}{\varepsilon} f_j f_p \left[ \frac{1}{2} \left\{ \left( 1 + \bar{\Phi}^c \right) \hat{V}_{\theta j} - \left( \hat{V}_{\phi j} - \hat{P}_j \right) \bar{\Phi}^c \right\} \right] \\
& - q \hat{V}_{\phi j}^2 \left[ \frac{1}{4} \varepsilon \left\{ \tilde{V}_{\phi j}^s \tilde{V}_{\phi j}^c + \tilde{n}_j^c \tilde{V}_{\phi j}^s + \tilde{n}_j^s \tilde{V}_{\phi j}^c \right\} \right] - \frac{1}{2} q v_{elcx,j}^* \left[ f_p \hat{V}_{\theta j} \tilde{n}_{oj}^c - v_{ionj}^* \tilde{n}_{oj}^s \right] \\
& - q f_p v_{ionj}^* \left[ \frac{1}{2} \hat{V}_{\theta j} \left\{ \tilde{n}_{oj}^c \left( 1 + \frac{n_e^0}{n_j^0} \right) + \frac{n_e^0}{n_j^0} \tilde{n}_e^c \right\} + \frac{1}{3} \frac{q}{\varepsilon} f_j \frac{n_e^0}{n_j^0} \left( \tilde{n}_e^s + \tilde{n}_{oj}^s \right) \right]
\end{aligned} \tag{C9}$$

where

$$\begin{aligned}
\hat{V}_{rj} & \equiv \frac{V_{rj}^0}{\left( \frac{m_j \nu_{thj}}{e_j B_\phi^0} \right) \left( \frac{\nu_{thj}}{qR} \right)}, \quad \hat{\Phi}_j \equiv \frac{e_j \Phi^0}{T_j}, \\
v_{jk}^* & \equiv \frac{\nu_{jk}^0}{\frac{\nu_{thj}}{qR}}, \quad v_{ionj}^* \equiv \frac{\left( \nu_{ionj}^0 + \nu_{ionj,nb}^0 \right) r}{\nu_{thj}}, \quad v_{elcx,j}^* \equiv \frac{\nu_{elcx,j}^0 r}{\nu_{thj}},
\end{aligned} \tag{C10}$$

In the above,  $\nu_{ionj}^0$  is the ionization frequency of recycling and gas fueling neutrals,  $\nu_{ionj,nb}^0 = S_{nbj}^0 / n_j^0$  is the ionization frequency of neutral beam particles, and  $\nu_{elcx,j}^0$  is the charge-exchange plus elastic scattering frequency of ‘cold’ recycling neutrals.

## REFERENCES

1. A. E. Hubbard, Plasma Phys. Control. Fusion, 42, A283 (2000).
2. M. Kotschenreuther, W. Dorland, Q. P. Liu, *et al.*, Proc. 16<sup>th</sup> Conf. Plasma Phys Control. Fusion Res., Montreal, 1996 (IEAE, Vienna, 1997), Vol. 2, p 371.
3. J. E. Kinsey, R. E. Waltz and D. P. Schissel, Proc. 24<sup>th</sup> Eur. Phys. Soc., Berchtesgarden, 1997, Vol. III, p 1081.
4. J. W. Connor, R. J. Hastie, H. R. Wilson and R. L. Miller, Phys. Plasmas, 5, 2687 (1998).
5. P. B. Snyder, H. R. Wilson, J. R. Ferron, *et al.*, Phys. Plasmas, 9, 2037, (2002).
6. P. B. Snyder, H. R. Wilson, J. R. Ferron, *et al.*, Nucl. Fusion, 44, 320 (2004).
7. W. M. Stacey, Phys. Plasmas, 11, 1511 (2004).
8. W. M. Stacey, Phys. Plasmas, 11, 5487 (2004).
9. W. M. Stacey and R. J. Groebner, Phys. Plasmas, 12, 042504 (2005).
10. C. S. Chang, S. Ku and H. Weitzner, Phys. Plasmas, 11, 2649 (2004).
11. R. J. Groebner, M. A. Mahdavi, A. W. Leonard, *et al.*, Phys. Plasmas, 9, 2134 (2002).
12. R. J. Groebner, M. A. Mahdavi, A. W. Leonard, *et al.*, Nucl. Fusion, 44, 204 (2004).
13. W. M. Stacey and R. J. Groebner, Phys. Plasmas, 10, 2412 (2003).
14. R. J. Groebner and T. H. Osborne, Phys. Plasmas, 5, 1800 (1998).
15. T. Onjun, G. Bateman, A. Kritz, *et al.*, Phys. Plasmas, 9, 5018 (2002).
16. W. Suttrop, O. Gruber, B. Kurzan, *et al.*, Plasma Phys. Control. Fusion, 42, A97 (2000).
17. T. H. Osborne, J. R. Ferron, R. J. Groebner, *et al.*, Plasma Phys. Control Fusion, 42, A175 (2000).
18. W. M. Stacey, Phys. Plasmas 5, 1015 (1998); 8, 3673 (2001).
19. W. M. Stacey, Nucl. Fusion, 40, 965 (2000).
20. L. D. Horton, A. V. Chankin, Y. P. Chen, *et al.*, Nucl. Fusion, 45, 856 (2005).
21. L. R. Baylor, K. H. Burrell, R. J. Groebner, *et al.*, Phys. Plasmas, 11, 3100 (2004).
22. H. A. Claassen, H. Gerhauser, A. Rogister, *et al.*, Phys. Plasmas, 7, 3699 (2000).
23. C. S. Chang and F. L. Hinton, Phys. Fluids, 29, 3314 (1986).
24. K. C. Shaing and R. D. Hazeltine, Phys. Fluids B, 4, 2547 (1992).
25. F. Romanelli, W. M. Tang and R. B. White, Nucl. Fusion, 26, 1515 (1986).
26. J. A. Wesson, *Tokamaks*, 2<sup>nd</sup> ed. (Clarendon Press, Oxford, 1997).
27. S. I. Braginskii, Rev. Plasma Phys., 1, 205 (1965).
28. A. B. Mikhailovskii and V. S. Tsypin, Sov. J. Plasma Phys., 10, 51 (1984).
29. W. M. Stacey and D. J. Sigmar, Phys. Fluids, 28, 2800 (1985).
30. P. J. Catto and A. N. Simakov, Phys. Plasmas, 12, 012501 (2005).
31. W. M. Stacey, Phys. Plasmas, 9, 3874 (2002).
32. W. M. Stacey, A. W. Bailey, D. J. Sigmar and K. C. Shaing, Nucl. Fusion, 25, 463 (1985).

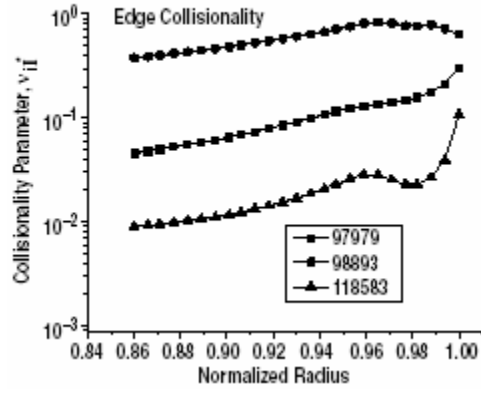


Fig. 1 Normalized deuterium-carbon collisionality parameter  $v_{il}^* = v_{il} q R / v_{thi}$ .

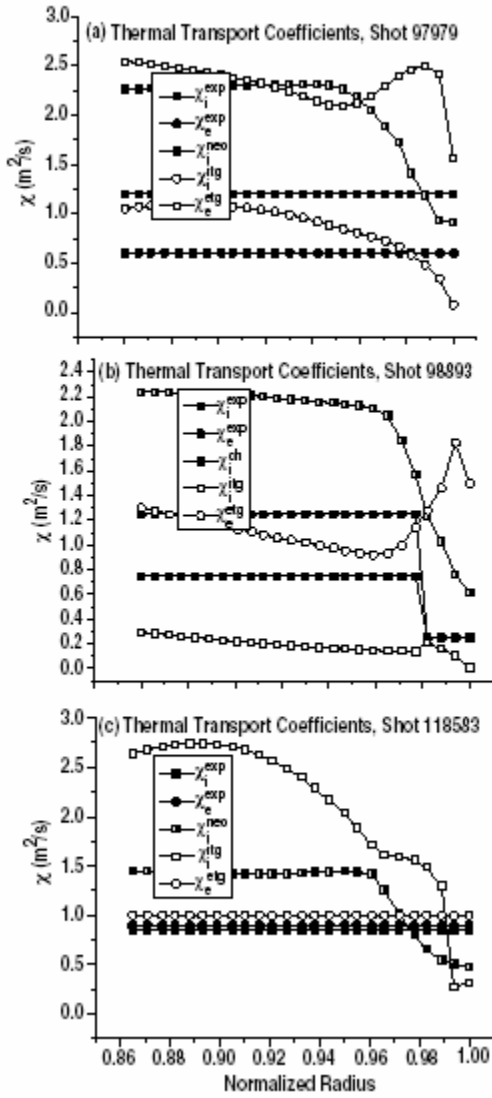


Fig. 2 Thermal transport coefficients inferred from experiment (solid symbols) compared with theoretical estimates from neoclassical, ITG and ETG theories.

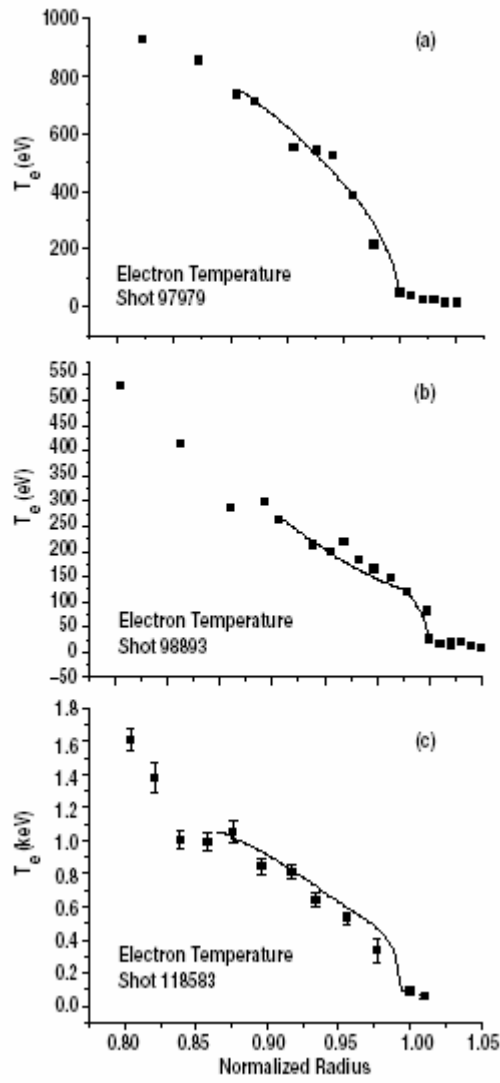


Fig. 3 Calculated (solid line) and measured electron temperatures.

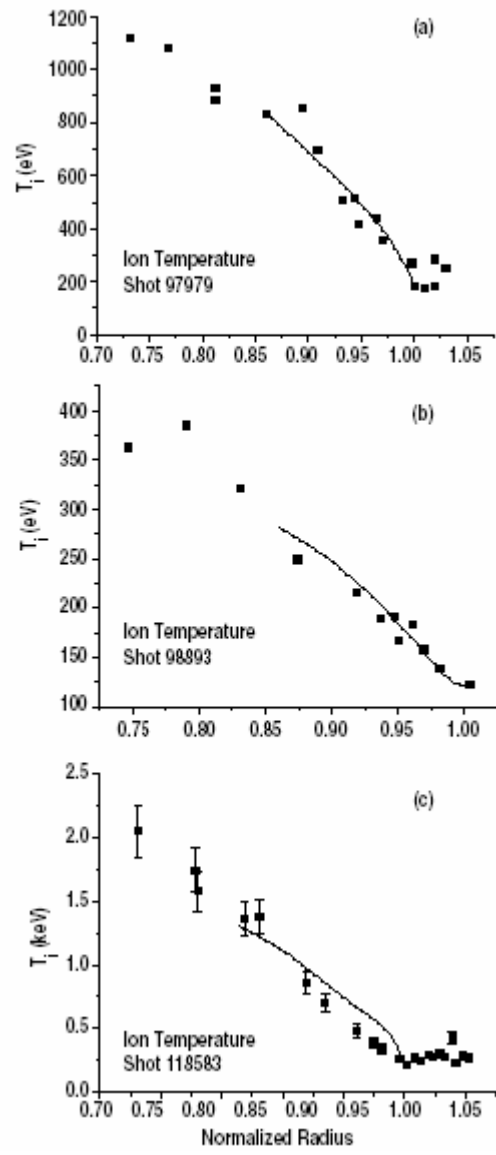


Fig. 4 Calculated (solid line) and measured ion temperatures.

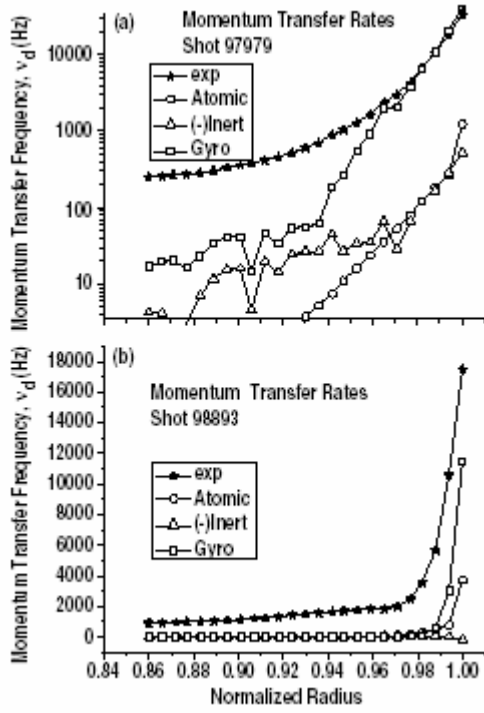


Fig. 5 Total frequency for the radial transfer of toroidal angular momentum inferred from experiment (solid stars) compared with calculated angular momentum transfer frequencies due to atomic physics, inertial effects and neoclassical gyroviscosity.

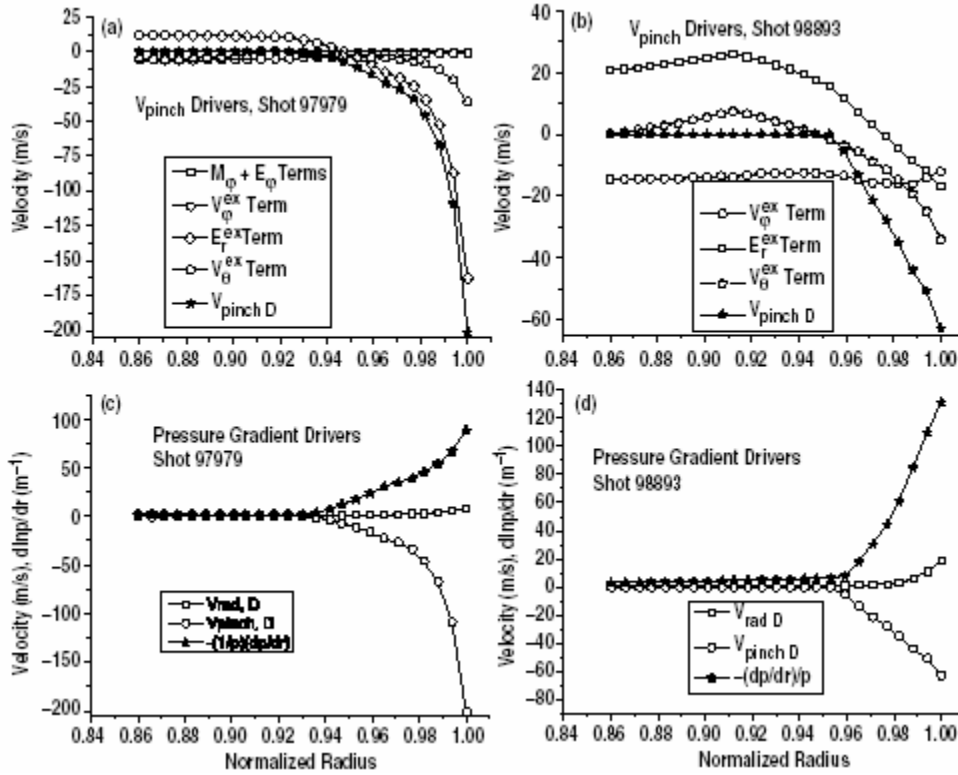


Fig. 6 Phenomenological causes of the edge pressure pedestal: a) and b) phenomena contributing to the inward deuterium pinch velocity; and c) and d) contributions of the inward pinch velocity and the radial particle velocity to the deuterium pressure gradient.

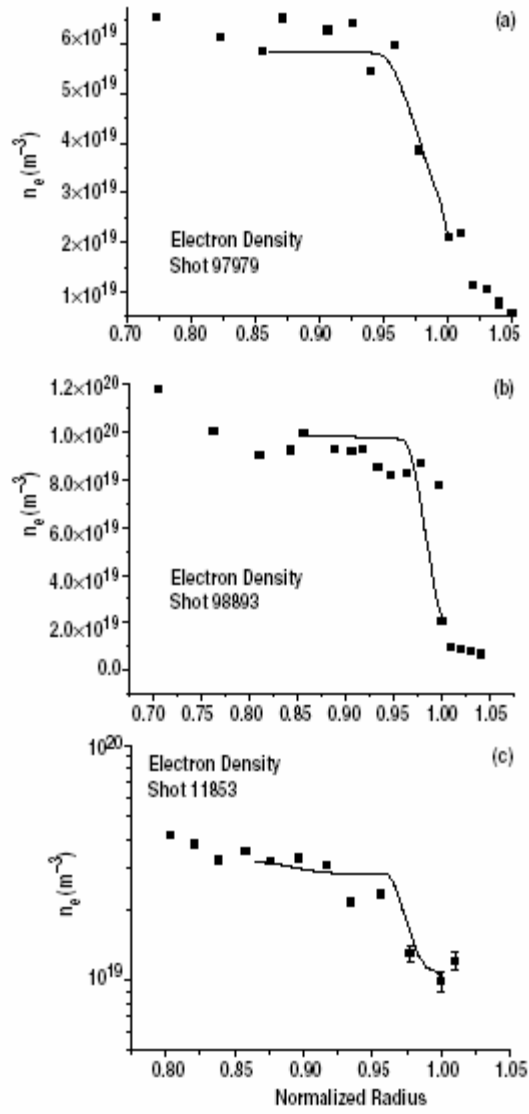


Fig. 7 Calculated (solid line) and measured electron densities.

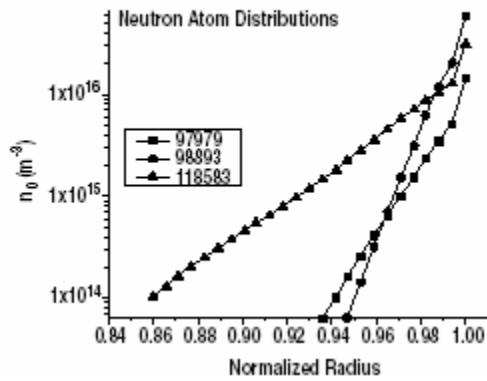


Fig. 8 Calculated neutral densities.



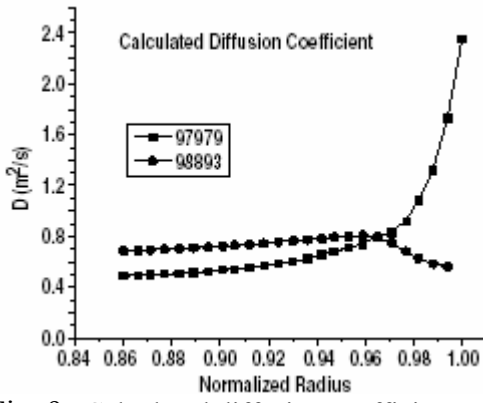


Fig. 9 Calculated diffusion coefficients.

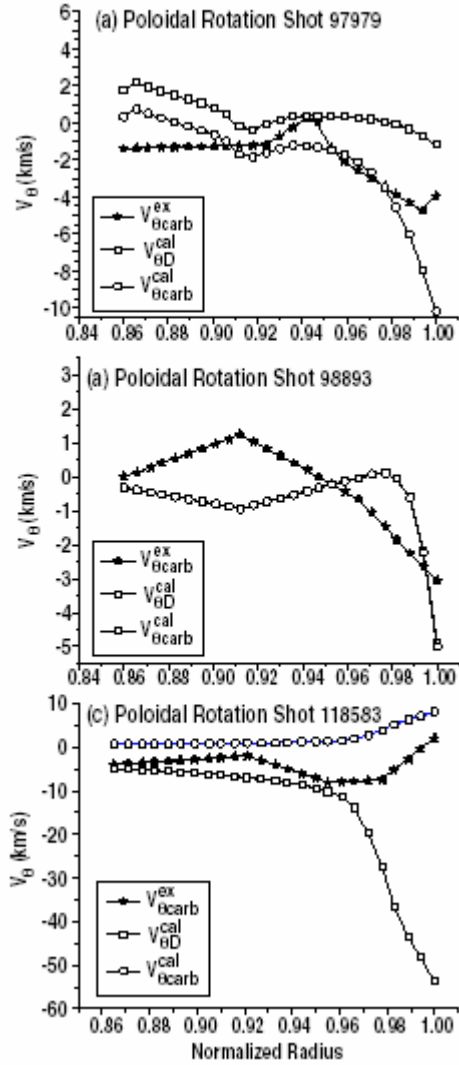


Fig. 10. Calculated deuterium and carbon poloidal rotation velocities (empty symbols) from poloidal momentum balance using neoclassical parallel viscosity compared with measured carbon VI poloidal rotation velocity (solid star). Note that the sign convention is different for the calculated and measured velocities.

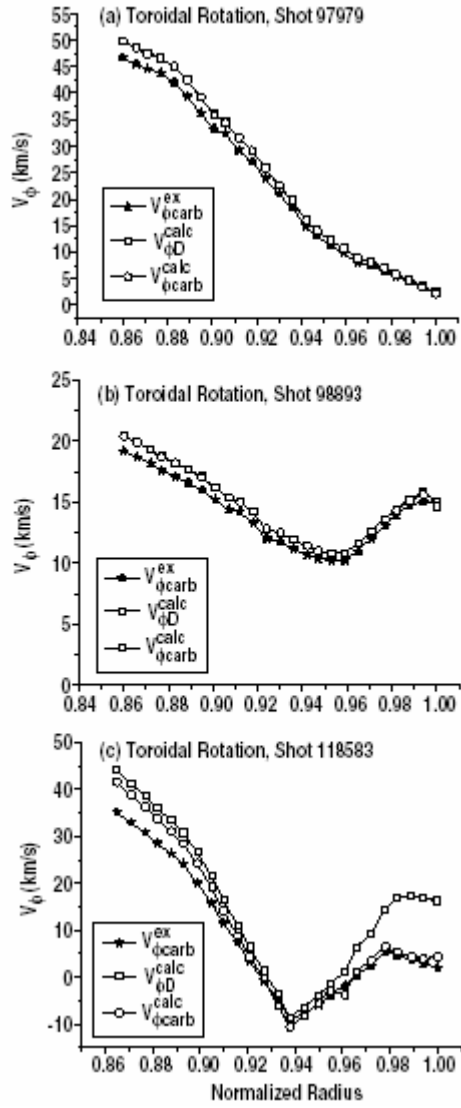


Fig. 11 Calculated deuterium and carbon toroidal rotation velocities (empty symbols) from toroidal momentum balance using same inferred momentum transfer frequency compared with measured carbon VI toroidal rotation velocity (solid star).

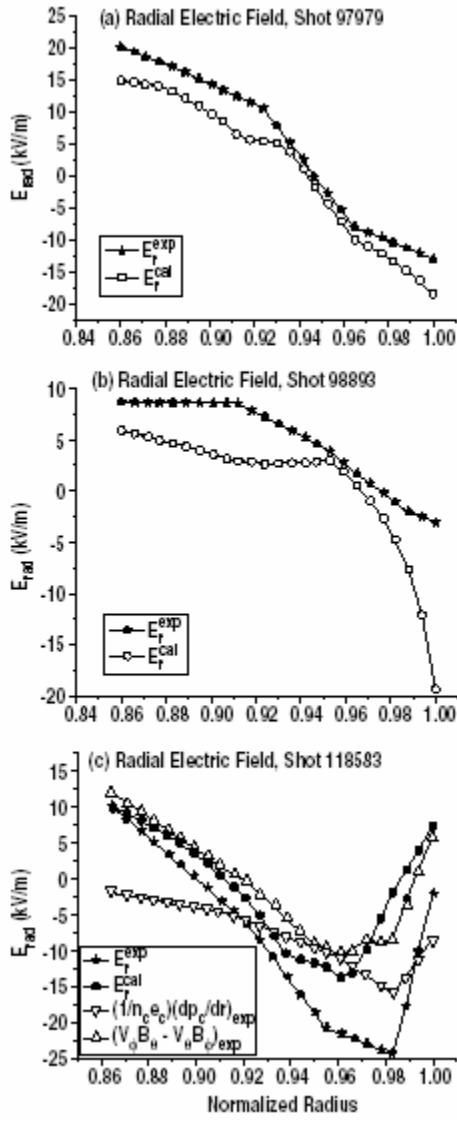


Fig. 12 Calculated radial electric field from radial momentum balance for carbon using calculated carbon pressure gradient and rotation velocities (circle symbol) compared with the experimental radial electric field calculated the same way but using measured carbon VI pressure gradient and rotation velocities (solid star). Also shown are the pressure gradient and  $V \times B$  components of the experimental radial electric field.

## **VI. A sub-critical, He-cooled, fast reactor for the transmutation of spent nuclear fuel (DOE Grant ER54350)**

W. M. Stacey, Z. Abbasi, C. J. Boyd, A. H. Bridges, E. A. Burgett, M. W. Cymbor, S. W. Fowler, A. T. Jones, R. S. Kelm, B. J. Kern, D. B. Lassiter, J. A. Maddox, W. B. Murphy, H. Park, J. M. Pounders and J. R. Preston

*(to be published in Nuclear Technology, 2006)*

### **Abstract**

A design concept and supporting analysis are presented for a He-cooled, fast reactor for the transmutation of spent nuclear fuel. Coated TRU fuel particles in a SiC matrix are used. The reactor operates sub-critical ( $k \leq 0.95$ ), with a tokamak D-T fusion neutron source, to achieve  $> 90\%$  TRU burnup in repeated 5-batch fuel cycles, fissions 1.1 MT/FPY, and produces 700 MWe net electrical power. The reactor design is based on nuclear, fuels, materials and separations technologies being developed in the GEN-IV, NGNP and AFCI Programs and similar international programs, and the fusion neutron source is based on the physics and technology supporting the ITER design.

### **I. INTRODUCTION**

Advanced reactor concepts with fuel cycles that better utilize fuel resources and reduce high-level waste repository requirements are being studied intensively in the U. S. Generation-IV Nuclear Energy Systems Initiative<sup>1</sup> (GEN-IV) and Advanced Fuel Cycle Initiative<sup>2</sup> and in related studies world-wide. In parallel, as part of the Next Generation Nuclear Plant (NGNP) Project<sup>3</sup>, an R&D program is underway on the further development of coated fuel particle technology with an objective of achieving extremely high burnup without fission product release.

The further development of coated fuel particle technology has stimulated the examination of ‘deep-burn’ transmutation reactors that could destroy up to 90% or more of the transuranic (TRU) waste remaining in the spent nuclear fuel (SNF) from light water reactors (LWRs) in thermal<sup>4</sup> and fast<sup>5</sup> gas-cooled reactors. In both cases, 90% burnup was achieved by subcritical operation, with an accelerator<sup>4</sup> or fusion<sup>5</sup> neutron source.

Our purpose in this paper is to extend our previous study<sup>5</sup> of a subcritical, He-cooled fast reactor with coated TRU fuel particles and a tokamak D-T fusion neutron source, denoted GCFTR (Gas Cooled Fast Transmutation Reactor). As in the previous study, the design objectives were 1) to achieve  $\geq 90\%$  TRU burnup and 2) to use a physics and technology design basis for both the reactor and the fusion neutron source that either exists or is being developed in ongoing R&D programs, so that a 2040 deployment timescale is feasible.

The paper is organized as follows. An overview of the new GCFTR-2 design concept, the materials and major parameters of the principal systems, the performance parameters, and the radiation damage lifetimes of the principal components are given in Section II. The aqueous reprocessing system for separating the TRU from the SNF, the coated TRU fuel particle and its fabrication system, an analysis of the coated TRU fuel particle lifetime against fission product gas buildup and corrosion, and the study of fuel element configuration leading to the choice of the coated particle embedded in a SiC matrix fuel pin configuration are presented in Section III. The nuclear analysis of the fuel configuration options, the fuel enrichment, the tritium production, reactivity coefficients, decay heat and the design of the shield to protect the superconducting magnets from radiation damage and nuclear heating are described in section IV. The nuclear fuel cycle analysis and the transmutation performance are presented in Section V. The plasma performance, magnet and divertor systems, and the tritium production requirements of the tokamak D-T fusion neutron source are discussed in Section VI. Thermal analyses of the nominal core operation for various options for the fuel element configuration, for the depressurization loss-of-coolant-accident, for the tritium production elements, and for the divertor of the fusion neutron source, along with a discussion of the secondary system and electrical power performance are presented in section VII.

## **II DESIGN OVERVIEW**

### **II.A Configuration and Dimensions**

The reactor concept is designated the Gas Cooled Fast Transmutation Reactor-2 (GCFTR-2). This reactor is a sub-critical, fast, helium cooled reactor using coated TRU fuel particles embedded in SiC matrix pins. A 3-D depiction of the reactor and its tokamak fusion neutron source is shown in Fig. 1. The annular reactor surrounds the fusion neutron source on the outboard side.

The detailed dimensions are shown in Fig. 2. The inner radius of the reactor core is 485 cm, the core width is 112 cm (100 cm fuel region) and the core height is 300 cm. The tokamak fusion neutron annular plasma source is on the inboard side of the reactor, with a width of 216 cm and a height of 367 cm. As indicated in Fig. 1 but not shown in Fig. 2, a divertor is located on the bottom inboard side of the plasma chamber. The plasma chamber and divertor are scaled down from the ITER (International Tokamak Experimental Reactor<sup>6</sup>) design. A 3.5 cm thick first wall of the plasma chamber separates the core and plasma regions. Both the plasma and the reactor core are surrounded by a blanket-shield which is 77 cm thick on the inboard side and 79.5 cm thick on the outboard side, which in turn is surrounded by a 6 cm thick ferritic steel vacuum vessel. This entire annular configuration--reactor, plasma, blanket, shield, vacuum vessel--is contained within a ring of 16 “D-shaped” superconducting toroidal field coils, each of radial thickness 43 cm. The vacuum vessel abuts the toroidal field coils on the inboard side. Just inside the toroidal field magnets is the central solenoidal magnet of thickness 70 cm. The remaining “flux core” space inside the central solenoid has a radius of 66 cm.

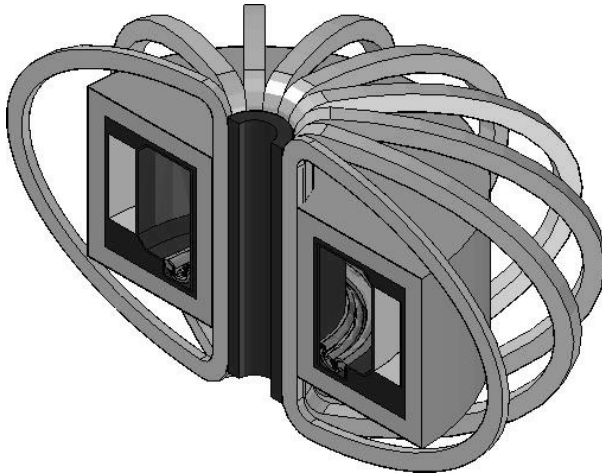


**Figure 1** 3-D depiction of the GCFTR-2

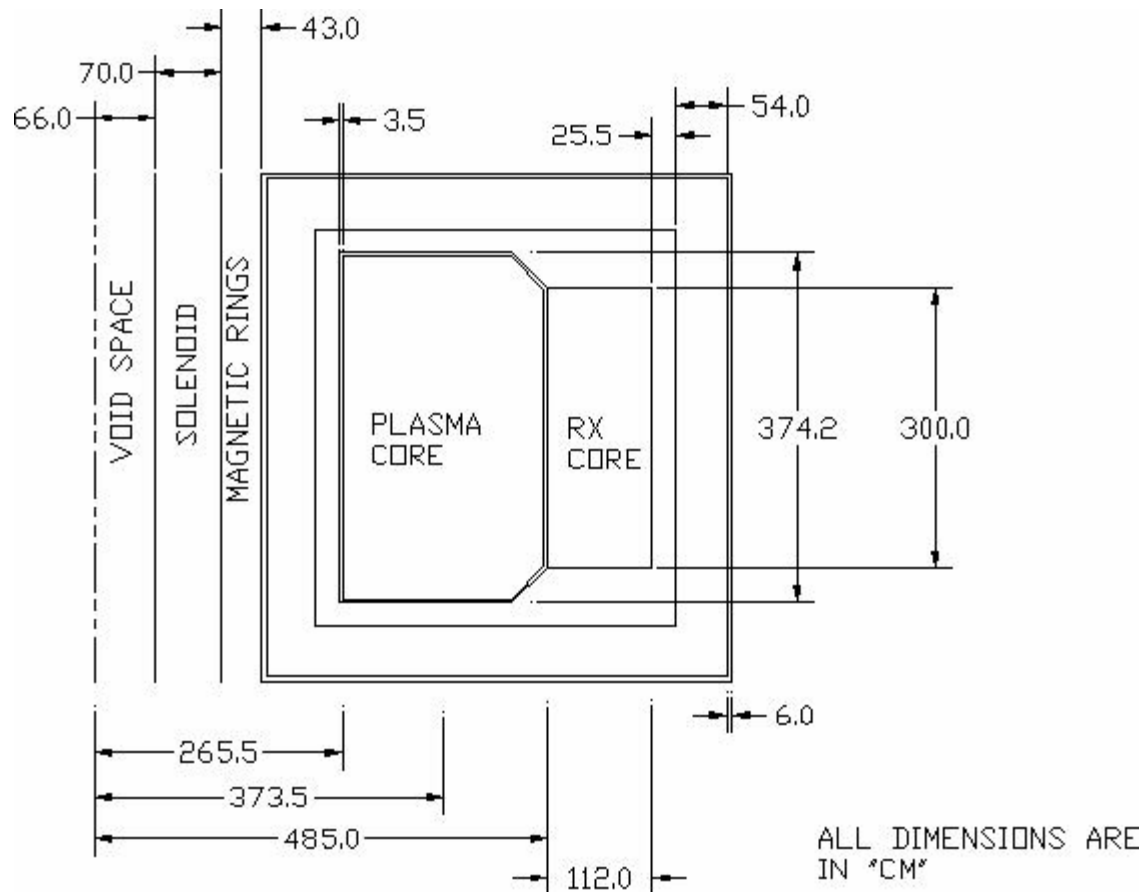
## II.B Major Parameters and Materials

Table 1 gives the major parameters and materials used in the GCFTR-2. The parameters and materials were designed for a TRISO fuel particle that has a TRU kernel that is surrounded by SiC, C and ZrC layers, which are embedded in a SiC matrix.

**Table 1.** Major Parameters and Materials of the GCFTR-2

Parameters and Materials	Values
<b>Reactor Core</b>	
Annular dimensions	$R_{in} = 4.85 \text{ m}$ , $R_{out} = 5.97 \text{ m}$ , $H = 3 \text{ m}$
Fuel/He/structure v/o	60/30/10
Fuel element	TRISO particles in SiC matrix, pins $d = 1.34 \text{ cm}$
TRU coated particle diameter	$660 \text{ }\mu\text{m}$
TRU-oxide fuel enrichment	62%
TRU fuel mass	74 MT
Maximum $k_{eff}$	0.95
He mass flow , He temperature	$M = 2870 \text{ kg/s}$ , $T_{He}^{in}/T_{He}^{out} = 280/494 \text{ }^{\circ}\text{C}$

Power density, Maximum $T_{\text{fuel}}$	$q''' = 42.2 \text{ MW/m}^3$ , $T_{\text{fuel}}^{\text{max}} = 582 \text{ }^{\circ}\text{C}$
Clad/structural materials	Zircaloy-4/HT-9
Fission Power	3000 MW <sub>th</sub>
<b>Blanket-Shield</b>	
Shield Materials	HT-9, He, B <sub>4</sub> C, HfC, Ir, WC, Cd, Pb, Xe
Tritium Breeder	Li <sub>2</sub> O
Inboard/Outboard Thickness	77/79.5 cm
Tritium Breeding Ratio	1.1
<b>Plasma</b>	
Plasma current	8.3 MA
Fusion power/neutron source rate	50 MW/1.8e19 s <sup>-1</sup> to 180 MW/6.5e19 s <sup>-1</sup>
Fusion gain ( $Q_p = P_{\text{fus}}/P_{\text{plasma heating}}$ )	180 MW <sub>th</sub> /58 MW <sub>th</sub> = 3.2
<b>Superconducting Magnets</b>	
Field CS, TFC, TF on center of plasma	12.4 T, 11.8 T, 5.7 T
<b>Divertor</b>	
Materials	W tiles on CuCrZr, He cooled
Heat flux	≤ 2.0 MW/m <sup>2</sup>
<b>First Wall</b>	
Materials	Be on HT-9, He cooled
Neutron wall load (14 MeV)	≤ 0.6 MW/m <sup>2</sup>
Heat flux	≤ 0.23 MW/m <sup>2</sup>



**Figure 2** GCFTR-2 radial dimensions

## II.C Performance

The transmutation and electrical performance of the GCFTR-2 are summarized in Table 2.

**Table 2: Transmutation & Electrical Performance of GCFTR-2**

Parameter	Value
TRU burnup objective	$\geq 90\%$ FIMA
TRU transmutation rate	1100 kg/FPY
SNF transmutation rate	99.3 tonne/FPY
LWR support ratio	3 1GW LWRs per GCFTR
Fission thermal power	3000 MWth
Gross electrical power	1020 MWe
Net electrical power	700 MWe
Electrical power amplification, $Q_e$	3.2

## II.D Radiation Damage and Component Lifetime

Component lifetime against radiation damage is an important consideration. In the reactor core, the lifetime of the TRISO fuel particles is critical to achievement of the deep-burn objective of  $\geq 90\%$  FIMA, which corresponds to a fast ( $> 0.1$  MeV) neutron fluence of  $6.5 \times 10^{23}$  n/cm<sup>2</sup> in the GCFTR-2. Unfortunately, there is little data for TRISO particles at deep burnup. The Peachbottom Reactor irradiated TRISO particles with a fast fluence of  $1.3 \times 10^{21}$  n/cm<sup>2</sup> at temperatures 800-1350°C, with a failure rate of  $1.4 \times 10^{-6}$  (Ref. 7). More recent results from development programs in the US and Germany have achieved burnups as large as 80% FIMA and fast neutron fluences as large as  $1.2 \times 10^{22}$  n/cm<sup>2</sup> with failure rates of  $10^{-4}$  to  $10^{-6}$  for the higher FIMA US tests and  $10^{-7}$  to  $10^{-9}$  for the order 10% FIMA German tests<sup>8</sup>. Achievement of the fluence lifetimes required for a deep burn transmutation reactor like GCFTR-2 is a major challenge for fuel development.

The fuel cladding and fuel assembly structure lifetimes against radiation damage are also important considerations. The minimal requirement for the zircaloy clad is to survive the 5-batch residence time of 8.1 years, which corresponds to a fast neutron fluence of  $5.1 \times 10^{22}$  n/cm<sup>2</sup>. We have been unable to find data on zircaloy radiation damage lifetimes, but such must exist. Lifetime of the ferritic steel structure can be estimated from the values of 80-150 dpa quoted for HT-9<sup>9</sup>, which corresponds to  $1.5$ - $3.0 \times 10^{23}$  n/cm<sup>2</sup> fast neutron fluence. For 40 years of operation at 75% availability, the accumulated fast neutron fluence in the core would be  $4.0 \times 10^{23}$  n/cm<sup>2</sup>, indicating that 1-2 replacements of the fuel assembly structure would be necessary.

The plasma chamber “first wall”, which consists of 3 cm of ferritic steel, would receive a fast neutron fluence of  $7.5 \times 10^{23}$  n/cm<sup>2</sup> over 30 effective full power years (EFPY) of operation. Using the same estimate for the radiation damage lifetime of ferritic steel as above, this would require 2-4 first wall replacements.

The shield was designed to protect the superconducting magnets from radiation damage failure over the 30 EFPY lifetime.

The ITER divertor<sup>6</sup>, after which the GCFTR-2 divertor is modeled, is expected to require replacement 8 times during ITER lifetime because of plasma erosion of the surface. The plasma flux to the divertor in ITER is a few times greater than in GCFTR-2, but the GCFTR-2 lifetime is several times longer than that of ITER, so that tens of divertor replacements might be anticipated for GCFTR-2.

The radiation damage and lifetime estimates are summarized in Table 3.

**Table 3. Component Radiation Damage Lifetimes**

Component	GCFTR-2 fast neutron fluence (n/cm <sup>2</sup> >0.1MeV)	LIMIT fast neutron fluence (n/cm <sup>2</sup> >0.1MeV)	REPLACEMENT OVER 30 EFPY CORE LIFE
<i>Reactor Core</i>			
Clad over 5-batch burn	$5.1 \times 10^{22}$	?	After each 5-batch residence?

Structure over 30 EFPY	$4.0 \times 10^{23}$	$1.5-3.0 \times 10^{23}$ <sup>a</sup>	1-2 replacements
TRISO Fuel particle			
@ 23% FIMA (5-batches)	$1.1 \times 10^{23}$	?	
@ 90% FIMA	$6.5 \times 10^{23}$	?	Lifetime component goal
<i>Fusion Neutron Source</i>			
TFC Nb <sub>3</sub> Sn 30 EFPY	$3.6 \times 10^{18}$	$1 \times 10^{19}$ <sup>b</sup>	Lifetime component goal
TFC insulation 30EFPY	$4.7 \times 10^7$ rad	$10^9-10^{10}$ rad <sup>b</sup>	Lifetime component goal
First-wall 30EFPY	$7.5 \times 10^{23}$	$1.5-3.0 \times 10^{23}$ <sup>a</sup>	2-4 replacements
Divertor		Plasma erosion	10's of replacements

<sup>a</sup> Ref. 9, <sup>b</sup> Ref. 10

### III. FUEL SYSTEM

#### III A. Spent Nuclear Fuel Reprocessing:

It is necessary to know the composition of the transuranic fuel that will be available from SNF in order to design the GCFTR-2, thus it is necessary to specify the initial SNF composition and the SNF reprocessing system. The solvent extraction system used is the four part partitioning process using the DIDPA and TBP solvents as designed by M. Kubota, et al. at JAERI<sup>11</sup>. A process that would utilize UREX, TRUEX and DIAMEX was also considered; however, for the simplicity of system design and superior separation factors, the DIDPA process was chosen despite a tendency for quicker solvent degradation as opposed to the other possible solvents<sup>12-15</sup>.

The four part process will separate the Np and Pu, U, Am and Cm, and lanthanides into four separate solutions that can be recombined into any desired combination as dictated by the thermal and reactor physics aspects of the core. There will be a small amount of residual uranium in the system due to the imperfection of process, but not nearly enough to affect the kernel. The separation efficiencies for the DIDPA process are shown in Table 4.

**Table 4: Separation properties of four part partitioning process<sup>11</sup>**

Elements	Target Recovery (%)	Separation Efficiency (%)	Estimated Recovery (%)
Np	99.5	>99.95	99.85
Pu	99.9	>99.99	99.85
Cm	99.99	>99.99	99.97
Am	99.9	>99.99	99.97

Since the efficiencies are so high, the amount of lanthanide poisons present in the minor actinide stream is low enough to that there will be little to no effect on the cross section of the fuel utilization factor. With the desired elements separated, the uranium stream can divert back into LWR fuel processing since much of it is still enriched and useful, and the lanthanides and fission products will be sent to a waste vitrification process and then to repository<sup>16</sup>. The remaining isotopes of Np, Pu, Am, and Cm will be separated from the aqueous streams and then combined, oxidized, and sent to the TRISO kernel manufacturing stage of the fuel cycle. The final number densities are shown in Table 5.

#### III B. Coated Fuel Particles

The two types of fuel particles that were considered for the design were the TRISO (tri-material isotropic) and the BISO (bi-material isotropic). The TRISO fuel particle is composed of a TRU kernel, a buffer layer, and three structural layers which provide containment for the fuel and its fission products. The BISO differs from the TRISO particle by having one-less structural layer. Due to having one less layer, the BISO particle is a smaller particle than the TRISO. From a fuel point-of-view, the BISO particle would be a good choice for use in the GCFTR-2 if a zirconium-based matrix material was used; however, the TRISO was chosen over the BISO since the TRISO/SiC-matrix had more advantageous



reactor physics properties and a more resilient structure for longer-term burn up. A representative TRISO particle is shown below.

**Table 5: Number densities of TRU<sup>17</sup>**

Isotope	Number density (10 <sup>24</sup> atoms/cm <sup>3</sup> )
Np 237	1.06063E-03
Pu 238	3.03036E-04
Pu 239	1.31141E-02
Pu 240	5.15161E-03
Pu 241	9.35231E-04
Pu 242	1.12332E-03
Pu 244	3.80885E-08
Am 241	2.21530E-03
Am 242M	1.60400E-06
Am 243	2.45041E-04
Cm 242	4.20593E-09
Cm 243	4.24773E-07
Cm 244	2.75867E-05
Cm 245	2.97289E-06
Cm 246	2.35114E-07
Cm 247	2.37204E-09

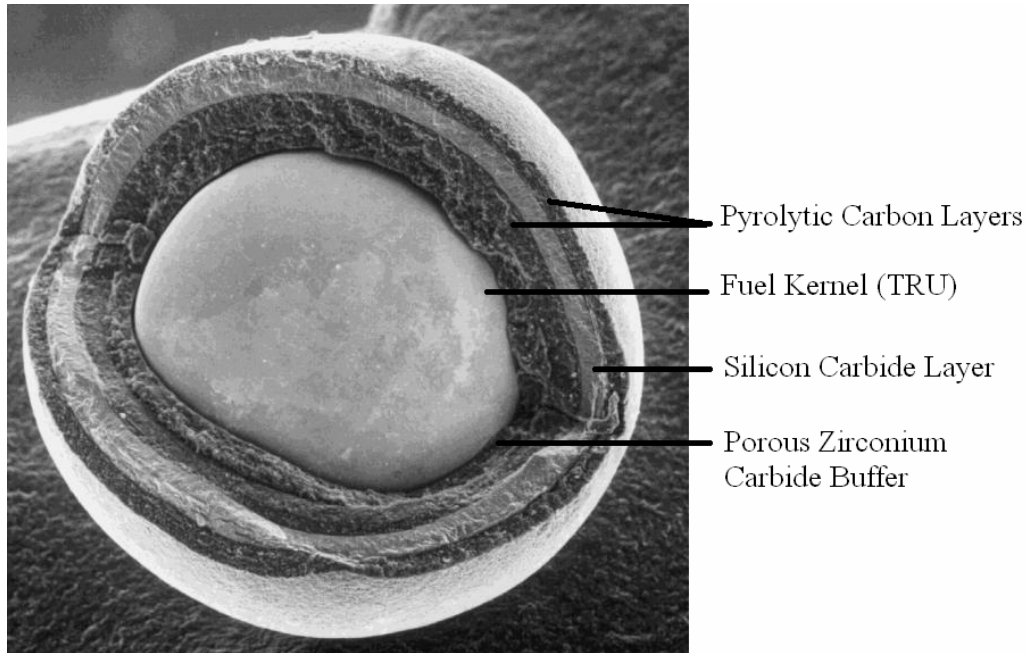


**Figure 3: Representative TRISO Particle<sup>18</sup>**

The first of the three structural layers of the TRISO particle is the inner pyrolytic carbon layer (IPyC). This layer is essential, because during the coating processes of the TRISO chlorine is used, and this layer protects the kernel from exposure to chlorine. The next layer is composed of SiC. When the TRISO undergoes irradiation, the kernel and buffer layers will expand outwards, and this layer will contract, which balances the inner and outer pressures. The last layer is the outer pyrolytic carbon layer (OPyC). This layer protects the SiC from interacting with the outside materials (cladding, matrix, etc.)

The TRISO particle is used in the design of the GCFTR-2 since it will allow for high degrees of burn-up as well as aiding in the disposal process of spent fuel.

The next area of concern is the form of the TRU fuel kernel. Options include oxide, carbide, and oxy-carbide kernels. Each choice was compared and pros and cons were weighed. The oxide kernel is advantageous since it has low volatility losses of americium, and producing oxide kernels is a well-known process. The two largest problems with oxide kernels are kernel migration (amoeba effect) and pressure buildup from carbon monoxide gas. The carbide kernel does not have any unfavorable pressure buildups or thermal migration issues. However, it has other severe problems, namely, volatility with americium during fabrication and an unfavorable reaction with SiC (the first layer of the particle). The benefits of the oxy-carbide kernel are similar to the benefits of each the oxide and carbide kernels; however, americium volatility is still unacceptably high<sup>19</sup>. The volatility with americium is unacceptable since americium is a major constituent of the TRU composition. This leaves two choices: oxide or nitride kernels. The production of <sup>14</sup>C by neutron capture is a disadvantage of the nitride kernels, which led us to rule them out. Thus, the oxide kernel used in the previous GCFTR design<sup>5</sup> was chosen, with the recognition that its problems must be resolved. The actinide composition of the TRISO kernel is listed in Table 6.

**Table 6: TRISO Kernel Composition<sup>5</sup>**

Element	Weight Percent	Oxide Form	Melting Point (°C)
Uranium	0.43	UO <sub>2</sub>	2820
Neptunium	4.32	Np <sub>2</sub> O <sub>3</sub>	2510
Plutonium	84.91	Pu <sub>2</sub> O <sub>3</sub>	2085
Americium	10.21	Am <sub>2</sub> O <sub>3</sub>	2190
Curium	0.13	Cm <sub>2</sub> O <sub>3</sub>	2225

In order to minimize the pressure buildup of carbon monoxide in the TRISO particle, a buffer layer of ZrC was proposed<sup>20</sup>, as Zr is an “oxygen getter” since oxygen has a greater affinity towards it than towards carbon. The zirconium not only alleviates carbon monoxide buildup, but it also can aid to minimize thermal migration, as carbon monoxide creates hotspots, which lead to thermal migration of the kernel<sup>20</sup>. Furthermore, the ZrC layer acts as a buffer for the recoil of fission products and it is porous which aids in containing the fission gases. The physical properties of the materials in a TRISO particle are given in Table 7. A diagram of the TRISO particle used in the GCFTR-2 design is shown in Fig 4.

**Table 7: Physical Properties of TRISO Fuel Particle components<sup>21</sup>**

Material	Melting Point (°C)	Thermal Conductivity (W/m-°C)	Density (g/cm <sup>3</sup> )
TRU Kernel	2085	2.75	10.63
PyC	2546	3.50	1.85
ZrC Buffer	3250	20.00	1.10
SiC	3373	960.00	3.2

### III C. Fuel Configuration:

Two possible fuel element configurations were investigated: 1) a fuel pin consisting of the fuel particles embedded in a SiC matrix and clad with Zircaloy-4<sup>5</sup> seen in Figure 5; and 2) solid blocks of low-density graphite foam<sup>22</sup> (LDGF) with the fuel pellets embedded, as suggested in Ref. 23 and shown in Figure 6. The fuel pin diameter was 1.34cm with a hexagonal pitch of 1.417cm. The hexagonal fuel assembly was 36.625cm wide and 300cm tall. The dimension across flats of the hexagonal LDGF fuel block was taken as the same as the pin fuel assembly for comparison purposes.

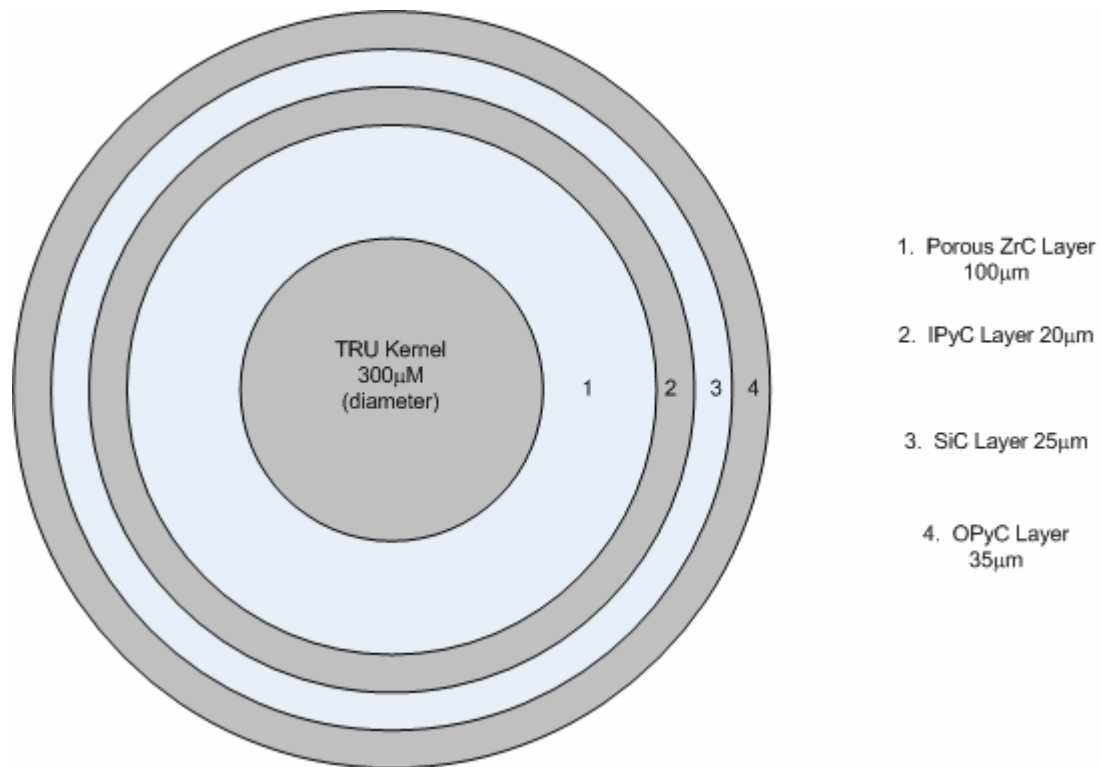


**Figure 4: TRISO Particle for GFCTR-2<sup>5</sup>**

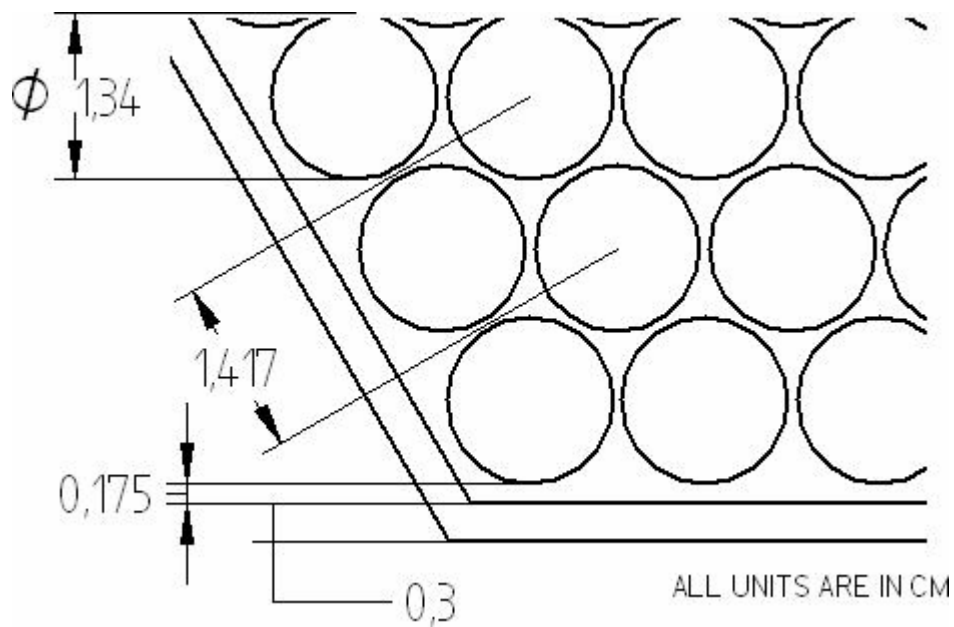


**Figure 5: Fuel Pin Assembly Cutaway**

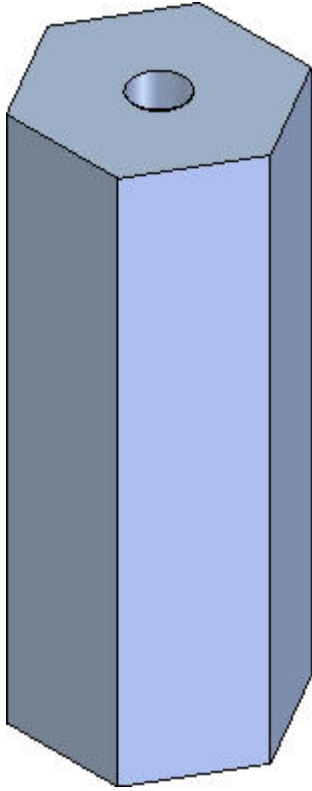


**Figure 6: LDGF Block Assembly with Central Cooling Channel**

A hexagonal fuel assembly is envisioned for the fuel pin configuration, with Zircalloy-4 clad fuel pins containing the TRISO pellets embedded in a SiC matrix material using the isothermal forced flow chemical vapor infiltration (CVI) method<sup>24</sup>. The CVI method, which is only feasible for short distances because of potential blocking of the tubes when the SiC propagates through the packed TRISO particles, requires that a short, cylindrical pellet be created, so the fuel pin will be made up of a stack of pellets about 2 inches in length. The maximum packing factor for this geometry is 62%; however, a realistic value may be more like 50-60%. The SiC matrix adds extra protection, in addition to the TRISO particle, against gaseous fission product release. Following the creation of the pellets, the Zircalloy-4 cladding will then be filled with pellets and hermetically sealed as yet another barrier to gaseous fission product release.

The other design considered was a LDGF block with embedded TRISO particles. The block resembles a fuel assembly of an HTGR, with a central coolant channel. The physical properties of LDGF and SiC are compared in Table 8. The low number density of the LDGF was initially viewed as an advantage in that it would not soften the fission neutron spectrum as much as the higher density of SiC; however this turned out not to be an unmitigated advantage because of the larger material damage effect of faster neutrons.

**Table 8: Physical Properties of Fuel Materials<sup>25,26</sup>**

Property	LDGF	SiC
Density (g/cc)	.25 – .65	3.1
Thermal Conductivity (W/m <sup>2</sup> K )	~ .3 – 175	120
Thermal Diffusivity (cm <sup>2</sup> /s)	.01 – 4.53	1.6
Coef. Thermal Expansion (/°K)	~ 0	4
Tensile Strength (MPa)	.7 – 1.6	2700
Compressive Strength (MPa)	1 – 3.5	3900
Compressive Modulus (GPa)	.144	1.05

The thermal performance of the SiC fuel pins and LDGF fuel blocks were calculated, as described in Section VII. Under nominal operating conditions there is little difference between the two

fuel options. The maximum temperature reached by the LDGF fuel block in a LOCA is about 2975 K, comparable to the value for the SiC fuel pins. This temperature exceeds the melting point of TRU-oxides (2308 °K) and of the zircaloy clad on the fuel pins (2118 °K). At these temperatures, the fission gas pressure buildup within the TRISO particles themselves may cause the particles to fail, as will be discussed in section III E. So there is little difference in the thermal performance of the SiC fuel pins and the LDGF fuel blocks.

However, there are two major other issues with the LDGF: 1) the relatively brittle nature of the material raises the question of the inability of the lower portion of the fuel assembly to support the weight of the upper portion<sup>25</sup>, which could necessitate extra structural material for support; and 2) the LDGF fabrication process is based on the graphitization process, in which the foam is heated twice to extremely high temperatures nearing 3000 °K<sup>22</sup>, which exceeds the melting point of the TRU kernel in the TRISO particle. There is also a lack of long-term durability data for the LDGF. For these reasons, the TRISO/SiC fuel pin clad with zircaloy-4 was chosen as the reference fuel configuration.

#### **III D. Fuel Manufacturing:**

The Sol-Gel process<sup>8,15,27,28</sup> would be used to manufacture the actinide fuel kernels. The process begins by preparing the sol, which includes the TRU's to be transmuted, and placing it into the device designed to form uniform droplets of fuel. The droplets are formed by forcing the solution into a hypodermic needle through an interchangeable nozzle (see figure 6). Once the droplets are formed, the droplets would be formed into a wet 'gel'. Gelation is a fast reaction since it takes place by the action of ammonia on sols, which are stabilized by hydrogen ion adsorption<sup>15</sup>. During the gelation phase, the droplets form a stabilizing barrier that surrounds the droplet. Once gelation is complete, the droplets are washed with water, in order to remove the ammonium nitrate. Once the washing is completed, the fuel kernels would then be dried using super-heated steam. This process takes about 10 minutes and occurs at 250°C. Super-heated steam is used since it has been found that the relatively dense, water-washed gel kernels can be dried without cracking if the drying takes place in a wet atmosphere<sup>15</sup>. After the drying phase, the sintering begins. The droplets are sintered with a prescribed temperature program and reduced until the kernels are ready for layering. The fuel kernels are heated to 1300°C for a duration of 3 hours. The complete process is displayed in Figure 7.

Following the sol-gel process for forming the fuel kernel, the fuel particle will be constructed. To form the TRISO particle that is needed for the GCFTR-2, a process known as chemical vapor infiltration or chemical vapor deposition is used. Chemical vapor infiltration (CVI) adds the coatings to the fuel kernel. These layers include the porous zirconium carbide (ZrC) buffer, the inner dense pyrolytic carbon (IPyC), silicon carbide (SiC), and the outer dense pyrolytic carbon layer (OPyC). Chemical Vapor Infiltration uses a gas stream that reacts on the surfaces of a porous body to deposit matrix material. By using this method, high temperature phases can be produced at temperatures below their melting points<sup>27</sup>. The ZrC coating will be formed based on the in-situ generation of zirconium halide vapor, hydrocarbon and hydrogen. Among the processes that have been developed, the bromide process is the most convenient. This involves the bromine, which is liquid at room temperature, to be reacted to generate ZrBr<sub>4</sub> vapor, which was then mixed with the other coating gases, CH<sub>4</sub> and H<sub>2</sub>. This deposited the ZrC layer onto the particle. The fabrication process by CVI of a stoichiometric ZrC coating layer has been established based on the in-situ generation of zirconium halide vapor<sup>28</sup>. Following the ZrC buffer layer was the IPyC layer, which was formed by depositing a mixture of acetylene, propylene, and argon at 1230°C. Following the IPyC coating is the SiC coating. The SiC layer is deposited using CVI using a mixture of hydrogen and methyltrichlorosilane at 1650°C<sup>8</sup>. The remaining layer to be coated onto the particle is the OPyC layer, which uses CVI as well.

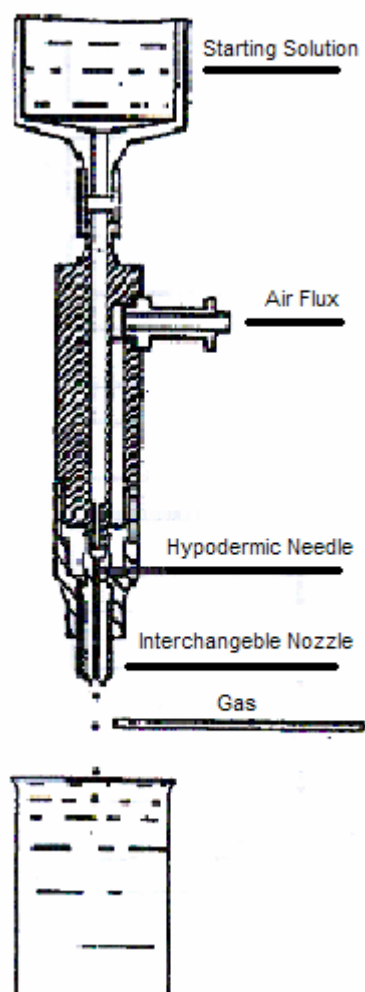


Figure 7: Droplet Formation<sup>15</sup>

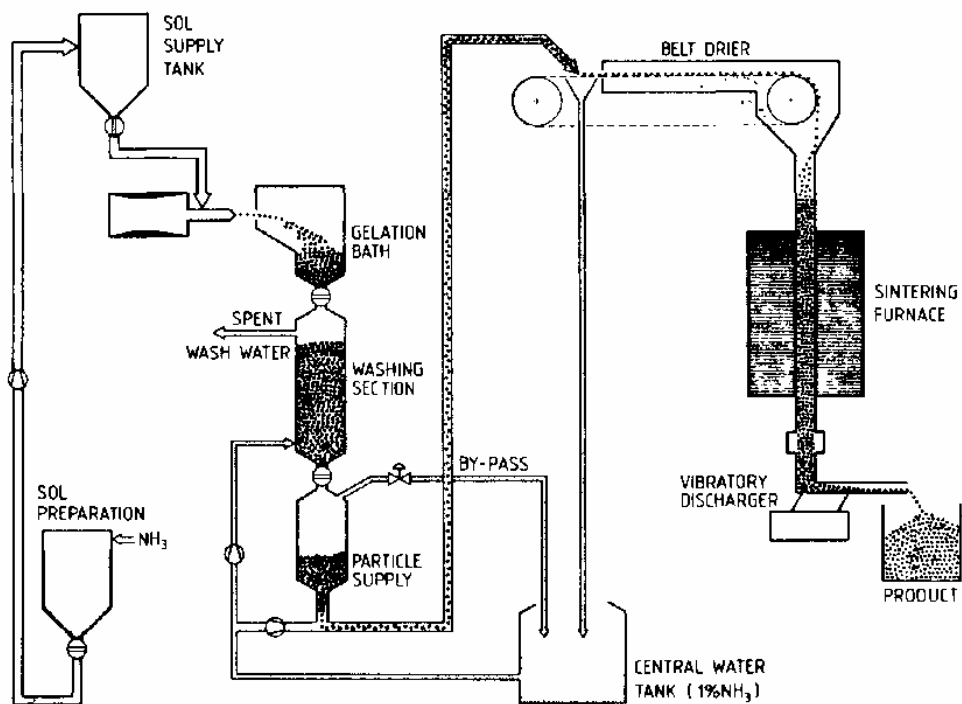
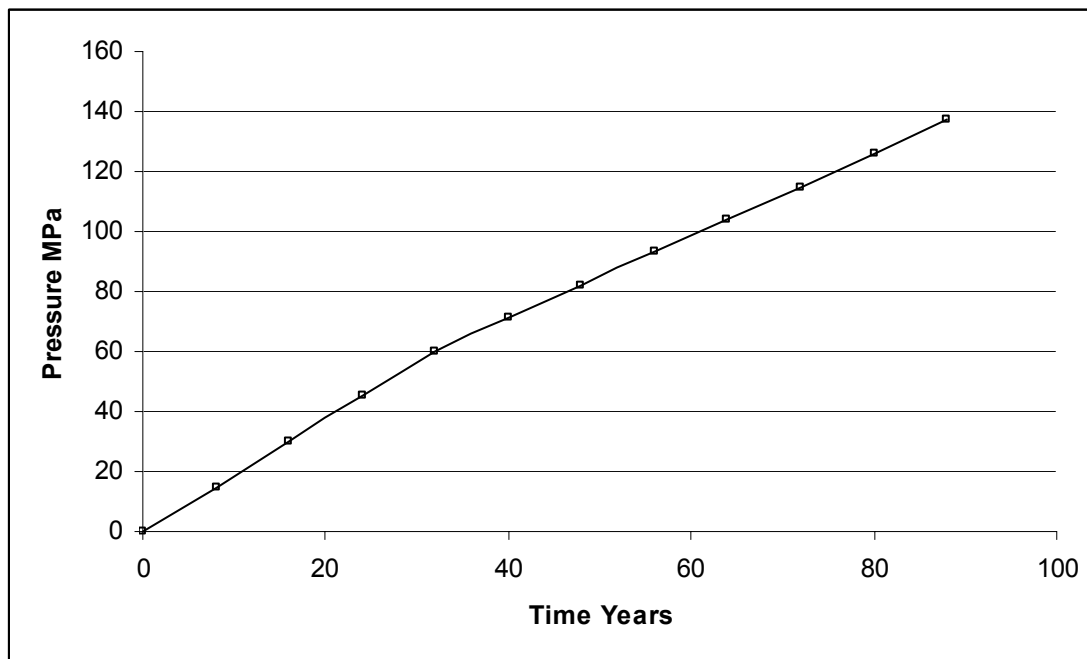


Figure 8: Equipment Flow Sheet<sup>15</sup>

### III.E TRISO Particle Lifetime

The fission gases present in the fuel play an important role in the process of degradation of fuel raised to high temperature. During this operation, global swelling of fuel is produced by the enclosed gases and the internal over-pressure due to inter granular gas bubbles. This leads to splitting of fuel along grain boundaries<sup>29,30</sup>.

The ORIGEN code<sup>31</sup> was run for deep burn up to 90 % burnup at a nominal centerline temperature of 535 ° C. Assuming 50 % porosity in the buffer layer of 100  $\mu\text{m}$ <sup>5,26</sup>, the pressure buildup shown in Fig 9 was calculated.



**Figure 9: Gas Pressure Buildup in TRISO Particle at Nominal Operating Temperature of 535°C**

The main contribution to this build up is from He, Kr, I, Xe and Br. The maximum pressure that the fission gases will reach at the nominal operating temperature is about 150 MPa, which is much less than the compressive yield strength of 345 MPa for  $\text{SiC}$ <sup>5</sup>. Hence, it can be inferred that the fuel particle will retain its integrity (radiation damage effects aside) at the nominal operating temperature during the 90 % burnup period. The ratio of 345 MPa to the nominal pressure shown in Fig. 9 times 535 °C provides an estimate of the maximum fuel temperature that could be withstood under accident conditions without failure of the TRISO fuel particles.

### III.F Waste Storage

Most of the waste that will be produced after the deep burnup can be handled with the shielding provided by the waste package. It will be contact handled, which means that the waste would not require remote handling, since alpha particles and beta particles would not penetrate the walls of the package. However, some of the containers with traces of Gamma generators (e.g. Cs) will have to be remotely handled<sup>32,33</sup>.

The waste could be vitrified by a Slurry Fed Ceramic Melter System. The waste would be mixed with molten glass and discharged from canisters where it solidifies. The reason glass is chosen is that it has high solubility for the nuclides found in HLW, shows resistance to radiation damage, requires only moderate temperature borosilicate glass based on the properties given in Table 10.

Property	Value
Thermal conductivity at 100 C	.55 BTU/h.ft.F
Heat capacity (100 C)	0.22 cal/g C
Fractional thermal expansion	1.22 E-5/C
Young's Modulus	9.0 E9 psi

Tensile strength	9.0 E3 psi
Compressive strength	1.0 E5 psi
Poisson ratio	0.2
Density (100 C)	2.5-3.0 g/cm3

**Table 9: Physical properties of borosilicate glass<sup>34</sup>**

Several materials are available for the canister in which vitrified waste is to be placed. They are type 304L stainless steel, plated carbon steel, titanium, and recycled contaminated steel. Overall, type 304L is the most promising material based on the experiments performed on materials mentioned above. Type 304L is an extra low carbon and high Chromium content alloy. The .03% maximum carbon content eliminates carbide precipitation due to welding. Consequently, the alloy can be used in the “as welded” condition even in severe corrosive conditions<sup>35</sup>.

The typical size of a canister will be 3.0 m high, 0.60 m outer diameter and a wall thickness of 9.53 mm. Each canister can hold ~1700 kg of glass, of which ~45kg will be radionuclides. The canister can withstand decay heat of ~ 700 W ( well above the decay heat calculated with the ORIGEN code ~ 20 W in 30 years), and the maximum activity of ~300 kCi would produce a radiation level of ~550rem/h on contact. The canister would normally be expected to corrode in 300 years, but in this case that is unlikely since there will not be enough heat to generate steam to cause corrosion<sup>34</sup>.

## **IV. NUCLEAR DESIGN**

### **IV.A. Fuel configuration**

The goal of the GCFTR-2 is to achieve deep burn of the actinide fuel with little or no reprocessing. In order to realize this goal a fast neutron spectrum is desired in order to make use of the high fission-to-capture ratio present with most actinides. There is, however, an inherent trade-off since a harder neutron spectrum increases the probability of radiation damage to the non-fuel structure of the core. It is necessary to choose a fuel assembly design which maximizes the rate of actinide fission with respect to the rate of radiation damage.

As described in Section III, the TRISO and BISO coated fuel particles are being considered for the GCFTR-2 fuel. These particles would be embedded in a matrix material such as SiC or zircalloy, respectively. A recently developed low-density graphite foam was also considered as the matrix material. In addition to having excellent thermal conductivity properties, the graphite foam has a very low density which will produce a harder neutron spectrum.

The four fuel configurations under consideration are (1) fuel pins of TRISO particles embedded in a SiC matrix, (2) fuel pins of BISO particles embedded in a zircalloy matrix, (3) TRISO particles embedded in graphite foam blocks and (4) BISO particles embedded in graphite foam blocks. Configurations 1 and 2 consist of zircalloy clad fuel pins with helium coolant flowing around them, as depicted in Fig. 5. Configurations 3 and 4 are fuel block designs which have helium coolant channels running vertically throughout the blocks, as depicted in Fig. 6. The fuel will occupy approximately 60% of the core volume, leaving ~30% coolant volume and ~10% structural volume.

The eigenvalue and core-averaged flux for each of these fuel configurations was computed using the radiation transport code EVENT<sup>37</sup>. The entire reactor was modeled using 2D r-z geometry with 34-group cross-sections generated by MC-2<sup>38</sup>. A P<sub>5</sub> angular approximation was used to calculate the neutron flux. Each region of the reactor was homogenized by a simple uniform smearing the volume-weighted material composition. It was assumed that the fusion neutron source is isotropic and uniform inside the plasma chamber. Therefore, the fusion source was modeled by placing the isotropic volumetric source in the first wall. Representative neutron spectra in the core are shown in Fig. 10.



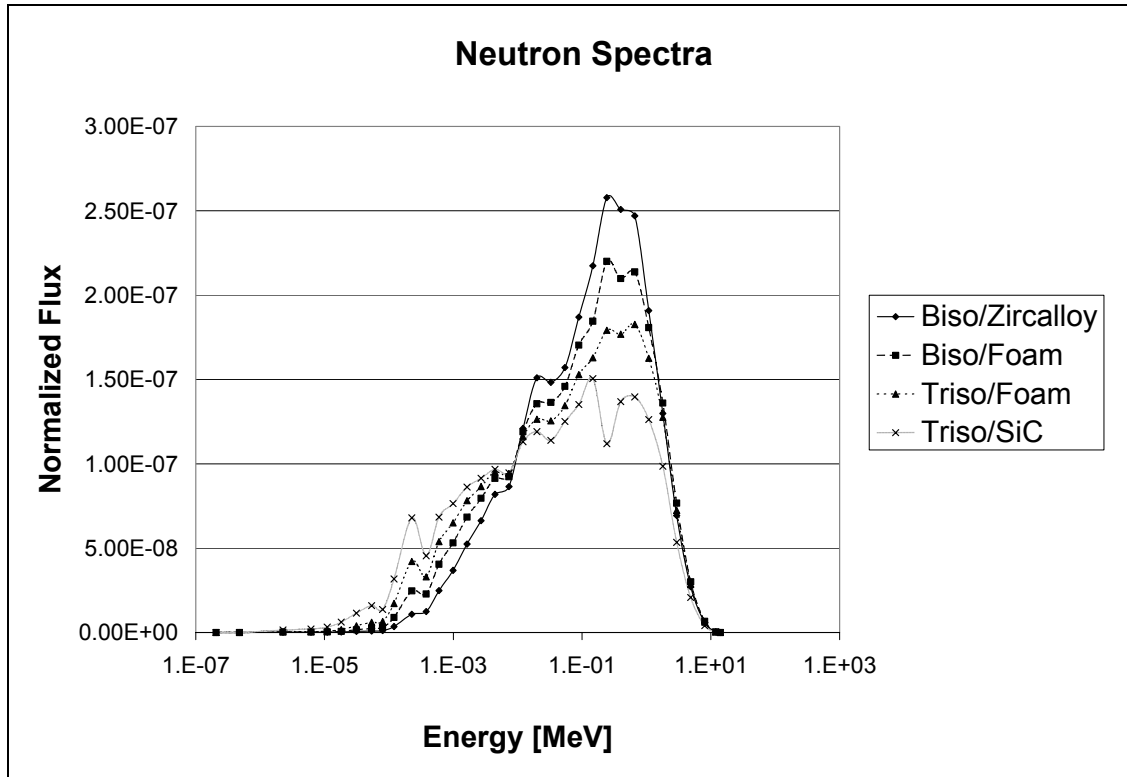


**Figure 10: Neutron spectra with different fuel configurations.**

From a neutronic standpoint, the basis of comparison between the assembly types is the neutron utilization index (NUI)<sup>5</sup> defined as the total fission rate divided by the neutron flux with energy greater than 100 keV. The assembly with the highest NUI should provide the most fissions per fast neutron, i.e. the most actinide burn per neutron capable of inducing structural damage. The NUI for each assembly is shown in Table 8 along with spectral parameters. The configuration with the highest NUI is the assembly with pins of TRISO particles embedded in SiC. For this and other reasons discussed in section III, this fuel configuration was selected for the GCFTR-2 and considered exclusively in the design analysis discussed hereafter.

**TABLE 10: Fuel Configuration Comparison**

	TRISO/SiC	BISO/Zircalloy	TRISO/LDGF	BISO/LDGF
$k_{eff}$	0.950	0.938	0.950	0.950
Fast neutrons*	45.22%	62.35%	53.51%	58.18%
Intermediate neutrons	54.71%	37.65%	46.48%	41.80%
Thermal neutrons	0.07%	0.01%	0.02%	0.01%
NUI ( $\times 10^{-6}$ )	12.83	4.01	7.67	5.43

\*Fast: 20 MeV ~ 100 keV

Intermediate: 100 keV ~ 6 eV

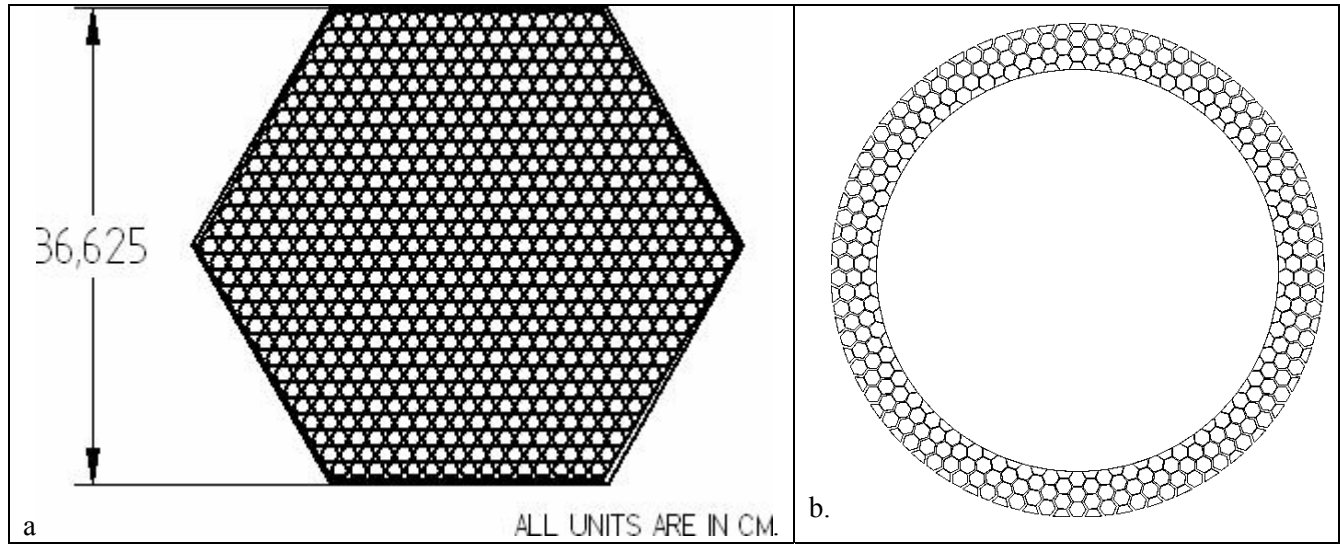
Thermal: < 6 eV

#### IV.B Assembly Design and Fuel Enrichment

The TRISO/SiC pins have roughly the same size as PWR pins, with an outer pin diameter of 1.34 cm. The pins are clad with Zircaloy-4 and tightly arranged in hexagonal assemblies with a pin pitch of 1.417 cm. The hexagonal assemblies are placed immediately outside the first wall, completely circumscribing the plasma chamber as shown in Figure 11.

**Table11: Fuel Pin & Assembly Parameters**

Flat to Flat distance	36.625 cm
Pin diameter w/clad	1.34 cm
Clad thickness	0.06 cm
Pin pitch	1.417 cm
Assembly wall thickness	0.3 cm
Pins/assembly	631
Total pin count for core	185000

**Figure 11: Fuel Assemblies: a) single fuel assembly and b) core layout.**

Since the isotopic composition of the TRU in the fuel particle kernels does not include uranium, the conventional definition of fuel enrichment does not apply to the GCFTR. Here enrichment refers to the volume of the coated fuel particles divided by the total volume of the fuel, which includes the fuel particles and the matrix material. In other words, the fuel enrichment is equivalent to the packing fraction of the TRISO particles in the matrix material. Due to the low delayed neutron fraction of Pu-239 and some of the other actinides, the GCFTR-2 will operate at sub-criticality with  $k_{\text{eff}} \leq 0.95$  to enhance the reactivity margin to prompt critical. For the core shown in Fig. 11 with the TRISO/SiC fuel pin, a fuel/coolant/structure v/o of 60/30/10 and a height of 3 m,  $k_{\text{eff}} \approx 0.95$  requires a core fuel enrichment of 38.5%. As discussed below, a higher fuel enrichment is needed to offset the addition of  $\text{Li}_2\text{O}$  for tritium breeding (and of the zircaloy cladding which was omitted in the above calculation).

#### IV.C. Tritium production

The sub-critical GCFTR-2 is driven by a deuterium-tritium fusion neutron source. It is necessary to achieve a condition of tritium self-sufficiency, where the reactor produces enough tritium to independently sustain the fusion source. Tritium production is accomplished utilizing the  $(n, \alpha)$  neutron capture reaction in lithium. The condition for tritium self-sufficiency can be characterized in terms of the tritium breeding ratio (TBR), defined as follows:

$$TBR = \frac{\text{\# of tritium produced per unit time}}{\text{\# of fusion source neutrons per unit time}}$$

As discussed in section VI, taking into account the loss of tritium in the extraction process and the loss due to the radioactive decay, tritium self-sufficiency requires  $TBR \approx 1.1$ .

The tritium production reaction is the neutron capture reaction by lithium. A calculation was made in which 90% enriched (in  $^6\text{Li}$ )  $\text{Li}_2\text{O}$  was placed in the upper and outboard of reflector, and 30% enriched  $\text{Li}_2\text{O}$  was placed in the inboard of reflector, as indicated in Fig. 12.  $\text{Li}_2\text{O}$  was selected in order to obtain the highest lithium number density. It was found that it was also necessary to place some  $\text{Li}_2\text{O}$  inside the core in order to obtain  $\text{TBR} > 1.0$ . Figure 13 shows the reactor configuration for the calculation, and Table 12 gives the parameters used in the calculation.

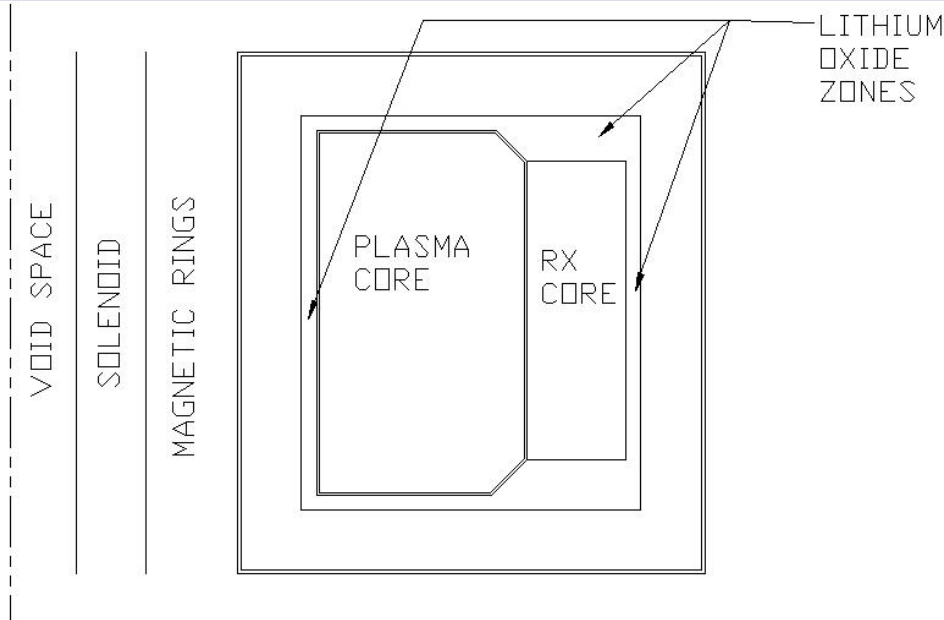


**Figure 12: Location of Lithium Oxide for Tritium Production**

**TABLE 12: Core and surrounding reflector material composition.**

Materials	Reflector without $\text{LiO}_2$	Blanket with $\text{LiO}_2$	Core
HT-9	70.0%	10.0%	5.0%
He coolant	30.0%	40.0%	30.0%
Lithium Oxide	0.0%	50.0%	0.2%
TRU/SiC Fuel Pin	0.0%	0.0%	64.3%

The TBR was calculated using EVENT in a manner identical to the core calculations described in section IV.A. Replacing 0.1-0.2 v/o of the fuel in the core with  $\text{Li}_2\text{O}$ , in addition to the  $\text{Li}_2\text{O}$  in the reflector, resulted in  $\text{TBR} = 1.06\text{-}1.23$ . In order to maintain  $k_{\text{eff}} = 0.95$  with 0.1-0.2 v/o  $\text{Li}_2\text{O}$  and the cladding in the core, the TRISO fuel enrichment must be increased to 60.0-62.5%, which is at the theoretical limit.

#### IV.D. Reactivity coefficients

Several key reactivity parameters were computed for the GCFTR-2 with the different fuel configurations under consideration. The two reactivity worths of primary concern are the coolant void reactivity and the Doppler temperature reactivity. Each reactivity value was computed by two separate EVENT calculations: one for the nominal reactor under hot operating conditions and the second for a slightly perturbed system.

The coolant void reactivity (CVR) was computed by assuming an instantaneous complete voiding of the core coolant, corresponding to the worst-case scenario. The change in reactivity in this scenario is  $\delta\rho = 4.963 \times 10^{-4}$ , which corresponds to a  $\delta k_{\text{eff}} = 0.471 \text{ mk}$  (1 mk = 0.001), for the reference TRISO/SiC pin fuel configuration, which has the lowest CVR of the four fuel configurations considered (see section IV.A). Since the helium in the GCFTR acts as a slight neutron moderator, the absence of helium causes a shift in the neutron spectrum towards higher energies, producing a slightly positive CVR.

The Doppler reactivity was calculated by assuming a sudden increase in the fuel and matrix material temperatures. Since there is not a strong presence of resonance absorbers in the fuel, Doppler

reactivities were quite low. The reference TRISO/SiC pin fuel configuration had the most negative Doppler reactivity coefficient of  $\delta\rho/\delta T_F \approx -5.56 \times 10^{-6}/^\circ\text{C}$ , or  $\delta k_{\text{eff}} = -0.00527$  mk per unit increase in fuel temperature.

#### IV.E. Benchmark

The EVENT calculation used for the above analysis was compared with S<sub>8</sub> TWODANT<sup>39</sup> calculations for benchmark purposes. The 34-group cross sections from MC-2 were used in both calculations. The core regions were modeled by volume-weighted material homogenization. Using the diffusion approximation, the EVENT calculation of  $k_{\text{eff}}$  agreed with TWODANT to within 5.0E-04.

#### IV.F. Blanket-shield design

In the design of the GCFTR-2, the primary requirements of the blanket-shield are to protect the superconducting magnets from radiation damage (maximum allowable fast [ $> 0.1$  MeV] neutron fluence  $10^{19}$  n/cm<sup>2</sup>, maximum dose to insulators  $10^9$  rads) so that they can be lifetime components and to produce tritium in lithium-containing Tritium Breeding Elements (tritium breeding ratio  $\approx 1.1$ ). Secondary requirements are to reduce the nuclear heating in the superconducting magnets and to reflect neutrons back into the reactor.

There are some additional constraints upon the blanket-shield design. The shielding material should not burn out in the 30 EFPH design lifetime of the GCFTR-2, although the Li<sub>2</sub>O will be replaced as necessary. Furthermore, there is an economic incentive to minimize the thickness of the inboard blanket-shield, hence the size of the reactor. The inboard shield, vacuum vessel, first-wall and tritium breeding elements were designed to fit into a radial dimension of 82 cm, as indicated in Fig. 2.

The blanket-shield system was modeled in 2D R-Z detailed geometry with MCNP<sup>40</sup>. The shielding calculation was performed in two stages. The fusion plasma neutron source and the slightly sub-critical reactor could not be modeled in a single calculation, so the first calculation treated the high energy neutron source into the (voided) reactor volume from the 14 MeV plasma neutron source. A fluence tally was used in a voided reactor volume to determine the neutron flux entering the space of the reactor. This fluence number was then scaled by the power at which the fusion source was to be operated. The resulting number gives an input neutron flux for the second stage of the calculation, in which the system was modeled as a criticality problem with an initial watt fission spectrum (MCNP manual<sup>41</sup> pg 99 of volume 2 chapter 3). The criticality calculation was allowed to converge and a flux resulting from the average neutron population produced in the core was then taken for all of the areas of importance. The photon source was modeled in a similar manner.

The neutron shielding materials selected for this application deviated somewhat from standard practice in order to achieve a compact configuration. The typical use of B<sub>4</sub>C as a shielding material was by and large avoided because, due to the high fast flux and leakage from the reactor, this shielding material would burn out from the n- $\alpha$  reaction if used as the only neutron absorbing material. The alternative selected was a mix of hafnium carbide (HfC) and beryllium as the main shielding materials for neutron absorption, with only a small layer of B<sub>4</sub>C on the outer edge. Carbon rich materials were chosen to thermalize the neutrons, which were then absorbed. The shield was designed to operate at 400-800 °C in the lithium-oxide containing regions in order to insure tritium recovery.

NJOY<sup>42</sup> was used to broaden the cross sections for all of the runs. NJOY correctly broadens the resonance region and self shielding cross sections for the materials point to point in energy on a reaction by reaction basis. Here the HfC relies on the resonance n- $\gamma$  reaction. Solid Li<sub>2</sub>O and helium purge gas and a layer of solid beryllium on the outside of the reactor were included for tritium production, as discussed above. At the upper energies of the fission spectrum, where most of the neutron leakage from the core occurs, beryllium has a substantial n,<sub>2</sub>n reaction. B<sub>4</sub>C is used in the outer region of the shield to thermalize and capture the neutrons that propagate to that region. Lastly, a 5 cm thick sheet of cadmium was added to capture all of the remaining thermalized neutrons.

The photon shielding was a combination of lead, tungsten and iridium. The tungsten is a good photon shield due to its high atomic number. On the outboard side of the reactor, a 15 cm sheet of lead was added to cut down the photon flux. On the inboard side, space is of an extreme premium, and Iridium was chosen to be the photon shield due to it being roughly twice the density of lead.

Tritium breeding was accomplished through a multifaceted approach. The relatively “soft” fast reactor spectrum caused by the large amount of SiC present in the core (Fig. 10) made it infeasible to

achieve the required tritium breeding ratio  $\approx 1.1$  with  $\text{Li}_2\text{O}$  located only in the blanket region, even using enrichments of 90 percent lithium-6. Therefore,  $\text{Li}_2\text{O}$  had to be added to the reactor region. As discussed above,  $\text{Li}_2\text{O}$  was added to the core at 0.2 v/o. MCNP was used to calculate the tritium production and neutron heating in the blanket and core. In addition to highly enriched (90 percent Li-6) in the outboard blanket, 30 percent Li-6 composition lithium was added in the inboard blanket of the fusion chamber in order to utilize the  $\sim 14$  MeV neutrons that were escaping inward and not contributing to the reactor neutron source. The MCNP calculation yielded  $\text{TBR} \approx 1.1$ , taking into account the lithium-oxide in the core and blanket-shield. This MCNP result, together with the more optimistic EVENT calculation of  $\text{TBR} = 1.23$  for 0.2 v/o  $\text{Li}_2\text{O}$  in the core and slightly more  $\text{Li}_2\text{O}$  in the blanket, provides confidence that tritium self-sufficiency can be achieved in the GCFTR-2 design.

The blanket-shield design described in Table 13 meets all of the requirements, as indicated in Table 14. The system fits into the space confines of the superconducting magnets while still keeping the neutron and photon fluxes well below the required levels. With an operating power of 175 MW for the fusion neutron source, the blanket-shield design can last for approximately 45 years at 80% availability. This is the point at which the  $\text{B}_4\text{C}$  burns out, after which the neutron flux to the magnets would rapidly increase.

**Table 13: Blanket-Shield Dimensions & Materials**

(REFL= Reflector, FW=First Wall, TBE = Tritium Breeding Element, SHLD= Shield, VV = Vacuum Vessel)

Designation	Thick	Outer Radius	Material										
	cm	cm	HT-9 steel	Be	Ir	$\text{Li}_2\text{O}$	HfC	$\text{B}_4\text{C}$	WC	Cd	Pb	Xe	He
			OUTBOARD										
REFL	3.5	600.5	100%	-	-	-	-	-	-	-	-	-	-
TBE	22	622.5	4 w/ specifications seen in the subtable below w/ 90% enriched Li-6										
SHLD	30	652.5	-	-	-	-	85%	-	10	-	-	5%	-
SHLD	18	670.5	-	-	-	-	-	45%	45%	-	-	10%	-
SHLD	1	671.5	-	-	-	-	-	-	-	95%	-	5%	-
SHLD	5	676.5	-	-	-	-	-	-	-	-	95%	5%	-
VV	6	682.5	100%	-	-	-	-	-	-	-	-	-	-
			INBOARD										
VV	6	185	100%	-	-	-	-	-	-	-	-	-	-
SHLD	5	190	-	-	95%	-	-	-	-	-	-	5%	-
SHLD	1	191	-	-	-	-	-	-	-	95%	-	5%	-
SHLD	10	201	-	-	-	-	-	45%	45%	-	-	10%	-
SHLD	44.5	245.5	-	-	-	-	85%	-	10	-	-	5%	-
TBE	16.5	262	3 w/ specifications seen in the subtable below w/ 30% enriched Li-6										
FW	3.5	265.5	100%	-	-	-	-	-	-	-	-	-	-
Tritium Breeding Element (TBE)													
	1		-	99%	-	-	-	-	-	-	-	1%	-
	0.5		-	-	100%	-	-	-	-	-	-	-	-
	3.5		-	-	-	95%	-	-	-	-	-	-	5%
	0.5		-	-	100%	-	-	-	-	-	-	-	-

**Table 14: Shielding Performance** (Nominal Fusion Neutron Source  
@ 180 MW=6.39E+19 n/s, Reactor  $k_{\text{eff}} = 0.95$ )

Parameter	Value	Limit	Calculated Value	Time to end of life
40-yr fast neutron fluence to superconductor at 75% availability	n/cm <sup>2</sup>	1.0E+19	3.62E+18	>>40
40-yr radiation dose to magnet Insulators at 75% availability	rad	1E+9/1E+10 <sup>a</sup>	4.67E+07	>>40
Nuclear Heating per magnet	kW		5.42E+00	
Total nuclear heating in magnets	kW		8.64E+01	
Power for cooling toroidal magnets	MW		9.76E+00	

<sup>a</sup> epoxy/ceramic

## V. NUCLEAR FUEL CYCLE

### V.A Batch operation and fuel cycle characteristics

The GCFTR fuel cycle consists of the continuous recycle of TRU fuel until >90%FIMA is achieved. A five-batch shuffling scheme with a 600-day cycle time is used. The core is initially loaded with “fresh” fuel (0%FIMA) and burned for one 600 day cycle. Fuel in the innermost region is then removed from the reactor and allowed to cool, the intermediate regions are each moved to the next inmost region of the core and the outermost region is filled with “fresh” fuel. Irradiated fuel will accumulate until after the third cycle, at which time the activity of the first batch to leave the core will have sufficiently decreased. It is then reinserted into the outermost region of the core along with other more reactive pins to compensate for the decreased reactivity due to the previous burn. If necessary, the cladding will be replaced prior to emplacement. It is assumed that the cladding will last for at least one “5-batch” pass through the reactor. The SiC matrix will be reconstituted as need be and is expected to last for at least one 5-batch pass through the reactor.

In the reference scenario, the continuous-recycle case, the TRISO particles are reprocessed after each 5-batch exposure in the reactor, their fission products extracted and sent to a HLWR, and their unburned TRU content re-fabricated into new particles. In the advanced scenario, the TRISO particles are never reprocessed during this repeated recycling nor before storage in a high level waste repository (HLWR) at  $\geq 90\%$  FIMA. This advanced scenario depends, of course, on the possibility of developing TRISO particles that can withstand radiation damage to  $\geq 90\%$  FIMA. In either case, the shuffling procedure outlined above will continue until the FIMA for a given batch has reached >90% at which time the particles will be processed for storage and placed in a HLWR.

The fuel composition in the reactor will change with time until an equilibrium is reached. The equilibrium fuel cycle in the reference scenario consists of fuel in the innermost region that is four-times burned, three-times burned for the next outermost region, out to the outermost region which is fresh fuel. This equilibrium is an approximation to the true equilibrium, which will consist of a much more diverse assortment of fuel pin burn times.

### V.B Computational Models

Fuel cycle calculations were performed with REBUS-3<sup>43</sup>, a fuel cycle depletion code. 34-group cross-sections were generated using the MCC-2<sup>38</sup> processing code, the ENDF-B/V cross-section library, and the equilibrium operating temperatures listed in Table 15. Transport calculations were performed with TWODANT<sup>39</sup>, a two-dimensional finite-difference flux distribution code, using an S6 approximation. Long-term decay characteristics of processed LWR SNF were calculated using ORIGEN-S<sup>31</sup>, a depletion and decay code, and KENOVA<sup>44</sup>, a criticality code, both of which are included in the SCALE5 package.

**Table 15: Transmutation fuel cycle analysis for 3000MW<sub>th</sub> GCFTR-2.** (The coolant temperature for a given region, where not specified, is 50°K less than the temperature of the given region.)

Temperature (K)	Region
750	Core Fuel
660	Core Coolant
700	Core Structure
600	Shield
600	Reflector
600	Magnet
600	Central Solenoid
600	First Wall
600	Vacuum Vessel

#### V.C Transmutation Performance with Reference Scenario

The detailed performance metrics for the GCFTR-2 Reference scenario are listed in Table 16. The fusion power swing over a given equilibrium cycle was well within the design limit of 180 MW. The required fuel volume fraction exceeds that possible with equally-sized TRISO particles when the packing fraction is taken into account (theoretical maximum ~64%). The 70% figure would be made more realistic if different sized particles were used.

**Table 16: 3000MW<sub>th</sub> GCFTR-2 Fuel Cycle Parameters**

PARAMETER	UNITS	
Fuel/Matrix (by volume)	n/a	70/30
Total Core TRU Volume	%	4.57
Core Coolant Volume	%	20.0
Core Fuel Volume (TRISO+matrix)	%	59.5
Core Cladding Volume	%	10.0
Core Li <sub>2</sub> O Volume	%	0.5
Cycles/Residence Time (Batches)	n/a	5
Cycle Length	Days	600
Once-Through Residence Time	Years	8.21
BOC $k_{eff}$	n/a	0.95
EOC $k_{eff}$	n/a	0.81
BOC $P_{fus}$	MW	38
EOC $P_{fus}$	MW	137
TRU BOC Load	MT	51
TRU Burned per Year	MT/FPY	1.11
TRU Burned per Cycle	MT	1.8
TRU Burned per Residence Time	MT	9.1
TRU Burn/Cycle	%	3.6
TRU Burn/Residence	%	16.8
SNF Disposed per year	MT/FPY	99.3
Average Core Flux Across Cycle	n/cm <sup>2</sup> -s	4.25E+14
Average Core (>0.11MeV) Flux	n/cm <sup>2</sup> -s	1.98E+14
Fluence/Residence Time	n/cm <sup>2</sup>	1.10E+23
Fluence (>0.11MeV)/Residence Time	n/cm <sup>2</sup>	5.14E+22
Residence at 90% Burn	Years	103
Fluence at 90% Burn	n/cm <sup>2</sup>	1.38E+24

Fluence (>0.11MeV) at 90% Burn	n/cm <sup>2</sup>	6.45E+23
Residence at 99% Burn	Years	205
Fluence at 99% Burn	n/cm <sup>2</sup>	2.75E+24
Fluence (>0.11MeV) at 99% Burn	n/cm <sup>2</sup>	1.28E+24

At a thermal power of 3000MW/FPY, the GCFTR-2 transmutes approximately 1.11MT of TRUs, which is equivalent to the TRU production rate of three 1000MWe LWRs per FPY. Hence, one GCFTR-2 can “support” 3 1000MWe LWRs. At the current rate of electricity production by nuclear power facilities in the United States (104 reactors), the national production of TRU could be offset with the deployment of a fleet of 35 GCFTRs. Additional units would allow for the depletion of TRU stockpiles contained within more than 60,000MT of SNF dispersed throughout the country. This depletion of the TRU content of LWR SNF would significantly reduce the repository requirements of a geologic repository and increase the proliferation resistance of that facility.

## VI. FUSION NEUTRON SOURCE

### VI.A Plasma Physics and Engineering Systems Analysis

Standard tokamak systems analysis methodology<sup>45</sup> was used to determine the major operational and geometric parameters in terms of the aspect ratio (major radius/minor radius) and plasma current, taking into account the various plasma physics and engineering constraints, as well as the geometric constraint on the radial build. A reference fusion neutron source was chosen with the nominal parameters for the most part well within the limits of the present plasma physics and fusion technology database, as given in Table 17. For the sake of comparison, the parameters of the planned ITER experiment<sup>6</sup>, which would serve as a proto-type of the GCFTR-2 neutron source, are also given.

**Table 17 Tokamak D-T Fusion Neutron Source Nominal Parameters**

Parameter	GCFTR-2	ITER <sup>6</sup>
Fusion power, $P_{fus}$ (MW <sub>th</sub> )	180	410
Neutron source strength (#/s)	$7.1 \times 10^{19}$	$14.4 \times 10^{19}$
Major radius, R (m)	3.72	6.2
Minor radius, a (m)	1.08	2.0
Plasma elongation, h/w	1.7	1.8
Plasma current, I (MA)	8.3	15.0
Fusion power/Plasma heating power	3.1	10
Magnetic field in plasma, $B_\phi$ (T)	5.7	5.3
Confinement factor <sup>a</sup> $H_{IPB98}(y,2)$	1.0	1.0
$\beta_N = (\text{plasma press}/\text{mag press})/(I/aB_\phi)$	$2.0^b$	1.8
Bootstrap current fraction, $f_{bs}$	0.31	
Current drive efficiency, $\gamma_{cd}$ (A/Wm <sup>2</sup> )	$0.61^c$	
14 MeV neutron wall flux, $\Gamma_n$ (MW/m <sup>2</sup> )	0.6	0.5
Heat flux to wall, $q_w$ (MW/m <sup>2</sup> )	0.23	0.15

<sup>a</sup> enhancement factor relative to present database; <sup>b</sup> present database  $\leq 2.5$

<sup>c</sup> present database  $\leq 0.45$

### VI.B. Superconducting magnet dimensions

The superconducting magnet design for the original GCFTR design<sup>5</sup> was adapted directly from the ITER design<sup>46,47</sup>. This design was based on cable-in-conduit Nb<sub>3</sub>Sn conductors operating at magnetic field strengths up to 11.8 T for the toroidal field coils (TFCs) and 13.5 T for the central solenoid (CS). After completion of the GCFTR design, it was realized that the scaling of the TFC design had allowed more space than was actually needed to contain the conductors necessary to produce the required toroidal field, and a preliminary re-examination of the magnet design indicated that the radial thickness of the



TFC could be reduced to 0.43 m. The purpose in this section is to re-examine the radial thickness determinations for the CS and TFC.

The first step in examining the radial magnet dimensions was a verification of the CS dimensions. Two limiting factors were considered. The tensile stress should be less than 430 MPa<sup>46</sup>, and the startup Volt-seconds,  $VS_{\text{start}}$ , should be above the 82.5 V-s required for inductive startup.

An approximate equation for the Central Solenoid stress is<sup>48</sup>:

$$C \cdot \frac{1}{f_{\text{structure}}} \cdot \left( \frac{B_{OH}^2}{2 \cdot \mu_0} \right) \left( \frac{R_{fc}}{\Delta_{OH}} + \frac{1}{3} \right) R_{fc}^2 \leq 430 \text{ MPa}$$

Here the scaling constant  $C \approx 1.4$  and the volume fraction of the structural material is  $f_{\text{structure}} = 0.564$ . The magnetic field for the central solenoid is 13.5 T. The flux core radius  $R_v = 0.66$  m and the thickness of the the CS coil  $\Delta_{OH} = 0.70$  m. Evaluation of the above equation yields  $\sim 230$  MPa, which is well below the tensile limit of 430 MPa<sup>5</sup>, confirming that the thickness of the CS coil is adequate to support the electromagnetic force.

The startup Volt-seconds requirement may be written<sup>48</sup>

$$\pi \cdot \Delta B_{OH} \cdot R_v^2 \left[ 1 + \frac{\Delta_{OH}}{R_v} + \frac{1}{3} \cdot \left( \frac{\Delta_{OH}}{R_v} \right)^2 \right] \geq VS_{\text{req-start}}$$

where  $\Delta B_{OH} \approx 2B_{OH}^{\text{max}} = 26.3$  T. Evaluation of this expression yields 87.7 V-s, satisfying the startup requirement of  $VS \geq VS_{\text{startup-required}} = 82.5$  V-s and confirming  $R_v = 0.66$  m.

The second part of the magnet analysis involved the Toroidal Field Coils, for which the preliminary estimate of 0.43 m for the radial width was confirmed by scaling down the ITER TF coil dimensions by conserving the ITER tensile stress  $\approx$  magnetic force/structural cross sectional area. This magnetic force is roughly equal to a constant times the square of the current in each TF leg, so that the stress is  $\sigma = F/A = (C I^2)/A$ . Here A equals the cross section area of the structural material in each TF coil. In GCFTR-2 the required current in each coil is 6.4 MA. In ITER<sup>6</sup>  $I = 9.13$  MA and  $A = 0.3$  m<sup>2</sup>. This scaling then leads to the area for GCFTR-2  $A = 0.15$  m<sup>2</sup>, which works out to a radial thickness  $\Delta_{TF} = 0.43$  m. It was then confirmed that the required number of conducting strands can fit in this geometry. Note that this scaling procedure doesn't take into account local stresses due to support structures, etc., analysis of which would require methods beyond the scope of this study.

In summary, the superconducting magnet system design of GCFTR<sup>5</sup> was adopted for GCFTR-2, with the single exception of reducing the radial thickness of the TFC to 0.43 m. The flux core radius of 0.66 m, the CS radial thickness of 0.70 m, the cable-in-conduit conductor design, the total current and the maximum field capability remain unchanged.

## VI.C. Tritium Production

The objective of using current reactor technologies or near-term technologies with respect to tritium self-sufficiency was achieved by placing He-cooled Li<sub>2</sub>O Tritium Breeding Elements (TBE) in both the outboard and inboard blanket-shield, as well as replacing 0.2% (by volume) of the fuel pins in the reactor core with Li<sub>2</sub>O pins.

The TBE design consists of a wall made of structural materials with ceramic breeder pebbles inside. Several designs have been proposed for such breeding blanket concepts<sup>49</sup>, which were modified to fit within the blanket and shield regions of the GCFTR-2. The TBE will be cooled by high-pressure helium flowing through tubes in the core. The tritium will be swept out of the blanket into a separate helium purge gas flow and removed online into a tritium processing system. In order to meet tritium self-sufficiency requirements, Li<sub>2</sub>O pins also must be placed inside the transmutation reactor core with their own He purge gas system.

The tritium breeding material will be Lithium Oxide (Li<sub>2</sub>O) enriched in <sup>6</sup>Li. Li<sub>2</sub>O was selected due to its higher atomic density of lithium as opposed to other potential ceramics (Li<sub>2</sub>O, Li<sub>2</sub>TiO<sub>3</sub>, Li<sub>2</sub>ZrO<sub>3</sub>, etc.). Drawbacks of this choice are that Li<sub>2</sub>O is hygroscopic and exhibits poor chemical stability. Additionally the temperature window for operation is smaller than that of the alternatives. The Li<sub>2</sub>O

operating temperature range is approximately 400°C to 800°C<sup>49</sup>. Below this temperature the pebbles are unable to release the tritium because the diffusivity of the tritium to the surface of the micro-particles becomes too small. Above this temperature range, the swelling of the particles increases and closes off the porosity, thus preventing the migration of the tritium into the purge gas stream. Optimal operating temperature would be closer to the lower limit of the range<sup>49</sup>. Li<sub>2</sub>O has a melting point of 1570°C.

The tritium production design will consist of 90% enriched natural lithium in the outboard blanket-shield in order to take advantage of the large <sup>6</sup>Li cross section in the thermal neutron energy range. The inboard reflector region will only be enriched to 30% <sup>6</sup>Li because tritium production from the <sup>7</sup>Li reaction is more prevalent in the higher energy neutron flux emerging inward from the fusion plasma source. The Li<sub>2</sub>O micro-particles are considered to be at 90% theoretical density (TD of Li<sub>2</sub>O is 2.013 g/cm<sup>3</sup>). A beryllium neutron multiplier will be employed in the TBE. The dimensions and materials of the TBE are described in Section IV.

The net production of tritium must exceed the net losses of tritium through burn up in the plasma by a margin adequate enough to compensate for losses and the radioactive decay during extraction and storage between production and use. Some loss of tritium can also be attributed to the fractional buildup between 0.01 and 0.5 which is inversely proportional to the flow rate into the plasma<sup>50</sup>. The models used to calculate tritium self-sufficiency depend on rather uncertain estimations of losses and error. Studies show an uncertainty of roughly 5% to 7% is to be expected<sup>51</sup>.

To be certain that self-sufficiency is attained a number greater than the theoretical requirement is necessary. Using the analysis of Ref. 50, it is estimated that a minimum tritium breeding ratio of greater than 1.06 is required to achieve tritium self-sufficiency of the GCFTR-2. Allowing for reasonable uncertainties (5%) and using the parameters in Table 18, the estimation is required TBR ≈ 1.12.

The required ( $\Lambda_r$ ) and achievable ( $\Lambda_a$ ) ratios were calculated from<sup>8</sup>:

$$\Lambda_r = 1 + G_0 + \Delta_G$$

$$\Lambda_a = \Lambda_c - \sqrt{\Delta_S^2 + \Delta_P^2}$$

Where

$G_0$  = tritium breeding margin to compensate for holdup, losses, decay, and reserves

$\Delta_G$  = uncertainties in breeding margin in reference parameters

$\Lambda_c$  = calculated TBR

$\Delta_S^2$  = uncertainties in system definition

$\Delta_P^2$  = uncertainties in predicting TBR due to uncertainties in nuclear data, calculation methods, and geometrical representation

**Table 18: Parameters for tritium losses<sup>49</sup>**

Parameter	Value	Definition
$\varepsilon_2$	0.001	Breeder processing loss
$\varepsilon_3$	0.001	Blanket coolant processing loss
$\varepsilon_4$	0	Fuel cleanup and isotope separation units loss
$\varepsilon_6$	0.001	Plasma exhaust processing loss
$\varepsilon_7$	0.001	Limiter coolant processing loss
$\varepsilon_8$	0.001	First-wall coolant processing loss
$\beta$	0.05	Tritium fractional burn up in plasma
$f_c$	0.01	Breeder to blanket leakage
$f_L$	0.0001	Plasma to limiter leakage
$f_F$	0.0001	Plasma to first-wall leakage

It is estimated that a beginning of cycle inventory of 144 g will be required<sup>48</sup>. The inventory will need to be sufficient to cover tritium consumption at a higher fusion power than the nominal upper limit of 180 MW, if that should prove to be necessary. The maximum tritium inventory is estimated to be approximately 1.2 kg<sup>48</sup>.

## VI.D Divertor and First-Wall

The divertor and first-wall design for the fusion neutron source were adapted for He cooling from the ITER design<sup>6</sup>, which uses water flowing through channels located in the structure for cooling. A detailed drawing of the ITER divertor was scaled down, Fig. 13, to serve as the model for the heat removal calculations described in section VII. The model was scaled down such that the width of the divertor would reach approximately half way out in the plasma region. The divertor targets are lined with tungsten tiles backed with a layer of copper that bonds the tiles to CuCrZr alloy matrix. Cooling fins must be added behind the targets to achieve adequate heat removal with He cooling. The first-wall consists of a 2 cm thick plate of ferritic steel (e. g. HT-9) coated on the plasma facing side with 0.5 cm of Be and cooled by He.

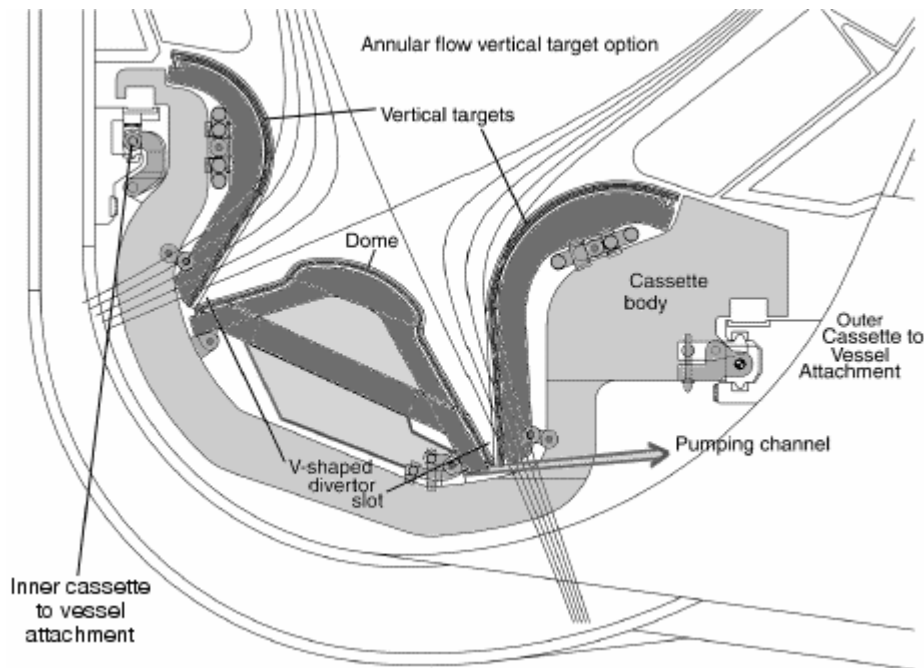


Fig. 13 Detailed drawing of the ITER divertor<sup>6</sup>

## VII. THERMAL DESIGN

### VII.A. Core Thermal Design

In order to support the selection between the pin and block fuel element options discussed in Section III, thermal analyses were performed for each type under steady-state conditions.

#### VII.A.1 Steady-State Analysis: Fuel Pins

The reactor fuel design was based upon a standard PWR pin; that is, fuel material surrounded by an inert gas “gap” blanket and a cladding structure. Two pin types were considered – one composed of BISO fuel pellets suspended within a zirconium carbide matrix, the other composed of TRISO fuel pellets suspended within a silicon carbide matrix. The dimensions of the fuel pin are provided in Table 19 and Figure 5.

Table 19: Fuel Pin Dimensions

Fuel Outer Radius (cm)	Clad Inner Radius (cm)	Clad Outer Radius (cm)
0.60	0.61	0.67

At 3000 MWth uniformly distributed power in the reactor, the average volumetric fission heat source is  $q''' = 42.2 \text{ MW/m}^3$ , which was used in the thermal analysis. With a He mass flow rate of 2870 kg/s, the He coolant entered at 280 °C and exited at 494 °C, and the core He pumping power was 0.15 MW.

The temperature distribution in a fuel pin was evaluated at three different axial locations in an average coolant channel in the core: the inlet, the outlet, and the arithmetic mean “bulk” temperature. In order to apply a thermal resistance model, the fuel pin must be treated as a homogeneous mixture of the fuel kernels, matrix, gas gap, and zircaloy cladding. The thermal conductivities for the various pin components are listed in Table 20.

**Table 20: Fuel Pin Component Heat Conductivities<sup>5</sup>**

Pin Component	Thermal Conductivity (W/m-°C)
Silicon Carbide Matrix <sup>52</sup>	120
Zirconium Carbide Matrix	18.94
BISO Fuel	15.18
TRISO Fuel	6.49
Helium Gap	0.26
Zircaloy Cladding	18.94
Helium Heat Transfer Coefficient	4161.81 W/m <sup>2</sup> -°C

The heat transfer coefficient (h) for the helium coolant was dependent upon the coolant channel geometry and helium flow conditions and was calculated<sup>53</sup> to be 4161.81 W/m<sup>2</sup>-°C.

The homogenized thermal conductivities for the two pin loadings were based upon the volume fraction for each pin type. The homogenized conductivities for the BISO/ZrC and TRISO/SiC pins were 16.87 W/m-°C and 51.76 W/m-°C, respectively. Application of the thermal resistance model resulted in the distribution plotted for the TRISO/SiC pins in Figure 14. Similar temperature distributions were found for the BISO/ZrC pins. Heat removal from both fuel types thus is readily accomplished under nominal steady-state operating conditions, since the lowest melting temperature among the pin components is that of the zircaloy cladding at 1845°C.

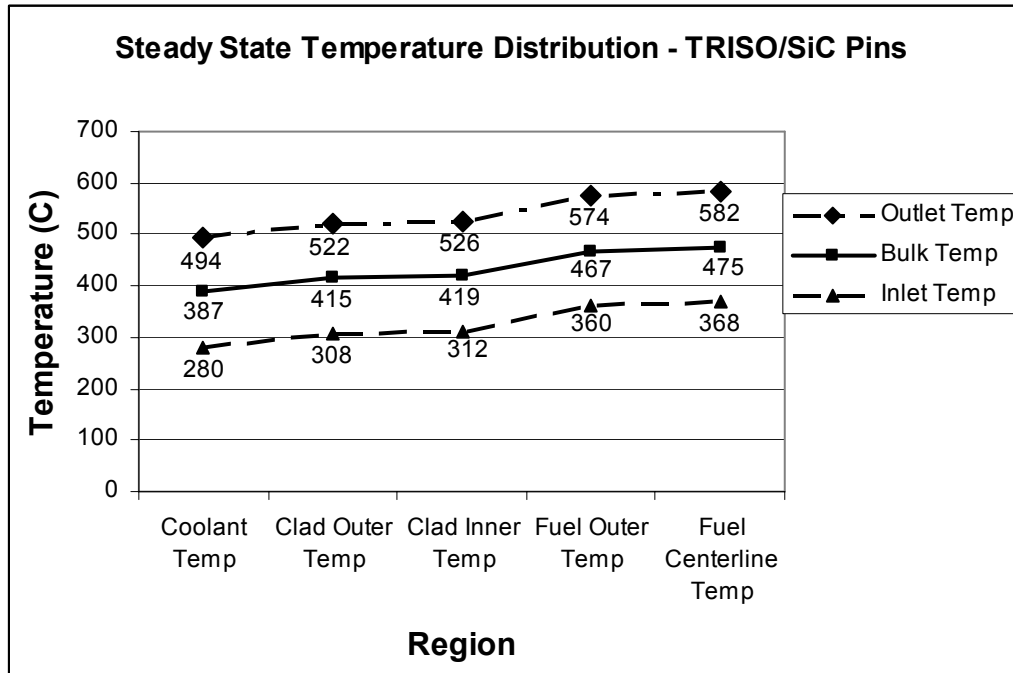


**Figure 14: TRISO/SiC Pin Temperature Distributions (Inlet, outlet and midway)**

### VII.A.2 Fluent Calculation: Fuel Pins

The steady state condition of the fuel pins under normal load also was investigated by modeling one pin centered in a hexagonal box of helium coolant that represents a unit cell for one pin. The following programs were used: a 3-D CAD program called Solid Edge<sup>54</sup> was used to build a fuel pin that had a radius of 0.67 cm and a height of 3 m and the equivalent cell; GAMBIT<sup>55</sup> was used to mesh nodes in the rod and cell, and a computational fluid dynamics program called Fluent<sup>55</sup> was used to model the steady state temperature distribution in the pin and the coolant, using the parameters in Table 21. This resulted in a somewhat smaller peak centerline temperature of 535°C at the top of the core but the same outlet coolant temperature of 494°C. The average coolant velocity was about 85 m/s.

**Table 21: Fluent Model Parameters**

He mass flow rate	0.01435 kg/s-cell
Volumetric heat generation of rod	42.17 MW/m <sup>3</sup>
He inlet temperature	280°C
Turbulence model	<i>k</i> - $\epsilon$ RNG method
Inlet turbulence	5%
Inlet pressure	7 MPa
$k_{\text{homogenized rod}}$	51.759 W/m-K
$k_{\text{helium}}$	0.26 W/m-K
He viscosity	3.37e-5 kg/m-s

### VII.A.3 Steady-State Analysis: Low Density Graphite Foam

A thermal analysis, using the thermal resistance model<sup>56</sup>, of the low-density graphite foam in a hexagonal fuel matrix (see Fig. 6) was performed. The only calculation that was performed for LDGF steady-state analysis was the bulk temperature at the midplane of the core. When calculating the bulk LDGF temperature, the following assumptions were made: same coolant pumping power, mass flow rate, power density, and v/o of coolant were used as in the above pin calculation. The thermal properties of the LDGF and the fuel configuration were different, of course. The maximum bulk midplane temperature in the LDGF fuel block was determined to be 484°C (TRISO) and 483°C (BISO) at the edges of a typical block within the core, which is slightly more than the midplane centerline fuel pin temperature of 475°C. Thus, there is essentially no difference in the nominal steady-state heat removal properties of the fuel pin and fuel block configurations.

### VII.B Loss of Coolant Accident (LOCA)

A complete loss of the flow of coolant was considered. Predicting the consequences of such an accident is necessary in order to know whether or not passive safety is possible. When such an accident occurs, it is assumed that the neutron source is immediately shut down and there is no more heat produced by fission. However, there is still heat generated as decay heat from (primarily) fission products. This decay heat calculated using the ORIGEN-S<sup>31</sup> code is shown in Fig. 16 for fuel irradiation periods of 5 years, 0.5 years, and 0.1 years in GCFTR-2. The decay heat from typical PWR fuel is shown for comparison.

When the flow of coolant is completely stopped in a LOCA, the only significant form of heat transfer that would remove the decay heat from the fuel pins is radiation. There also would be a slight amount of conduction through structural material, but that form of heat transfer was ignored because of its insignificance. A MATLAB code was written in order to calculate the temperature change in the pins during a LOCA.

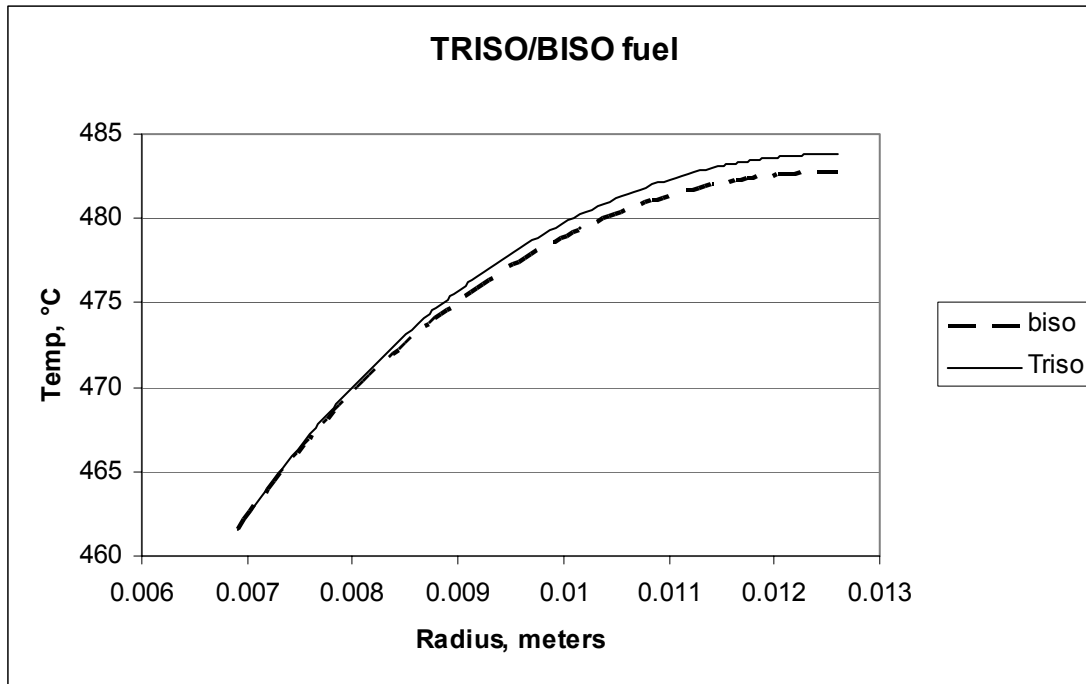


**Figure15: Steady State Temperature Distribution of an average hexagonal graphite assembly**

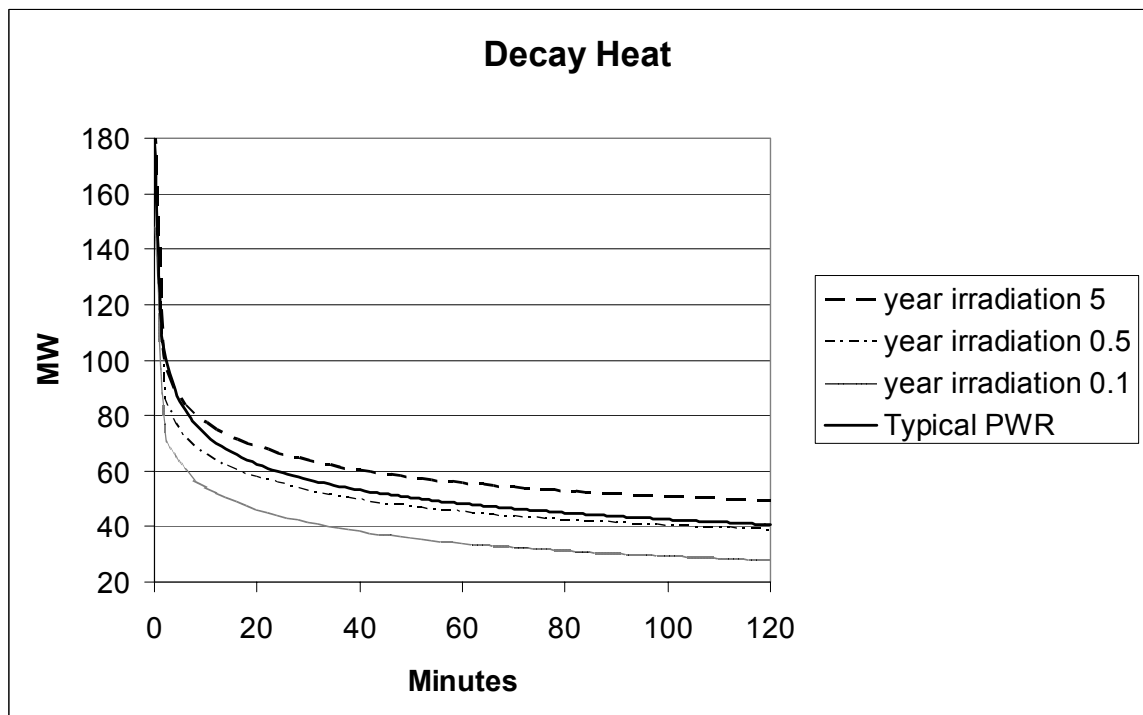


**Figure 16: Decay Heat**

In order to calculate the heat lost from radiation, view factors for the fuel pin configuration needed to be obtained. For a horizontal cross section of the core, each interior fuel pin is surrounded by six pins and there are six channels between adjacent pins where heat can escape (see Fig. 5). Using the reference pin pitch and diameter given above, the view factor for each adjacent pin is approximately 0.157. This means that approximately 15.7% of the heat that can be emitted by radiation from one pin is incident directly on each of the six adjacent pins. Similarly, a view factor of about 1% was obtained from a pin to the channel between two adjacent pins. Exterior pins in the assembly had a view factor to the assembly wall of 34.4%. Thus, the exterior pins would radiatively cool first by radiating to the assembly wall, the second row of pins would cool by radiating to the exterior pins, etc. Heat is also radiated out

vertically from the tops and bottoms of the fuel pins, and the vertical view factor for these surfaces to the walls of the core was assumed to be 100%.

At the beginning of the LOCA, it was assumed that the temperature of each pin was 408°C. It was assumed that the pins and the reactor walls were black bodies and no heat was reflected from the surface. The MATLAB code calculated the amount of heat generated in each radial row of fuel pins for each minute and then calculated the temperature change due to that heat addition. These temperature differences were important in calculating the amount of heat that would radiate away from the pins because in order for a net amount of heat to be radiated away from a pin, the surrounding surfaces must be at a lower temperature than the pin itself. The heat was then added to adjacent rows of pins or the reactor walls and then new temperatures were calculated. This calculation was carried out for the first 48 hours after a LOCA occurs.

It was determined by this calculation that under radiation heat removal only, the zircaloy cladding on the fuel pins would melt (1845°C) at approximately 25 minutes after the LOCA starts, and the TRU fuel kernel would melt (2035°C) a few minutes later, as shown in Fig. 17. Thus, the reactor is not passively safe and must be designed with an active safety system in order to prevent melting of the clad and TRU kernel in a LOCA. However, after approximately 50 minutes the decay heat that would be generated would be able to be removed by radiation without the melting temperature of any part of the fuel being exceeded. Therefore, an active safety system would only need to supply emergency coolant within the initial hour of a LOCA.

The calculations were repeated with emergency helium injection for varying durations during a LOCA, using the decay heat source that would be present after five years of fuel burnup. The emergency cooling system was assumed to operate in a fashion similar to that of the primary cooling system; that is, the heat transfer coefficient  $h$  was assumed to be the same. In addition, the fuel pin temperature was assumed to remain at steady-state levels for the duration of emergency cooling, although, under actual conditions, the pin temperature would actually decrease. This assumption was made so as to add a degree of conservatism to the calculation.

Figure 17 shows the fuel pin temperature as a function of time under a LOCA scenario as related to several melting temperatures, the lowest one being that the cladding at 1845°C. If there is no emergency coolant injection then the zircaloy cladding (1845°C mp) and the TRU kernel (2035°C mp) would both melt, but the ZrC (3250°C mp) and SiC (3375°C mp) would not. For the entire core to survive a LOCA without any fuel melting, a minimum of 10-15 minutes of emergency helium cooling would be required.

If the pins were designed without the zircaloy cladding, then the only material to melt during the LOCA would be the TRU kernel. Since the kernel is encased in ZrC and pyrolytic graphite coatings, which would not melt, it might be argued that the design would be passively safe if the zircaloy cladding could be omitted.

### VII.C Divertor Heat Removal

Although the divertor design was adapted from the ITER H<sub>2</sub>O cooled design (Fig. 13), heat removal from the GCFTR-2 He cooled divertor differs significantly due to the choice of coolant. Some form of fins will be needed in the void space behind the vertical targets in order to adequately remove the heat from the structure. The calculations to determine the amount of divertor heat removal were made with Fluent<sup>55</sup> by using a highly simplified 3-D model made in Solid Edge<sup>54</sup> and meshed in GAMBIT<sup>55</sup>. The Fluent model uses a large void space behind the tiles with no cooling fins and a divertor depth of 1 m. From this a steady state temperature distribution for the modified ITER design, which is now helium cooled instead of water-cooled, (no cooling fins) was found for two surface heat fluxes, 1 MW/m<sup>2</sup> and 2 MW/m<sup>2</sup>. This information determines the additional heat removal requirement for a set of fins that would be able to remove enough heat to obtain an acceptable temperature distribution.

The entire structure is modeled as CuCrZr that has a density of 8900 kg/m<sup>3</sup>, specific heat of 376 J/kg-K and thermal conductivity 320 W/m-K. The required helium mass flow rates for the 1 MW/m<sup>2</sup> and 2 MW/m<sup>2</sup> cases are 77.1 kg/s and 231.2 kg/s, respectively, and the inlet pressure is 7 MPa. The pumping power for the Helium through the divertor was calculated to be 143.6 MW<sup>5</sup>. The turbulence is modeled the same way as described above for the equivalent unit cell for the fuel pins, except that a 10% turbulence intensity was set for the inlet. The temperature of the plasma facing components has a surface

profile that starts out cool and gradually becomes hotter at the outlet. The maximum temperature seen is 1217°C for the 1 MW/m<sup>2</sup> case and 1417°C for the 2 MW/m<sup>2</sup> case.

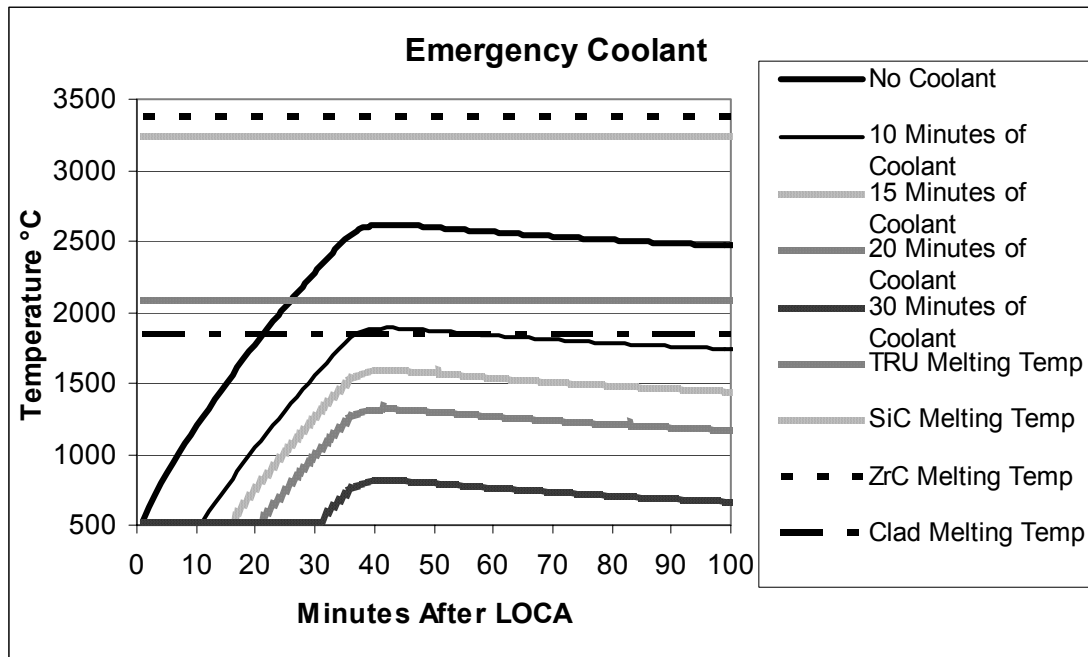


**Figure17: Fuel Temperature during LOCA with and without Emergency Core Cooling**

Knowing the mass and the maximum temperature of the plasma facing component, a calculation was performed using the specific heat of the material to determine how much energy needs to be removed to lower the temperature to a safe level. For the sake of the study 1000°C was defined as a safe temperature. For the 1/2 MW/m<sup>2</sup> case 74/142 MJ need to be removed from the steady state condition to lower the temperature to 1000°C. An appropriate fin design that would remove energy at this rate would allow safe operation of the GCFTR-2 divertor.

#### **VII.D Secondary System & Electrical Performance**

A secondary electrical system is needed to convert the heat to useful electrical work. Since Helium is the coolant for the reactor, a typical Brayton cycle<sup>57</sup> will be used which utilizes the He directly. In order to realistically utilize the 3000MWth that is being produced in the core, a total of four Brayton cycles will be used, one for each 90 degree segment of the reactor. Therefore, each Brayton cycle corresponds to 750MWth. Figure 18 shows one of the Brayton cycles and Table 21 identifies the properties at each section of the thermodynamic cycle.

The total electric power that is extracted from the 750MW cycle is 255MWe corresponding to a thermal efficiency of 34%. The total electrical power for the entire reactor is 1020MWe. However, in order to calculate the net amount of electrical power, the operating power requirements must be taken into consideration. These losses include power for all of the magnets involved in confinement (approx. 30MW), the heating and current-drive systems for the plasma (90MW<sup>5</sup>), and the coolant pumping power for both the core and the divertor (approx.200MW). After taking into account all of the power used to operate the reactor, the net electrical power for the entire system is 700MWe. The electrical power amplification factor ( $Q_e$ ) is calculated as the total electrical power divided by the net operating power requirements and this equals 3.19.



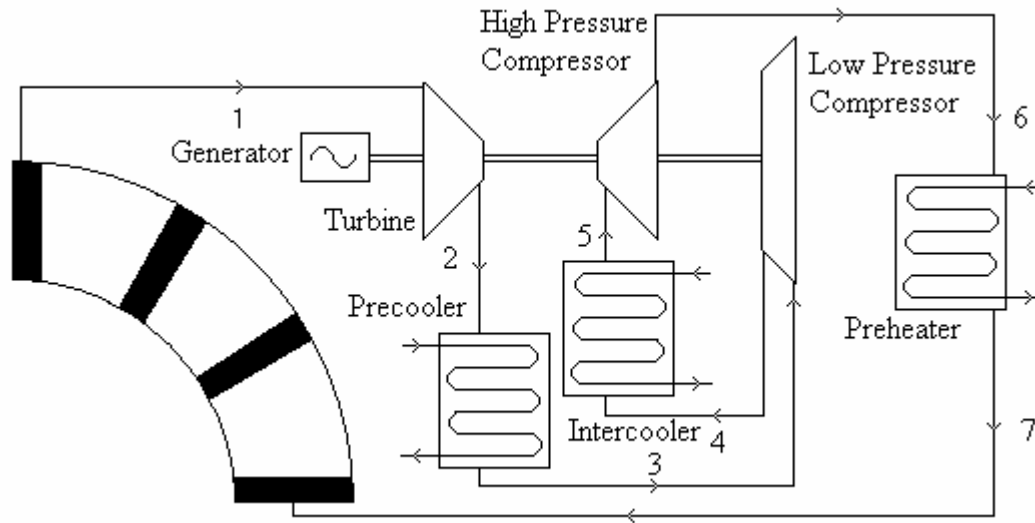


**Figure 18: Secondary Electrical System Diagram (Brayton Cycle)**

**Table 21: Thermodynamic Properties of Brayton Cycle**

Section	Temperature (°C)	Pressure (MPa)
1	494	7.00
2	122	2.41
3	25	2.41
4	66	3.09
5	25	3.09
6	151	7.00
7	300	7.00

## VIII. SUMMARY

A design concept for a sub-critical, gas cooled fast transmutation reactor (GCFTR) driven by a tokamak DT fusion neutron source has been analyzed and further evolved. The GCFTR-2 objectives are 1) to obtain deep burn ( $> 90\%$ ) of transuranics (TRU) extracted from spent nuclear fuel by utilizing coated fuel particle (TRISO or BISO) technology, and 2) to base the design on near-term physics and technologies that are being developed in the U. S. DoE Nuclear and Fusion programs and corresponding international programs.

We considered coated TRU fuel embedded in SiC or zircaloy to form fuel pins or embedded in low density graphite foam to form solid fuel blocks, all He-cooled, as fuel options. All options had similar heat removal characteristics under nominal steady-state conditions and under loss-of-coolant accident (LOCA) conditions. The TRISO/SiC fuel pin option resulted in the largest ratio of transmutation rate to neutron damage rate and the most negative or least positive coefficients of reactivity. The graphite foam fuel block option was rejected because of excessive brittleness and a high-temperature step in the formation process that exceeded the melting temperature of the TRU kernel in the coated fuel particle. The TRISO/SiC fuel pin option was chosen over the BISO/zircaloy fuel pin option because of superior neutronics properties for transmutation.

The annular fast transmutation reactor core ( $R_{in} = 485$  cm,  $W = 112$  cm,  $H = 300$  cm) will be 59.8 v/o fuel, 0.2 v/o  $Li_2O$ , 30 v/o He and 10 v/o structure, the fuel will be 62.8 v/o coated TRU particles and 37.2 v/o SiC. The core would operate at  $k_{eff} \leq 0.95$ ,  $P_{th} = 3000$  MWth at a nominal power density of 42 MW/m<sup>3</sup> and a tritium breeding ratio  $\geq 1.1$  to achieve tritium self-sufficiency. The He mass flow rate of 2870 kg/s at  $T_{in} = 280$  C and  $T_{out} = 494$  C would limit the maximum fuel temperature to 582 C under normal operation. For the entire core to survive a LOCA without any zircaloy clad melting, a minimum of 10-15 minutes of emergency helium cooling would be required during the first hour.

The sub-critical reactor would be driven by a superconducting tokamak DT fusion neutron source that would produce up to 180 MW of power and a neutron source rate of  $6.5 \times 10^{19}$  /s. The major parameters of the tokamak plasma are ( $R_{\text{major}} = 3.73$  m,  $\beta_N \leq 2.0$ ,  $Q_p \approx 3$ ,  $H_{98} = 1$ ). The plasma physics and fusion technology design basis for the neutron source is the same as for ITER, except for modest extensions in current drive efficiency, and ITER operation would serve as a prototype.

At a thermal power of 3000MW/FPY, the GCFTR-2 transmutes approximately 1.11MT of TRUs, which is equivalent to the TRU production rate of three 1000MWe LWRs per FPY. The GCFTR-2 produces 700 MW net electrical power and operates with an electrical multiplication factor  $Q_e = 3.2$ .

## REFERENCES

1. "GEN-IV International Forum: Nuclear Energy Systems for the Future", Web site <http://www.gif.inel.gov/>.
2. "Advanced Fuel Cycle Initiative", Web site <http://www.nuclear.gov/afci>.
3. F. H. Southworth, et al., "The Next Generation Nuclear Plant (NGNP) Project", Proc. Global 2003 Conf., New Orleans, LA, November 16-20, 2003, American Nuclear Society CD-ROM (2003).
4. C. Rodriguez, et al., "Deep-Burn: making nuclear waste transmutation practical", Nucl. Eng. Des., 2805 (2003).
5. W. M. Stacey, et al., "A Subcritical, Gas-Cooled Fast Transmutation Reactor with a Fusion Neutron Source", Nucl. Technol., 150, 162 (2005).
6. Web site <http://www.iter.org>; also "ITER Detailed Design Report, Cost Review and Safety Analysis, International Thermonuclear Reactor Project Report (1996); also "The ITER Project L-7 Implementation", ENEA, Web site [www.brasimone.enea.it/iterl-7](http://www.brasimone.enea.it/iterl-7) (1998).
7. E. Long, et al., "Fabrication of ORNL Fuel Irradiated in the Peachbottom Reactor and Post-irradiation Examination of the Recycle Test Elements 7 and 4", Oak Ridge National Laboratory report (Oct. 1974).
8. D. A. Petti, et al., "Key Differences in the Fabrication, Irradiation and High Temperature Accident Testing of U. S. and German TRISO-Coated Particle Fuel, and Their Implications on Fuel Performance", Nucl. Eng. Des., **222**, 281 (2003).
9. B. B. Kadomtsev, et al., "USSR Contribution to the Phase IIA INTOR Workshop", Vol 2, p. VIII-64 (1982).
10. M. Sawan, Univ. Wisconsin, personal communication (2004).
11. M. Kubota, Y. Morita, I. Yamaguchi, I. Yamagishi, T. Fujiwara, M. Watanabe, "Development of the Four Group Partitioning Process at JAERI," Fifth OECD/NEA Information Exchange Meeting on Actinide and Fission Product Partitioning and Transmutation, Session 2, pp. 1-9 (1998).
12. M. C. Thompson, M. A. Norato, G. F. Kessinger, R. A. Pierce, T. S. Rudisill, and J. D. Johnson "Demonstration of the UREX Solvent Extraction Process with Dresden Reactor Fuel Solution," Westinghouse Savannah River Company report (2002).
13. IAEA "Implications of Partitioning and Transmutation in Radioactive Waste Management" IAEA Report, Vienna (2003).
14. C. Madic, "Overview of the Hydrometallurgical and Pyro-metallurgical Processes Studied Worldwide for the Partitioning of High Active Nuclear Wastes." OECD/NEA 6<sup>th</sup> Information Exchange Meeting, Madrid, Spain, pp. 53-64 (2000).
15. E. Zimmer and C. Ganguly, "Reprocessing and Refabrication of Thorium-Based Fuels". [http://www.iaea.org/inis/aws/fnss/fulltext/0412\\_8.pdf](http://www.iaea.org/inis/aws/fnss/fulltext/0412_8.pdf) Institut für chemische Technologie der nuklearen Entsorgung, Kernforschungsanlage Jülich GmbH (2005).
16. J. J. Laidler, L. Burris, E. D. Collins, J. Duguid, R. N. Henry, J. Hill, E. J. Karell, S. M. McDevitt, M. Thompson, M. A. Williamson, J. L. Willit, "Chemical Partitioning Technologies for an ATW System." Progress in Nuclear Energy, Vol 38, No 1-2 pp. 65-79 (2001).
17. D. E. Clark, J. B. White and A. J. Machiels, "Nuclear Waste Management", Advances in ceramics, vol. 20, American Ceramic Soc., Waterville, OH (1986).
18. Reactor Institute Delft web site <http://www.iri.tudelft.nl/~rfwww/images/triso.jpg>

19. F. J. Homan, T. B. Lindemer, E. L. Long, Jr., T. N. Tiegs and R. L. Beatty, "Stoichiometric Effects on Performance of High-Temperature Gas-Cooled Reactor Fuels from the U-C-O System," Nuc. Technol., 35, 428-441 (1977).
20. T. B. Lindemer, "Thermochemical Analysis of Gas-Cooled Reactor Fuels Containing Am and Pu Oxides," ORNL/TM-2002/133, Oak Ridge National Laboratory (2002).
21. Hideyuki Hayashi, Kazuhiro Sawa, Yoshihiro Komori "Irradiation experiences and the future plan in the HTTR project." Proceedings of the International Symposium on Research Reactor and Neutron Science, Daejeon, Korea, April (2005).
22. W. Corwin and J. Klett, "High Conductivity Graphite Foams and Applications," Oak Ridge National Laboratory report (May 2004).
23. R. A. Karam, et al., "High Temperature Gas-Cooled Fast Reactor", Proc. Int. Conf. Adv. Power Plants, Seoul, May 14-20, 2005.
24. W. J. Lackey, Thomas L. Starr, "Fabrication of Fiber Reinforced Ceramic Composites by Chemical Vapor Infiltration: Processing, Structure and Properties." Fiber Reinforced Ceramic Composites. Ed. K. S. Mazdiasni. Park Ridge: Noyes Publications, 1990.
25. J. Klett, Oak Ridge National Laboratory, Private Communication (2005).
26. J. F. Shackelford and W. Alexander, ed. *CRC Materials Science and Engineering Handbook*, CRC Press, Boca Raton (2000).
27. T. Besmann, "Chemical Vapor Infiltration Modeling and Processing of Energy-Related Materials", ORNL report (Nov, 1999).
28. K. Minato and T. Ogawa, "Research and Development of ZrC Coated Particle Fuel", Proc. GLOBAL 2003 Atoms for Prosperity", American Nuclear Soc., (CD-ROM) p. 1068 (2003).
29. C. T. Walker, T. Kameyama, S. Kitaima and M. Kinoshita, "Concerning the Microstructure Changes that Occur at the Surface of UO<sub>2</sub> Pellets on Irradiation to High Burnup", Journal of nuclear materials, 188, 73-79 (1992).
30. H. Bailey, D. Menessier and C. Prunier, *The Nuclear Fuel of Pressurized Water Reactors and Fast Reactors: Design and Behaviour*, Intercept Ltd, Hampshire, UK, Ch. 5, p 427 (1999).
31. "ORIGEN-S: SCALE System Module to Calculate Fuel Depletion, Actinide Transmutation, Fission Product Buildup and Decay, and Associated Radiation Source Terms," NUREG/CR-200, Rev. 7 (ORNL/NUREG/CSD-2/V2/R7) Oak Ridge National Laboratory (2004).
32. T. Saling, *Radioactive Waste Management*, Hemisphere Publ. Corp., New York (1990).
33. R. Rasmussen, "Dry Storage Option for Spent Fuel Management", Proc. USCEA Fuel Cycle Conf., New Orleans (1988).
34. Robert Cochran and Nicholas Tsoulfanidis, *The Nuclear Fuel Cycle : Analysis and Management*, American Nuclear Soc., LaGrange Park, IL (1990).
35. Web site [www.wisconsinmetaltch.com](http://www.wisconsinmetaltch.com)
36. K. Minato and T. Ogawa, "Research and Development of ZrC-Coated Particle Fuel", Proc. GLOBAL 2003 Atoms for Prosperity: Updating Eisenhower's Global Vision for Nuclear Energy (CD-ROM) p. 1068-1074 (2003).
37. C. de Oliveira and A. Goddard, "EVENT-A Multidimensional Finite Element-Spherical Harmonics Radiation Transport Code," Proc. Int. Seminar 3-D Deterministic Radiation Transport Codes, Paris, France, Organization for Economic Cooperation and Development (1996)
38. H. Henryson et al., "MC<sup>2</sup>-2: A Code to Calculate Fast neutron Spectra and Multigroup Cross Sections," ANL-8144, Argonne National Laboratory (1976)
39. "DANTSYS: A Diffusion Accelerated Neutral particle Transport Code System," LA-12969-M Manual UC-705, Los Alamos National Laboratory (1997)
40. J. F. Briesmeister, Ed. "MCNP – A General Monte Carlo N-Particle Transport Code, Version 4B," Los Alamos National Laboratory, LA-12625-M (1997).
41. I.C. Gauld, O.W. Hermann, and R.M. Westfall, NUREG/CR-0200, Seventh Edition, (2004)
42. "Understanding NJOY", Los Alamos National Laboratory, LA-UR-00-1538. <http://t2.lanl.gov/njoy/>. (2000).
43. B. J. Toppel, "A User's Guide to the REBUS-3 Fuel Cycle Analysis Capability," ANL- 83-2, Argonne National Lab (1983).
44. "KENO V.a: An Improved Monte Carlo Criticality Program," NUREG/CR-0200, Rev. 7, Vol. II, Section F11, ORNL/NUREG/CSD-2/R7 (2004).

45. J. D. Galambos, et al., "Commercial Tokamak Reactor Potential with Advanced Tokamak Operation", Nucl. Fusion, 35, 551 (1995).
46. M. Huguet, "Key Engineering Features of the ITER-FEAT Magnet System and Implications for the R&D Programme" Nucl. Fusion, 41, 645 (2001).
47. ITER Technical Basis, Chap. 2.1 Magnets, G A0 FDR 1 01-07-13 R1.0 (2001)
48. W. M. Stacey, et al, "A Fusion Transmutation of Waste Reactor", Fusion Science and Technology, 41, 116-140 (2002).
49. M. A. Abdou, M. Tillack, and R. A. Raffray, "Thermal, Fluid Flow and Tritium Release Problems in Fusion Blankets", Fusion Technology, 18, 165 (1990).
50. M. A. Abdou, et al., "Deuterium-Tritium Fuel Self-Sufficiency in Fusion Reactors", Fusion Technology, 9, 250 (1986).
51. M. A. Abdou, et al., "Evaluation of the Prediction Uncertainty in Tritium Production based on Results from Experiments on an Li<sub>2</sub>O Annular Blanket surrounding a 14 MeV Simulated Line Source", Fusion Eng. Des., 28, 673 (1995).
52. "Materials / Silicon Carbide (SiC) Properties". 2002. Accuratus. L March 2005 <<http://www accuratus.com/silcar.html>>
53. Mujid S. Kazimi and Neil E. Todreas, *Nuclear Systems I: Thermal Hydraulics Fundamentals*, Hemisphere Publishing Corporation, New York pp 16-17, 417, 684-5 (1990).
54. Solid Edge, Version 15.0, "Computer Aided DrawingSolid", Solid Works Inc. (2003).
55. Fluent/Gambit, Version 6.1.22/s.1.2, "Computational Fluid Dynamics", Fluent Inc. (2004)
56. F. P. Incropera and D. P. DeWitt, *Fundamental of Heat and Mass Transfer*, Fifth Edition, John Wiley & Sons, Hoboken, NJ (2002) Chapter 3.
57. M. J. Moran and Howard N. Shapiro. *Fundamentals of Engineering Thermodynamics*, Fourth Edition. John Wiley & Sons, Inc, New York (2000) pp 441-467.